Alma Mater Studiorum – Università di Bologna

DOTTORATO DI RICERCA IN

CHIMICA

Ciclo XXVII

Settore Concorsuale di afferenza: 03/B2

Settore Scientifico disciplinare: CHIM-07

Patterning soft matter for cell culturing

Presentata da: Silvia Tortorella

Coordinatore Dottorato

Prof. Aldo Roda

Relatore

Prof. Francesco Zerbetto

Correlatore

Prof. Fabio Biscarini

Esame finale anno 2015

Alla mia famiglia

Ad Alessandro

ABSTRACT

In the search to understand the interaction between cells and their underlying substrates, life sciences are beginning to incorporate micro and nano-technology based tools to probe, measure and improve cellular behavior. In this frame, patterned surfaces provide a platform for highly defined cellular interactions and, in perspective, they offer unique advantages for artificial implants. For these reasons, functionalized materials have recently become a central topic in tissue engineering.

Nanotechnology, with its rich toolbox of techniques, can be the leading actor in the materials patterning field. Laser assisted methods, conventional and un-conventional lithography and other patterning techniques, allow the fabrication of functional supports with tunable properties, either physically, or topographically and chemically. Among them, soft lithography provides an effective (and low cost) strategy for manufacturing micro and nanostructures.

The main focus of this work is the use of different fabrication approaches aiming at a precise control of cell behavior, adhesion, proliferation and differentiation, through chemically and spatially designed surfaces.

3 types of patterning techniques were combined with 3 types of cell lines. Each method has been characterized at the nanoscale before cell seeding.

The thesis is divided as herein indicated: **Chapter 1** is an introduction on the state of the art of nanotechnology, patterning techniques and regenerative medicine, along with a brief reference of one of the guiding projects of my PhD (Implantable Organic Nano-Electronics I-ONE). In **Chapter 2** we collected all the functionalization, fabrication and characterization techniques learned and employed during the PhD period. **Chapter 3** and **Chapter 4** describe the main technique we have worked with for accurate and controlled molecule deposition on surfaces: Laser Assisted Bioprinting (LAB). A very exhaustive description is provided and also some very notable applications are shown. In **Chapter 5** the use of Lithographically Controlled Wetting (LCW) for patterning functional molecules (β-cyclodextrins, ACyD) on a glass support with modified hydrophobicity rate is reported in comparison with other drug-delivery methods. **Chapter 6** reports the use of thiols for the modulation of the cell adhesion onto surfaces. Using the electrochemical desorption of self-assembly monolayers (SAM) of thiols, is possible to fabricate a chemical gradient made of anti-fouling molecules that can affect cell adhesion and growth. **Chapter 7** concerns a very recent study about the fabrication of biodegradable-biocompatible microfluidics for the delivery of small volumes of active molecules preceded by a very short glance on the use of Polyhydroxybutyrate (PHB), a biodegradable polymer, employed for cell adhesion and growth.

Finally, at the end of the thesis, the main conclusions of the entire work are reported.

Table of Contents

Patterning adhesion proteins with Laser Assisted Bioprinting

Patterning chemical cues for cell positioning and migration

Chapter 1 – State of the art

In this chapter a brief introduction of the state of art of nanotechnology, surface functionalization and micro-nanopatterning is provided. A paragraph about regenerative medicine, with a particular focus on the thematic related to the regeneration of neural cells, is reported at the end of the chapter.

1.1 Nanotechnology

Nanotechnology is naturally very broad field, including different topics such as surface science, organic chemistry, molecular biology, semiconductor physics, microfabrication, etc. The related research and applications are equally different, ranging from the extension of conventional device physics to completely new approaches based on molecular self-assembly, from developing new materials with nanoscale dimensions to the direct control of matter on the atomic scale.
As defined by Saini et al [1], nanotechnology can be defined as the science and engineering involved in the design, synthesis, characterization, and application of materials and devices whose smallest functional organization, in at least one dimension, is on the nanometer scale. At these scales, is very important to considerate individual molecules and interacting groups in relation to the bulk macroscopic properties of the material or device, as it has a control over the fundamental molecular structure, which allows control over the macroscopic chemical and physical properties.
Scientists currently debate the future implications of nanotechnology. Nanotechnology may be able to create new materials and devices with a vast range of applications, such as in medicine, electronics, biomaterials and energy production. On the other hand, nanotechnology raises many of the issues already experienced by many novel technologies such as concerns about the toxicity and environmental impact of nanomaterials, and their potential effects on global economics, as well as speculation about various doomsday scenarios.
Concerning life sciences, these materials and devices can be designed to interact with cells and tissues at a molecular (i.e., subcellular) level, for applications in medicine and physiology, with a high degree of functional specificity, thus allowing a degree of integration between technology and biological systems not previously attainable. It should be appreciated that nanotechnology is not in itself a single emerging scientific discipline, but rather, the meeting of different traditional sciences, such as, chemistry, physics, materials science and biology, that bring together the required collective expertise needed to develop these novel technologies.

1.2 Micro-nanostructured functional surfaces

Basically, there are two approaches to fabricate micro and nanostructured materials: **top-down** and **bottom-up** (Figure 1.1). These terms were first applied to the field of nanotechnology by the Foresight Institute in 1989 in order to distinguish between molecular manufacturing (to mass-produce objects with conveyed order at the atomic scale) and conventional manufacturing (which can mass-produce large objects that are not atomically precise).

A **top-down** approach (also known as stepwise design and in some cases used as a synonym of *decomposition*) is essentially the breaking down of a system to gain insight into its compositional sub-systems, while bottom-up approaches seek to have smaller (usually molecular) components built up into more complex assemblies.

The top-down approach often uses the traditional workshop or microfabrication methods where externally controlled tools are used to cut, mill, and shape materials into the desired shape and order. Micropatterning techniques, such as photolithography and inkjet/laser assisted printing belong to this category.

Bottom-up approaches, in contrast, use the chemical properties of individual molecules to push them to (a) self-organize or self-assemble into some functional conformation, or (b) rely on positional assembly. These approaches utilize the concepts of molecular self-assembly and/or molecular recognition. Such bottom-up approaches should, broadly speaking, be able to produce devices in parallel and much cheaper than top-down methods, but could potentially be overwhelmed as the size and complexity of the desired assembly increases. Examples of top-down techniques exploiting molecular self-organization are: Dip-pen Lithography (DPL), Local Oxidation Nanolithography (LON), Nanoimprint Lithography (NIL) and Soft-lithography.

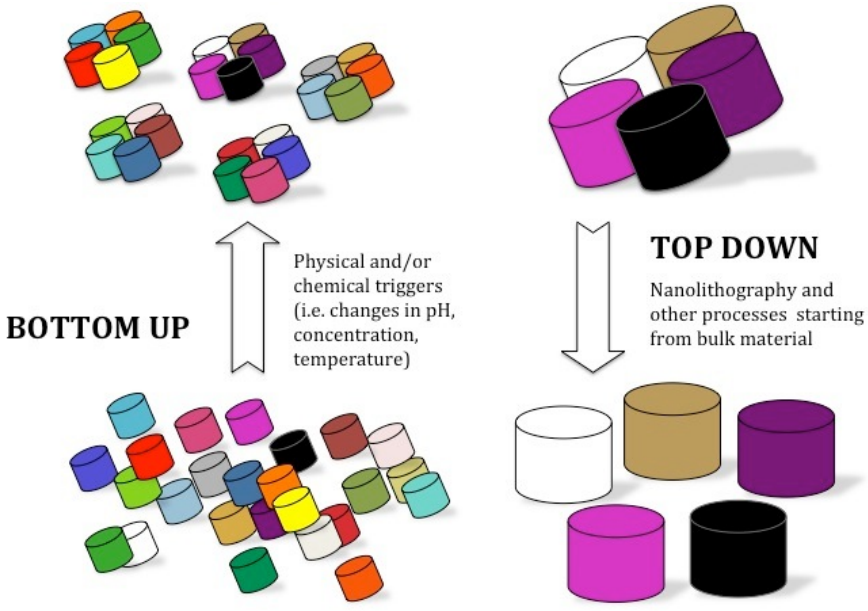

*Figure **1.1**: Bottom up and top down approaches.*

1.3 Regenerative medicine for neural cells

Regenerative medicine is an emerging branch of translational research in tissue engineering and molecular biology, which deals with the "process of replacing, engineering or regenerating human cells, tissues or organs to restore or establish normal function". In addition to the therapeutic applications, such as a tissue grown in a patient or outside the patient and then transplanted, this field holds the promise of engineering damaged tissues and organs via stimulating the body's own repair mechanisms to functionally heal previously irreparable tissues or organs [2][3].
Regenerative medicine also refers to a group of biomedical approaches to clinical therapies that may involve the use of stem cells [4].
The bases of regenerative medicine and tissue engineering for either therapeutic or diagnostic applications are the ability to exploit living cells to fabricate tissue. Many results at a preclinical level have been shown, but we are still far from its clinical application. Actually most of the *in vitro* engineered tissues are dysfunctional: this is chiefly due to our limited understanding of the very fundamental principles underlying the complexity of cell life, with a restricted capacity of encoding bioactive signals in order to guide cells through the correct pathways of differentiation and biosynthesis.
Cell functioning is, to a large extent, dependent on their microenvironment, which contains the surrounding extracellular matrix (ECM), other cells and soluble factors. Cells can sense ECM cues, such as composition, stiffness and topography signals through, for instance, integrin mediated adhesion, and can also communicate with neighboring cells[5][6]. The regulators of cell behaviors can easily classify into cell cues, ECM cues and soluble factors (Figure 1.2).

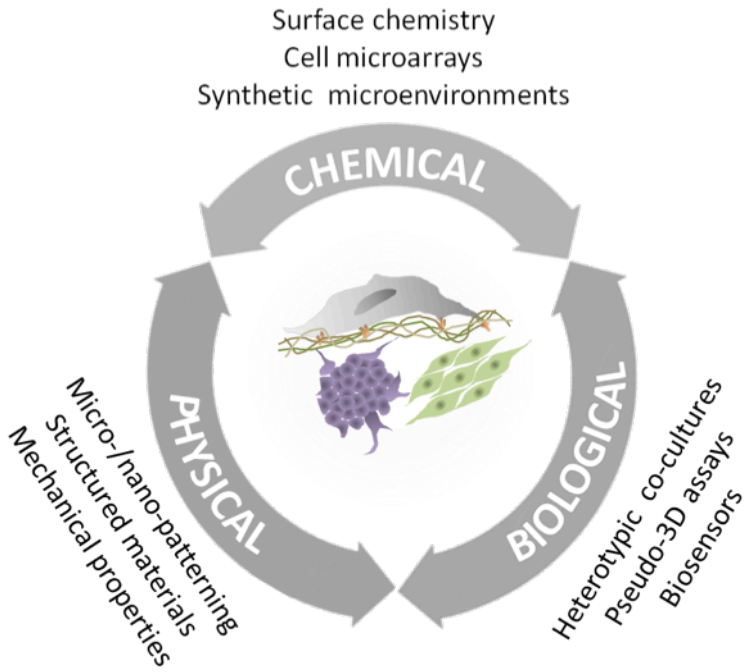

*Figure **1.2**:Physical, chemical and biological cell behavior regulators*

The current micro- and nano-technologies interfacing synthetic materials and cell biology requires a better understanding of cell-surface interactions on the micro and nanometer scale. The development of these tools provides new means to understand the fundamental relationships between cells and their surrounding microenvironment, which underlie the physiology of human tissue.

One of core studies of biomaterials in the large field of regenerative medicine relies on understanding cell-material interactions, using the development of advanced materials and the surface patterning.

A significant topic in the field of regenerative medicine is the one related to the study of the central nervous system (CNS) diseases. Unfortunately the amount of CNS diseases is large and may be due to many causes, including mechanical trauma, infections as encephalitis and poliomyelitis, neurodegenerative disorders such as Alzheimer's disease and amyotrophic lateral sclerosis, autoimmune and inflammatory diseases such as multiple sclerosis or acute disseminated encephalomyelitis, and genetic disorders such as Krabbe's disease or Huntington's disease. Finally, tumors sited in CNS can cause severe illness and, when malignant, can be fatal.

Given this wide range of pathologies, it is fundamental to create novel route for investigating neural cell response to the environment signals starting from a completely new approach.

In this thesis two different secondary human neural cell lines, viz. NE4C neuroectodermal stem cells and SH-SY5Y neuroblastoma were used as cell line models. Both the cell lines have been extensively studied for many years as model of neural cell lines, more properly NE4C as neurons-astrocytes lineage [7][8] and SH-SY5Y as neuronal one [9][10]; furthermore their culture conditions allow one to obtain reproducible data about cell adhesion and proliferation. We already know the critical role of neurons in the CNS, but in the past, the neuronal network was considered the only important part in the CNS, and astrocytes were looked upon as “gap fillers”. More recently, the function of astrocytes has been reconsidered, and they are now thought to play a number of active roles in the brain, including the secretion and internalization of neuro-transmitters, biochemical support of the endothelial cells that form the blood–brain barrier, providing of nutrients to the nervous tissue, preserving the extracellular ion balance, repairing and scarring process of the brain and spinal cord following traumatic injuries.

A third further cell line: standard fibroblasts NIH-3T3 (from mouse) obtained and characterized in 1963 by G. Todaro and H. Green and used in a wide range of research studies and biomedical application has been employed in the adhesion and proliferation tests [11].

1.4 Implantable Organic Nano-Electronics: **i-ONE** project

A large part of my PhD work has been performed in the framework of the European project iONE-FP7 funded by the European Union Seventh Framework Program (FP7/2007-2013) under grant agreement n° 280772.
As literally reported in the technical annex "The vision of iONE project is to develop and test for the first time flexible organic electronics for the development and testing of Active Multifunctional Implantable Devices (AMIDs) leading to treatment of Spinal Cord Injury (SCI)". The AMID has to be stable and safe, with high biocompatibility for reducing risk of a host versus graft immune response. The use of these flexible organic electronics devices (ultra-thin film organic field effect transistor (FET), organic electro-chemical transistor, nanoparticle organic memory FET) will (i) advance the state-of-the-art of implantable devices for SCI from passive to active layouts that will promote nerve regeneration by a combination of local stimuli delivered on demand, (ii) sense inflammation, and (iii) control the immune-inflammatory response.
My work has been devoted primarily to the mimicking of the local microenvironment for stem/precursor cell recruitment and differentiation (and delivering locally growth factors, neurotransmitters, and drugs.), by applying surfaces functionalization and micro and nanopatterning technologies.
The biomedical impact of the project has been demonstrated *in vitro* and *in vivo*. *In vitro*, the neural therapeutic plasticity induced by the iONE device has been evaluated on stem cells, which differentiated to neural progenitor cells, and then to neural cells. *In vivo*, the study of neural plasticity has been transferred to endogenous stem cells by implanting the iONE device into a contusion SCI animal model.

In conclusion, iONE, acquiring the knowledge and the technology required to regenerate the nerve in the niche of the injury, is the perfect example of nanotechnology application in regenerative medicine.

Bibliography

[1] Rajiv Saini, Santosh Saini, and Sugandha Sharma, “Nanotechnology: The Future Medicine,” *J. Cutan. Aesthet. Surg.*, vol. 3, no. 1, pp. 32–33, 2010.

[2] J. Z. Gasiorowski, C. J. Murphy, and P. F. Nealey, “Biophysical cues and cell behavior: the big impact of little things,” *Annu. Rev. Biomed. Eng.*, vol. 15, pp. 155–176, 2013.

[3] J. P. Fisher, A. G. Mikos, J. D. Bronzino, and D. R. Peterson, *Tissue Engineering: Principles and Practices*. CRC Press, 2012.

[4] A. M. Riazi, S. Y. Kwon, and W. L. Stanford, “Stem cell sources for regenerative medicine,” *Methods Mol. Biol.*, vol. 482, pp. 55–90, 2009.

[5] F. Gattazzo, A. Urciuolo, and P. Bonaldo, “Extracellular matrix: A dynamic microenvironment for stem cell niche,” *Biochim. Biophys. Acta*, vol. 1840, no. 8, pp. 2506–2519, 2014.

[6] J. Barthes, H. Özçelik, M. Hindié, A. Ndreu-Halili, A. Hasan, and N. E. Vrana, “Cell Microenvironment Engineering and Monitoring for Tissue Engineering and Regenerative Medicine: The Recent Advances,” *Biomed Res. Int.*, vol. 2014, 2014.

[7] K. Schlett, B. Herberth, and E. Madarász, “In vitro pattern formation during neurogenesis in neuroectodermal progenitor cells immortalized by p53-deficiency.,” *Int. J. Dev. Neurosci.*, vol. 15, no. 6, pp. 795–804, 1997.

[8] Z. Környei, V. Szlávik, B. Szabó, E. Gócza, A. Czirók, and E. Madarász, “Humoral and contact interactions in astroglia/stem cell co-cultures in the course of glia-induced neurogenesis.,” *Glia*, vol. 49, no. 3, pp. 430–444, 2005.

[9] R. A. Ross, B. A. Spengler, and J. L. Biedler, “Coordinate morphological and biochemical interconversion of human neuroblastoma cells,” *J. Natl. Cancer Inst.*, vol. 71, no. 4, pp. 741–747, 1983.

[10] J. Biedler, S. Roffler-Tarlov, M. Schachner, and L. Freedman, “Multiple neurotransmitter synthesis by human neuroblastoma cell lines and clones.,” *Cancer Res.*, vol. 38, no. 11 Pt 1, pp. 3751–3757, 1978.

[11] G. J. Todaro and H. Green, “Quantitative studies of the growht of mouse embryo cells in culture and their development into established lines.,” *J. Cell Biol.*, vol. 17, pp. 299–313, 1963.

Chapter 2 – Experimental and Fabrication techniques

Here an overview of the main techniques used for fabrication, patterning and characterization is provided.

2.1 Fabrication and patterning techniques

2.1.1 Laser Assisted Bioprinting (LAB)

Parallel to the "scaffold based" strategy, in which cells are seeded onto porous structures, the bioprinting approach aims at constructing three dimensional biological structures or functional organs, layer-by-layer, from the bottom up[1]. Jet-based methods to print living cells have been widely reviewed [2][3]. Historically, laser-based printing techniques, such as laser-direct-writing, matrix-assisted pulsed laser evaporation (MAPLE), laser-induced forward transfer (LIFT) etc., have been used to spatially pattern solutions in 2D. Among them, the LIFT technique allows printing inorganic as well as organic material with micrometer resolution. Initially developed to transfer metals [4], the LIFT has been successfully improved to print biological material such as peptides, DNA, and cells [5][6].
Manipulation of picoliter to nanoliter droplets has been a challenge for several applications including biochemical surface patterning, tissue engineering, and direct placement of cells and biomaterials for wound dressing applications [7][8][[9]. In this regard, ejecting droplets via an actuator has emerged as a valuable technological advance addressing the issue of precise manipulation and deposition. A LIFT based bioprinter designed to print biological material was created and named BioLP (Biological Laser Printer) by Barron et al. [10]. LIFT based bioprinters or Laser Assisted Bioprinters (LAB) are comprised of three components: (i) a pulsed laser source, (ii) a target, called 'ribbon', from which a biological material is printed, and (iii) a receiving substrate that collects the printed material. The ribbon is made of a thin absorbing layer of metal (such as gold, titanium or stainless steel) coated onto a laser transparent support (usually glass). Biomolecules or cells are prepared in a liquid solution (i.e. physiological solution, water or culture media) that is called *bioink*, and deposited at the surface of the metal film, using various methods, like spin coating or doctor blade.
The laser pulse induces vaporization of the metal film, resulting in the production of a *jet* of liquid solution, which is deposited onto the facing substrate (Figure 2.1).

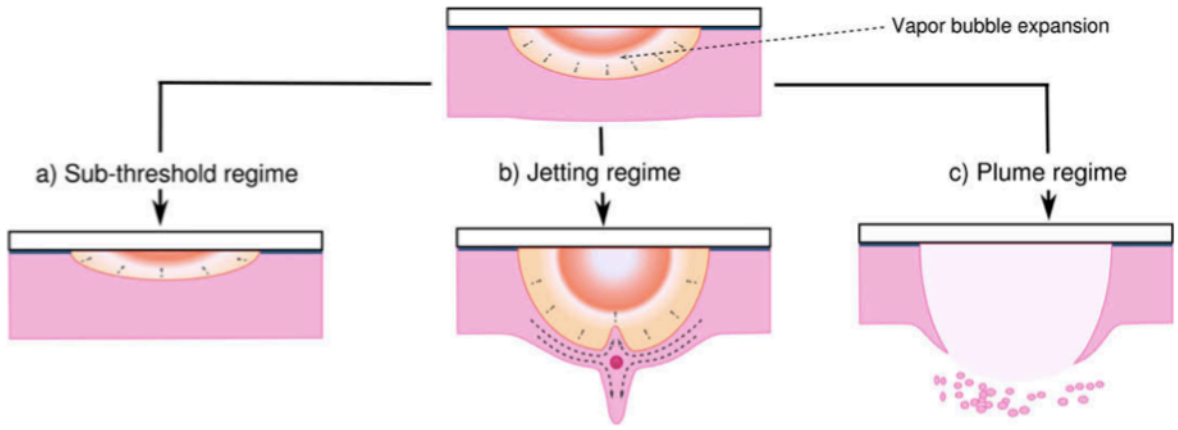

*Figure **2.1**: Mechanism for laser-induced droplet ejection. A vapour bubble is generated by vaporization of the absorbing layer and/or the first molecular layers of the liquid film. At a given viscosity, depending on bubble dynamics, jetting (b) is observed for intermediary values of fluences. For lower fluences (a), the bubble collapses far from the free surface without generating a jet. For high fluences (c), the bubble bursts to the surface, generating sub-micrometer droplets. Increasing viscosity leads to increased threshold values between the subthreshold, jetting and plume regimes*

To control the surface tension effects during printing, glycerol 1:1 is added to the final volume of the solution. Glycerol is a simple polyol (sugar alcohol) compound, colorless, odorless, very viscous and widely used in pharmaceutical formulations. Glycerol has three hydroxyl groups that are responsible for its solubility in water and its hygroscopic nature. Glycerol improves the process not only because of his high viscosity that helps in the creation of the bioink jet, but also because glycerol is not toxic and does not alter the bioink molecules features (i.e. protein structure or cell fate).
Non-contact printing is obtained through a jet formation which occurs, at a microsecond time scale, above a laser energy density threshold whose value depends on the rheological properties of liquid films and the thickness of the metallic absorbing layer [11]. By analogy with other studies in physics, it has been proposed that jet formation could be related to bubble dynamics [12], [13]. Bubble growth depends mainly on viscosity and surface tension of the liquid, while bubble collapsing is related to the distance between the bubble front and the free surface.
Considering the LAB, the resolution of printing, i.e. the size and proximity of the printed droplets, depends on parameters like the thickness of the layer of the bioink coated onto the ribbon, the surface tension and the viscosity of the bioink, the wettability of the substrate, the laser fluence, the air gap between the ribbon and the substrate [11]. The compromise between these parameters in order to obtain the desired resolution of printing may thus vary depending on the type of material being printed. The influence of these parameters on jet formation is still under investigation [14]. Therefore, controlled bioprinting (i.e. absence of splashing, controlled size of the liquid droplet) by LAB remains challenging and the highest resolution of cell printing has not yet been attained (Fig. 2.1).

LAB Applications

Laser Printing was first investigated for the fabrication of microelectronic circuits. Thereby, lines of conductive material were printed to connect micro devices or as antennas [15]. For biological applications, different groups printed cells, proteins and DNA [16][17]. Serra et al. printed a biosensor, consisting of micrometric patterns of deposited droplets containing DNA [18]. After deposition, the microarray was hybridized with the complementary strands of the transferred DNAs, each kind tagged with a different dye. The fluorescence assay was positive, demonstrating that hybridization occurred only in the droplets where specific DNA was deposited. This study demonstrates LIFT techniques as a suitable strategy for biosensors preparation without significant biomolecular damage during the laser printing procedure. Furthermore, pieces of tissue from a histological section or living adherent cells located on a polymer foil have been printed by Vogel et al [19].

In this thesis, Laser Assisted Bioprinting has been performed using ScribaR Laser Marker (Figure 2.2).

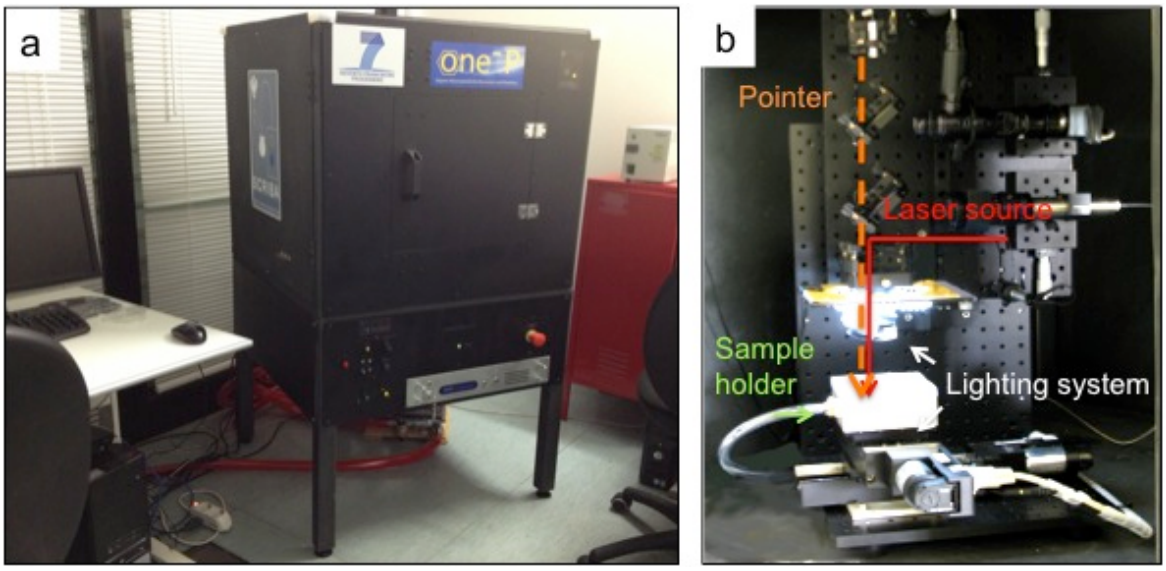

*Figure **2.2**: (a) ScribaR Multifunctional Laser Marker. (b) The ScribaR chamber with the sample holder, the lightning and microscope-camera system. The laser beam remains focused on the same point, while the sample holder is moving (in x, y, z) due to a very accurate micrometric motor stage.*

2.1.2 Soft Lithography

Soft lithography refers to a family of techniques for fabricating or replicating structures using "elastomeric stamps, molds, and conformable photomasks". It is called "soft" because it uses elastomeric materials, most notably PDMS (polydimethylsiloxane). Soft lithography is generally used to construct features measured on the micrometer to nanometer scale.
Photolithography, since 1959, has always been the most successful technology in microfabrication. The photolithographic techniques currently used for manufacturing microelectronic structures are based on a projection-printing system in which the image of a reticle is reduced and projected onto a thin film of photoresist that is spin-coated on a wafer through a high numerical aperture lens system.
Microelectronics is based on photolithography and associated techniques that are used for fabricate integrated circuits. Microelectromechanical systems are made-up by silicon micromachining; these techniques were the first to be improved to the manufacture of microstructures for biological research. The first example was the use of photolithography in the fabrication of DNA arrays [20], [21]. Anyway, photolithography is limited in its application to biotechnology and biology for several reasons: is intrinsically expensive (for most applications, cost is a dominant parameter), it gives limited control over surface properties, is often not directly suitable for proteins and cells, the time procedure to reach a prototype from a design can be long, and the techniques are unfamiliar and inaccessible to most biologists.
For fabricating microstructures for biological applications, soft lithography overcomes many of the limitations of photolithography because it allows working with water solutions thus allowing controlling the molecular structure of surfaces by patterning complex molecules such as proteins or nucleic acids [22]. A number of non-photolithographic techniques have been demonstrated for fabricating (and in some cases for manufacturing) high-quality microstructures and nanostructures: microcontact printing (μCP), replica molding (REM), microtransfer molding (μTM), micromolding in capillaries (MIMIC) and solvent-assisted micromolding (SAMIM) and Lithographically Controlled Wetting (LCW). PDMS, the most used elastomeric material, is supplied, in its most widely commercialized version (Sylgard 184, Dow Chemicals), as two components, a base and a curing agent. PDMS displays many relevant properties. It has a Young's modulus that makes it a moderately stiff elastomer (1 MPa). It is nontoxic and readily available commercially. It is intrinsically very hydrophobic (advancing contact angle of water of 110°), but its surface can be converted to a hydrophilic form (±10°) by common plasma treatments.

Lithographically controlled wetting (LCW)

LCW is a simple, fast and sustainable wet-patterning process that exploits the self-organization of soluble materials, that allows a fine spatial control provided by the

features of the employed stamp [23]. In principle, LCW can be used with any soluble compound or material. It can be performed without special instrumentation and does not require a clean room. Compared with other lithographic methods, LCW does not rely on specific interactions between the molecules and the surface; therefore, it has a wide range of potential applications, as demonstrated by the large variety of soluble materials reported in the literature to which it could be applied. Although LCW was developed originally for patterning organic semiconductors, its application was extended to many functional materials such as inorganic salts, coordination compounds, coordination polymers, molecular magnets, nanoclusters, electroluminescent compounds, sensing materials for pH and others.

Recently, LCW was also applied to biomolecules, where it can have an important role in the fabrication of biomaterial interfaces in biologically inspired applications and in medical devices. LCW has been already applied in some experiments for fabricating patterns aimed to guide the adhesion, migration and proliferation of cells [24].

A schematic overview of the LCW process is shown in Figure 2.3.

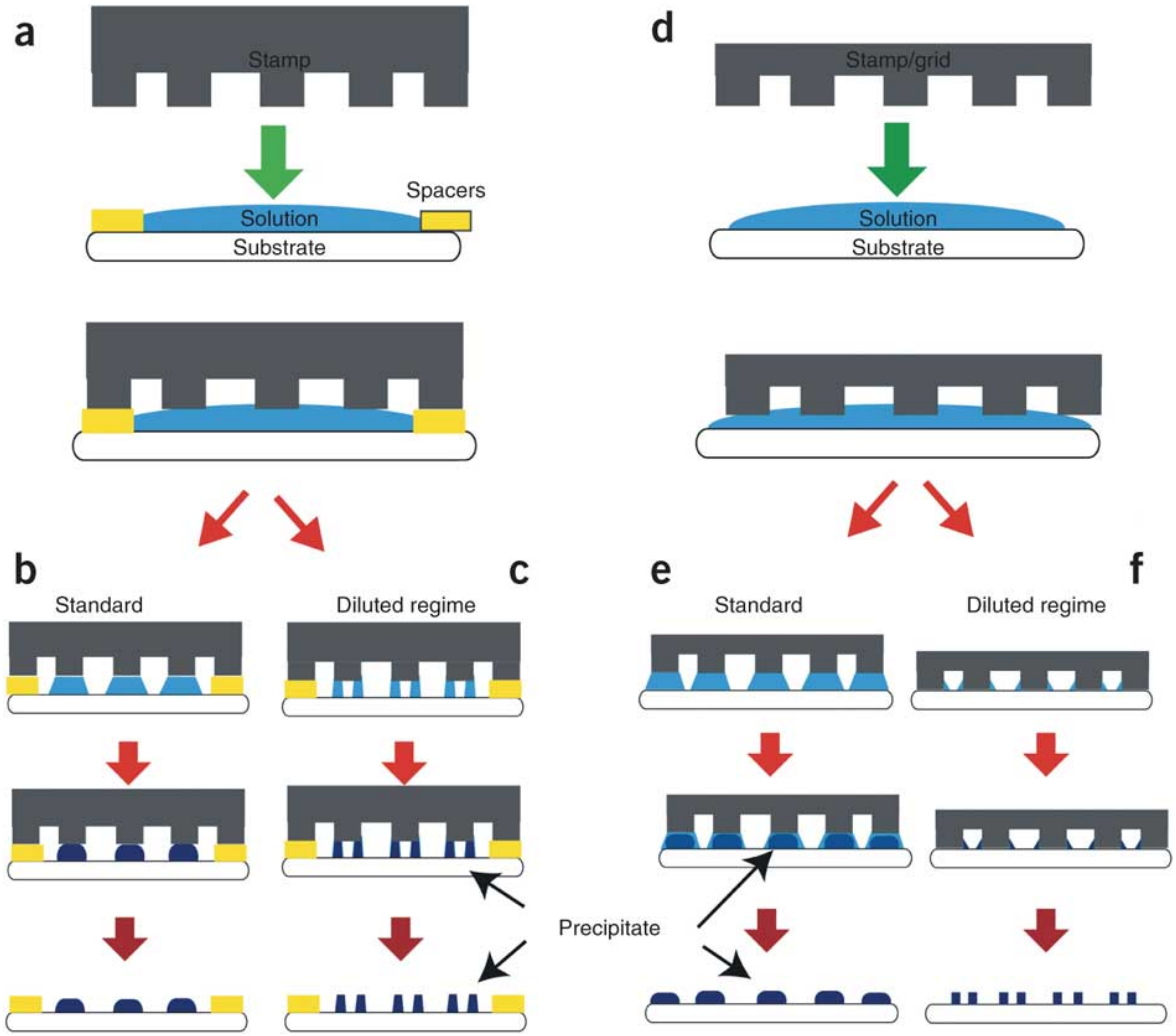

*Figure **2.3**: LCW (**a**–**c**) Scheme of printing using prefabricated spacers (**a**) in the standard (**b**) and diluted (**c**) regime. (**d**–**f**) Scheme of printing using a floating stamp (**d**) in the standard (**e**) or diluted (**f**) regime.*

When a stamp is placed in contact with a liquid thin film spread on a substrate, instability of the fluid layer develops and capillary forces pin the solution to the stamp protrusions, giving rise to an array of menisci. As the solvent evaporates, the solution forms a subfemtoliter fluid cell under each stamp protrusion (assuming a stamp feature ranging between 100 and 500 nm and a stamp- substrate distance between 50 and 200 nm, sizes commonly used in LCW). When the solution reaches supersaturation, the solute precipitates onto the substrate within the menisci, giving rise to a deposit replicating the protrusion of the stamp.

Microcontact Printing (μCP)

Microcontact printing is the most famous soft-lithographic method: the strategy is using a relief patterns onto an elastomeric stamp of PDMS to create patterns of self-assembled monolayers (SAMs) of a printable compound (the ink) on the surface of a substrate through conformal contact. Its potential applications range from microelectronics and surface chemistry to cell biology. It requires printable materials chemically grafted to the substrate or able to form SAMs. The procedure is remarkably simple and is showed in Figure 3.4. An elastomeric PDMS stamp is used to transfer molecules of the ink to the surface of the substrate by contact. After printing, a different SAM can be formed on the underivatized regions by washing the patterned substrate with a dilute solution containing the second molecule (Figure 2.4).

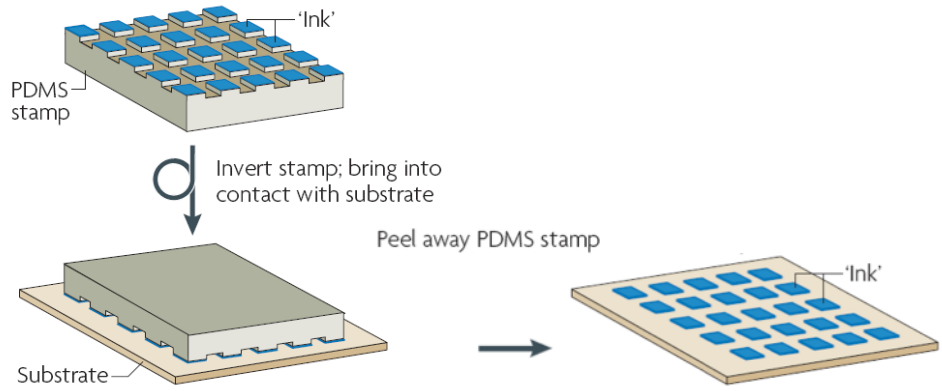

*Figure **2.4**: μCP technique scheme.*

Replica Molding (REM)

Replica molding duplicates the information, such as the shape, the morphology, and the structure, present in a master (Figure 2.5). It is a procedure that accommodates a wide range of materials. It also allows duplication of 3D topologies in a single step, whereas photolithography is not able to replicate such structures. It has been used for the mass production of surface relief structures such as diffraction gratings, holograms, compact disks (CDs), and micro tools. Replica molding with an appropriate material (usually in the form of a precursor) enables highly complex structures in the master to be faithfully

duplicated into multiple copies with nanometer resolution in a reliable, simple, and inexpensive way. The fidelity of replica molding is determined by van der Waals interactions, wetting and kinetic factors such as filling of the mold. These physical interactions should allow more accurate replica of features that are smaller than 100 nm than does photolithography, which is limited by optical diffraction.

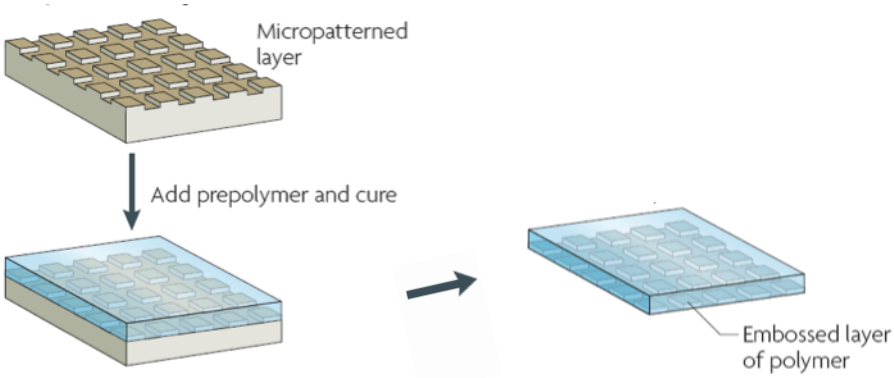

*Figure **2.5**: Replica Molding technique scheme.*

2.1.3 Electrochemical desorption of Self-Assembled Monolayers

Self-assembled monolayers (SAM) of organic molecules are molecular assemblies formed spontaneously on surfaces by adsorption and are organized into more or less large ordered domains. In nature, self-assembly results in supermolecular hierarchical organizations of interlocking components that provides very complex systems [25]. SAMs offer unique opportunities to increase fundamental understanding of self-organization, structure-property relationships, and interfacial phenomena. The ability to tailor both head and tail groups of the constituent molecules, makes SAMs excellent systems for a more fundamental understanding of phenomena affected by competing intermolecular, molecular-substrates and molecule-solvent interactions like ordering and growth, wetting, adhesion, lubrication, and corrosion. SAMs being well defined and accessible are good model systems for studies of physical chemistry and statistical physics in two dimensions and the crossover to three dimensions.
SAMs provide the needed design flexibility, both at the individual molecule and at the material levels and offer a vehicle for investigating both specific interactions at interfaces and the effect of increasing molecular complexity on the structure and stability of two-dimensional assemblies.
SAMs are ordered molecular assemblies formed by the adsorption of an active surfactant on a solid surface [26] (Figure 2.6).

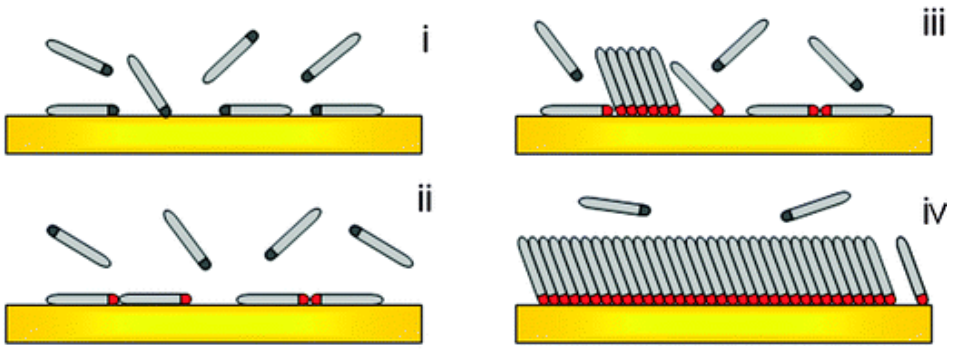

*Figure **2.6**: Scheme of the different steps taking place during the self-assembly of alkanethiol on Au: (i) physisorption, (ii) lying down phase formation, (iii) nucleation of the standing up phase, (iv) completion of the standing up phase.*

This simple process makes SAMs inherently manufacturable and thus technologically attractive for building superlattices and for surface engineering. The order in these two-dimensional systems is produced by a spontaneous chemical arrangement at the interface as the system approaches equilibrium.

In our experiments, oligo ethylene-glycol-terminated alkylthiols (HS-(CH2)11-(OCH2CH2)6-OH: TOEG6) were used for generating a SAM on a thin gold layer deposited on a glass slice.

Electrochemical desorption (ECD) of self-assembled monolayers is an important process that can dynamically modify surface properties: an electrical stimulus is used to desorb molecules that form SAM by breaking the chemical bond between Au and S:

$$Au - SR + e^- \rightarrow Au^0 + RS^-$$

Electrical stimulus can also be used to modify electronic state or molecular conformation of SAMs, and to help deposit molecules of SAMs. Although the assembly of alkanethiols onto Au is a spontaneous process, its stability varies at different range of electrochemical potentials. To conduct an ECD we need at least two electrodes. The *working electrode*, which makes contact with the SAM, must apply the desired potential in a controlled way and facilitate the transfer of charge to and from the sample. A second electrode acts as the other half of the cell and must have a known potential with we measure the potential of the working electrode, furthermore it must balance the charge added or removed by the working electrode. While this is a viable setup, it has a number of limitations: it is extremely hard for an electrode to maintain a constant potential while passing current to counter redox events at the working electrode. To solve this problem, two separate electrodes have the individual roles of supplying electrons and providing a reference potential. The *reference electrode* is a half cell with a known reduction potential and it acts as reference in measuring and controlling the *working electrode*'s potential and at no point does it pass any current. Then we have a *counter electrode* that passes all the current needed to balance the current observed at the

working electrode. These three electrodes, the *working*, *reference*, and *counter*, make up the "three electrode system".

For studies of ECD, SAMs are usually immersed in an aqueous or ethanol solution with an electrolyte, for example KOH, at a neutral or basic pH. Both the thiolates and the bare Au surface become solvated. The potential is applied between the working electrode and the reference electrode while the current is measured between the working electrode and the counter electrode. The thiols diffuse from the surface or sometimes tend to remain on the electrode surface and form a molecular assembly, preventing the residual SAM from desorbing and even redeposited repetitively onto the Au surface. Desorption process is reversible: the thiols can re-adsorb onto the Au surface when the applied negative potential is removed [27]. The potential at which the desorption of the SAMs occurs depends on several factors, such as the length of the alkyl chain, the degree of ordering and the number of intermolecular interactions within the organic film, and the crystallinity of the substrate (Au) [28].

A typical desorption potential for n-alkanethiolates is -1.0 V with respect to an Ag/AgCl (satd. KCl) reference electrode. Thiols with short chain tend to undergo reductive desorption at potentials less negative than -1.0 V.
Various methods can be used to characterize ECD, such as cyclic voltammogram (CV), chronoamperometry, electrochemical quartz crystal microbalance, surface plasmon resonance (SPR), fluorescence microscopy, scanning tunneling microscopy (STM) and so forth.

2.1.4 Nanografting

This technique combines Atomic Force Microscopy (AFM, see below, section 2.2.2) with SAM functionalized surfaces. Using an AFM tip it is possible to "scan" the SAM and *scratch* it along a defined pattern. As a higher force is applied during the scanning, the matrix thiol molecules are removed by the tip and transported into the solvent. Thiol molecules contained in the solution immediately adsorb onto the freshly exposed gold area following the scanning track of the atomic force microscope tip to form designed nanostructures. The produced nanopatterns can then be characterized in situ by the same atomic force microscope tip at a reduced force.
The whole procedure occurs in liquid environment: more specifically, the solution that contains a different *self-assembly* molecule that one wants to replace the first one (Figure 2.7).

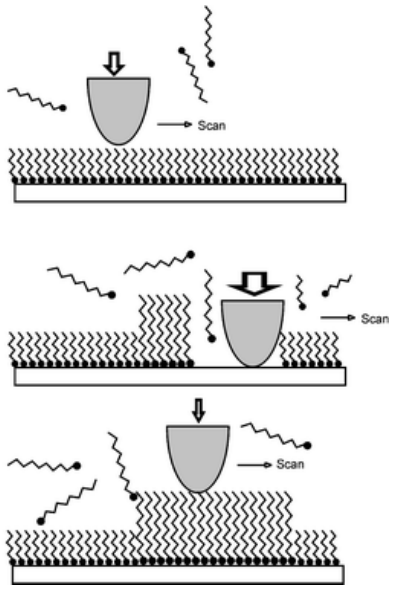

*Figure **2.7**: Nanografting scheme. An AFM tip reaches the SAM and, landing on it, begins to scratch the monolayer. The empty space is filled by another molecule.*

Tip force, scanning speed and lines density per units of area, are adjustable for locally modify SAM structure and molecules packing. AFM tip induces mechanical stress that allows local exchanges of surface material with molecules in the liquid suspension. Otherwise, friction forces between tip and surface can provide extra thermal energy for overtaking desorption energetic barrier, as observed by J. Liang in DNA nanografting [29].
Nanografting technique shows very critical opportunities in the field of nanomaterials and in the nanotechnology sector, allowing fabrication of nanostructures with functional groups as –OH, -COOH, -CHO, -NH_2, NHS, biotin, -CF_3, carbohydrates and nucleotides. This versatility has been demonstrated by the fabrication of patches of objects displaying of large sizes such as metal nanoparticles (NPs), DNA and proteins [30].

2.2 Characterization techniques

2.2.1 Scanning Electron Microscopy (SEM)

The scanning electron microscope (SEM) uses a focused beam of high-energy electrons to generate a variety of signals at the surface of solid specimens. The signals that derive from electron-sample interactions reveal information about the sample including external morphology (texture), chemical composition, crystalline structure and orientation of materials making up the sample. In most applications, data are collected

over a selected area of the surface of the sample and a 2-dimensional image is generated that displays spatial variations of these properties. Areas ranging from approximately 1 cm to 5 microns in width can be imaged in a scanning mode using conventional SEM techniques (magnification ranging from 20X to approximately 30,000X, spatial resolution of 50 to 100 nm). The SEM is also capable of performing analyses of selected point locations on the sample; this is especially useful in qualitatively or semi-quantitatively determination of the chemical compositions (using Energy Dispersive X-ray Spectrometry, EDS), crystalline structure, and crystal orientations (using Electron Back Scattered Diffraction, EBSD).

Accelerated electrons carry significant amounts of kinetic energy and this energy is dissipated by electron-sample interactions when the incident electrons are decelerated in the solid sample. These signals produced by this interaction include secondary electrons (that produce SEM images), backscattered electrons (BSE), diffracted backscattered electrons (EBSD that are used to determine crystal structures and orientations of minerals), photons (characteristic X-rays that are used for elemental analysis and continuum X-rays), visible light (cathodoluminescence–CL) and heat. Secondary electrons and backscattered electrons are commonly used for imaging samples: secondary electrons are most valuable for showing morphology and topography on samples and backscattered electrons are most valuable for illustrating contrasts in composition in multiphase samples (i.e. for rapid phase discrimination). X-ray generation is produced by inelastic collisions of the incident electrons with electrons in discrete orbitals (shells) of atoms in the sample. As the excited electrons return to lower energy states, they yield X-rays of a fixed wavelength (that is related to the difference in energy levels of electrons in different shells for a given element). Thus, characteristic X-rays are produced for each element in a mineral that is "excited" by the electron beam (Figure 3.8).

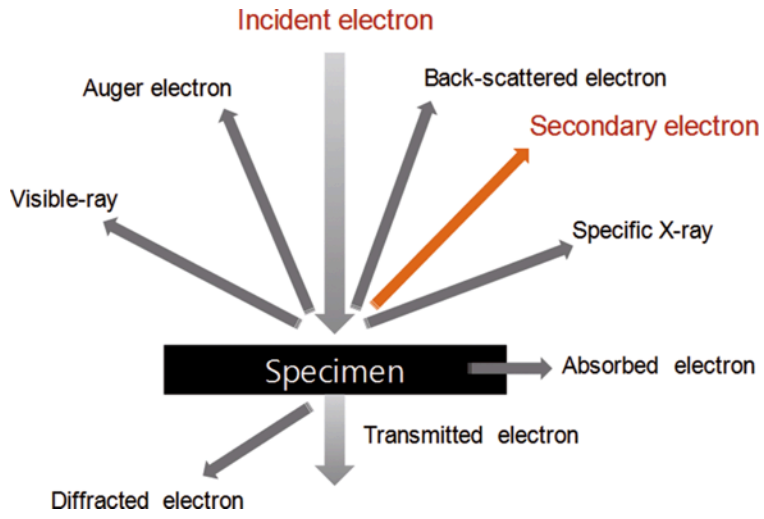

*Figure **2.8**: Scheme of the interaction between an electron beam and the sample.*

SEM analysis is considered to be "non-destructive"; that is, x-rays generated by electron interactions do not lead to volume loss of the sample, so it is possible to analyze the same materials repeatedly.
Essential components of all SEMs include: electron Source ("Gun"), electron lenses, sample stage, detectors for all signals of interest, display / data output devices. Infrastructure requirements are: power supply, vacuum system, cooling system, vibration-free floor, room free of ambient magnetic and electric fields.
SEMs always have at least one detector (usually a secondary electron detector), and most have additional ones. The specific capabilities of a particular instrument are critically dependent on which detectors it accommodates.
In our laboratory we use a Hitachi S4000 SEM (Figure 2.9), a high-resolution microscope with a cold cathode field emission electron source (FESEM).

*Figure **2.9**: SEM Hitachi S4000*
(Institute for the Study of Nanostructured Materials, CNR-Bologna, Italy).

The SEM also has a solid-state backscattered electron detector for atomic contrast imaging. The ease of use and high resolution makes it very versatile for many users' applications, complementing the other microscopes in the unit. Resolution can be 1.5nm guaranteed at 30kV with a working distance of 5mm, magnification goes from 20x to 300,000x. Hitachi S4000 works with an accelerating voltage in a range 0.5 to 30kV. The imaging system used is a Quartz PCI image management system.

In the electron column is located the electron gun, with two or more electromagnetic lenses that operate in vacuum. This electron gun generates free electrons and accelerates them to energy in a range 1-40 keV. The aim of the lenses is to create a small, focused electron probe on the sample. Electron lenses are cylinders of metal with cylindric hole and operate in vacuum. Inside them is generated a magnetic field that

focused or defocused the electron beam passing through the hole. To focus the electron probe to a smaller size, there are one to three condenser lenses in which the strength is variable. First and second condenser lenses control the amount of demagnification; usually the third one (the 'final lens') is improperly called *objective* because it focuses the beam on the specimen. The final aberration and resolution of the lens is controlled by an aperture, which affects the beam convergence angle α, but also regulates the current and the depth of field. If the convergence angle is small, we have a greater depth of field.

Lens defects or contamination, like processing errors and asymmetry in lens twisting, on apertures or column can cause modification in shape of the cross section of the electron beam profile. The result is that the image will stretch along different direction. This effect is called *astigmatism* and is corrected by a series of coils surrounding the electron beam. This compensation for astigmatism is better performed at higher magnification.

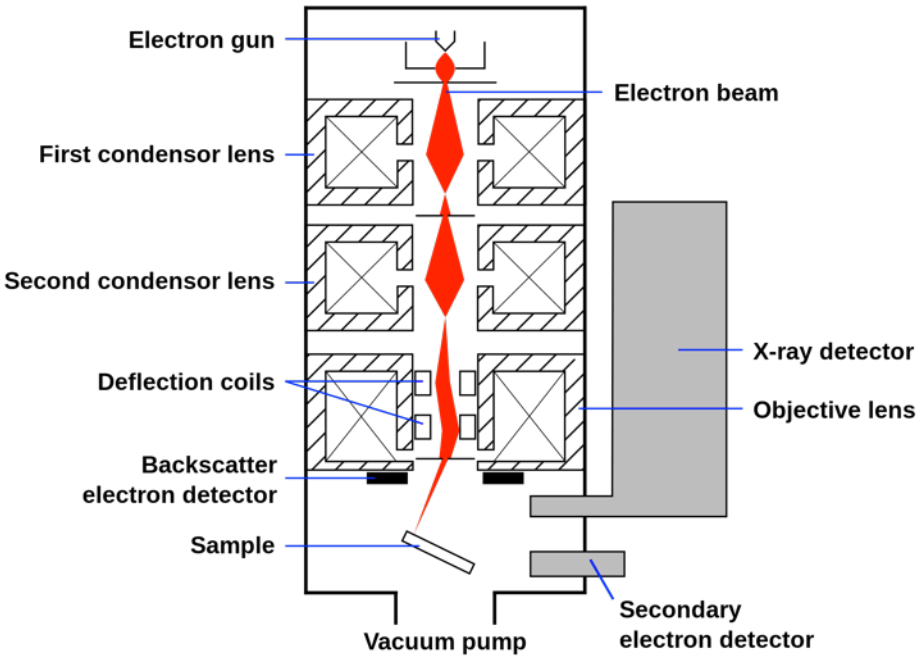

*Figure **2.10**: Schematic of an SEM.*

The SEM image is a 2D intensity map in the analog or digital domain. Each image pixel on the display corresponds to a point on the sample, which is proportional to the signal intensity captured by the detector at each specific point. In an analog scanning system, the beam is moved continuously; with a rapid scan along the X-axis (line scan) supplemented by a stepwise slow scan along the Y-axis at predefined number of lines. In digital scanning system, only discrete beam locations are allowed. The beam is positioned in a particular location, remains there for a fixed time, called dwell time, and then it is moved to the next point.

SEM magnification is achieved by scanning an area on the specimen, which is smaller than the display. Since the monitor length is fixed, increase or decrease in magnification

is achieved by respectively reducing or increasing the length of the scan on the specimen. It depends only on the excitation of the scan coils and not on the excitation of the objective lens, which determines the focus of the beam. The magnification of the SEM image is then changed by adjusting the length of the scan on the specimen (L_{sample}) for a constant length of scan on the monitor ($L_{display}$), which gives the linear magnification of the image (M)

$$\text{Magnification} = L_{display}/L_{sample}$$

The SEM column, gun, and specimen chambers are all kept under a vacuum of 10^{-6} Torr for achieving the right electron optics performance. High vacuum environments are unfamiliar to most forms of life due to the nearly 80% water content of cells and tissues. Even small biomolecules need a hydration shell to remain in a natural active state. This incompatibility of water rich specimens with standard electron microscope vacuum system requires a sample preparation to bereave them of all the fluids that would degas in high vacuum. Therefore, all samples placed in a SEM must be dried of fluids in order to be stable for secondary electron imaging.

The strategy followed to preserve the structural features of organisms, organs, tissues, cells and biomolecules is to chemically fix them into a rigid state with cross-linkers and then load them with heavy metal salts to enhance the mass density of the components. Biological samples are first cross-linked with glutaraldehyde, a dialdehyde that contains five carbon atoms. When this molecule is buffered and the biological sample is either perfused or immersed in it, it reacts with the amino groups of amino acids thereby releasing $2H_2O$ molecules and cross-linking the peptide chains. Thus, movement of all protein components of cells and tissues are prevented. Biological samples are then "postfixed" with osmium tetroxide that is believed to interact with the unsaturated fatty. Since OsO_4 contains the heaviest of all elements, it serves to add electron density and scattering properties to otherwise low contrast biological membranes. OsO_4 also acts as a mordant that interacts with itself and with other stains [31]. Subsequent to fixation, the aqueous content of the sample is replaced with an intermediate fluid, usually an organic solvent such as ethanol or acetone before drying. The dehydration procedure that we have employed uses ethanol or acetone in a graded series such as 50%, 75%, 95% and then several washes with pure 100% solvent. Caution should be exercised not to remove too much of the bulk fluid and expose the sample surface to air. A better method is a linear dehydration gradient that requires an exchange apparatus that slowly increases the intermediate fluid concentration and serves to reduce osmotic shock and shape change in the specimen [32]. This method is called Critical Point Drying (CPD). Biological specimens dried in air are greatly distorted by surface tensional processes; CPD involves taking the fluid in which a specimen is dipped to its critical point; that is the temperature and pressure at which the liquid changes from liquid to gas (and vice versa). At this point, surface tension is zero and fluid may be released from the tissue causing the minimal amount of morphological change. However, this method is not appropriate for high-resolution SEM of nanometer-sized structures since the drying

procedure removes the hydration shell from bioorganic molecules that could thus collapse over the 1–10 nm range. The very last step consists in coating the sample with a thin layer of metal; in the experiments reported in this thesis work few nanometers of gold sputtered in a saturated atmosphere of argon were used.

2.2.2 Atomic Force Microscopy (AFM)

Unlike Scanning Electron Microscope, the AFM does not rely on electromagnetic radiation, such as photon or electron beams, to create an image. AFM is a mechanical imaging instrument that measures the 3D topography as well as physical properties of a surface with a sharpened probe. The probe is positioned close enough to the surface such that it can interact with its force fields, the probe is then scanned across the surface; in the most common imaging mode the forces between the probe and the sample are kept constant. An image of the surface is reconstructed by monitoring the precise motion of the probe as it is scanned over the surface. Typically the probe is scanned in a raster-like pattern. Piezoelectric materials are commonly used for controlling the motion of the probe as it is scanned across a surface in an AFM.
In an AFM the probe is very sharp, typically less than 50 nanometers in diameter and the areas scanned by the probe are less than 100 um (some instruments exist with very large scanned area but they are usually devoted to very specific applications). There are not fixed limitation to the height of surface features scanned with an AFM, nevertheless, with the commonly available scanner, they have to be less than 20 um. Scan times can range from fraction of seconds to minutes depending on the size of the scan, the height of the topographic features and the scanner.

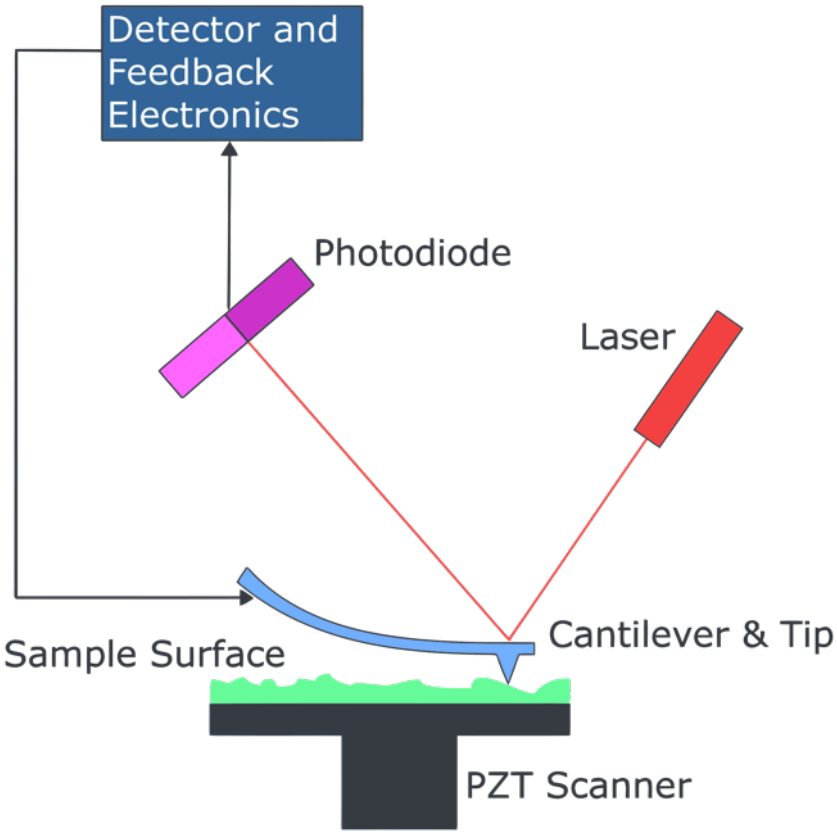

*Figure **2.11**: Block diagram of AFM using beam deflection detection. As the cantilever is displaced via its interaction with the surface, so too will the reflection of the laser beam be displaced on the surface of the photodiode.*

A light lever is the force sensor of an atomic force microscope; the output from a laser is focused on the backside of a cantilever and reflected into a photo-detector with two sections. The output of each of the photo-detector sections is compared in a differential amplifier. When the probe interacts with the surface, the cantilever curves, and the light path changes causing the amount of light in the two photo-detector sections to change. Thus the electronic output of the light lever force sensor and the force between the probe and sample are proportional.
Although the AFM is capable of extreme magnification, it is not a large instrument and can be easily installed in a laboratory on a desktop. The greatest deterrent to high magnification with the AFM is often environmental vibrations that cause the probe to have vibrations that prevent the imaging over very small scales. Although the AFM is an amazing instrument for visualizing and measuring nanometer scale features, it has several characteristics that make it unique. For example the ratio between dimensions and atomic-scale sensitivity: most measuring instruments become larger when greater sensitivity is required. With an AFM the sensitivity is built-in at the nanometer or atomic scale. Thus to make the instrument more sensitive, there is no need to make it larger. An AFM may be used also for rapidly making changes in surface structures at the nanometer scale. Such changes can be made for a fraction of the amount it would cost

with traditional technologies such as e-beam or photolithography. Finally, very important is the motion control: a precise motion control technology is required to accurately scan and position the probe in an AFM at the nanometer scale. Such accurate motion control technology allows cost effective motion control at a level not achievable with other methods.
These three unique characteristics may be applied to other technological and scientific areas such as data storage, genetic engineering and nano-robotics.

AFM vs other microscopes

The AFM can be compared to traditional microscopes such as the optical or scanning electron microscopes for measuring two-dimension morphology. However, it can also be compared to profilometers (optical or stylus) for making measurements in the vertical axis thus providing a real topography. One of the great advantages of the AFM is the ability to magnify in the X, Y and Z axes.
When compared to a profilometer, the AFM has a greater X-Y resolution because the AFM probe is much smaller than the profilometer stylus and compared to the optical instruments it is not limited by the optical diffraction law.
The length scale of an optical microscope overlaps nicely with an AFM. Thus, an AFM can be combined with an optical microscope and with this combination it is possible to have a field of view dynamic range from mm to nm. In practice, an optical microscope is typically used for selecting the location for AFM scanning. The AFM is most often compared with the electron beam techniques such as the SEM or TEM. In general, it is easier to learn to use an AFM than an SEM because there is minimal sample preparation required with an AFM. One can say that with an AFM, if the probe is good, a good image is measured.
SEM/TEM instruments are capable of doing much more than topography measurements. For example, electron beam instrumentation can do EDX measurements or even electron beam initiated lithography. Likewise, the AFM can make many types of measurements other than AFM topographical measurements. For example, AFM instruments can make thermal, magnetic and electric field maps of a surface. Like the SEM/ TEM, an AFM can also initiate lithographic changes on a surface. Although the time required for making a measurement with the SEM image is typically less than an AFM, the amount of time required to get meaningful images is similar. This is because the SEM/TEM often requires substantial time to prepare a sample. With the AFM, little or no sample preparation is required. In comparison with an optical microscope and the SEM/TEM an AFM is more difficult to use than the optical microscope and easier to use than the SEM/TEM. Lastly, an optical microscope requires the least amount of laboratory space, while the SEM/TEM requires the most amount of laboratory space. The AFM is typically between these two. Finally, in comparison to an optical profiler, the AFM is more difficult to use. This is because the optical profilometer need almost no adjustments while the AFM requires the adjustments of at least few parameters such as the scan speed and the feedback control.

AFM Instrumentation

The basic components of an AFM are a computer, a control electronics and a stage.

- Computer: a Software is used for controlling the microscope, acquiring and displaying images. The software is often used also for processing and analyzing AFM images.

- Control Electronics: The control electronics generate the electronic signals required for moving stage components such as the Z motors and the XYZ scanner. The control electronics also digitize the images measured in the stage so that they can be displayed by the computer.

- Stage: An AFM stage is where the sample is placed when an image is measured.
Typically, the AFM stage includes an AFM scanner and an optical microscope, along with motion control systems for moving the scanner relative to a sample in the X-Y-Z axis.

In this work a Smena Scanning Probe Microscopy consisting of stand alone head, where the piezo scanner is positioned inside the head has been used (Figure 2.12). The geometry of the piezo consists of three blocks of piezoelectric ceramic, allowing the movement of the tip along the three orthogonal directions x, y, z.

*Figure **2.12**: a) NT-MDTTM Smena Standalone head, b) AFM equipment (Institute for the Study of Nanostructured Materials, CNR-Bologna, Italy).*

The most important part of an AFM is the probe, a consumable measuring device with a sharp tip on the free-swinging end of a cantilever that is protruding from a holder plate. The dimensions of the cantilever are in the scale of tenths of micrometers while the radius of the tip is in the scale of a few nanometers. The holder plate, also called *holder chip* - often 1.6 mm by 3.4 mm in size - allows the operator to hold the AFM probe with tweezers and fit it into the corresponding holder clips on the scanning head of the Atomic force microscope. This complete device is most commonly called an "AFM

probe", but other names include "AFM tip" and "cantilever" (employing the name of a single part as the name of the whole device). AFM probes are manufactured with MEMS technology. Most AFM probes used are made from silicon (Si), but borosilicate glass and silicon nitride are also in use. As already described, the tip is carried very close to the surface of the object under investigation, thus the cantilever is deflected by the interaction between the tip and the surface, which is what the AFM is designed to measure. A spatial map of the interaction can be made by measuring the deflection at many points of a 2D surface.

Several types of interaction can be detected. Depending on the interaction under investigation, the surface of the tip of the AFM probe may need to be modified with a coating.

The surface of the cantilevers can also be modified. These coatings are mostly applied in order to increase the reflectance of the cantilever and to improve the deflection signal.

Imaging modes

AFM operation is usually described as one of three modes, according to the nature of the tip motion: (1) contact mode, also called static mode (as opposed to the other two modes, which are called dynamic modes); (2) tapping mode, also called intermittent contact, AC mode, or vibrating mode, or, after the detection mechanism, Amplitude Modulation AFM; (3) non-contact mode, or, again after the detection mechanism, Frequency Modulation AFM.

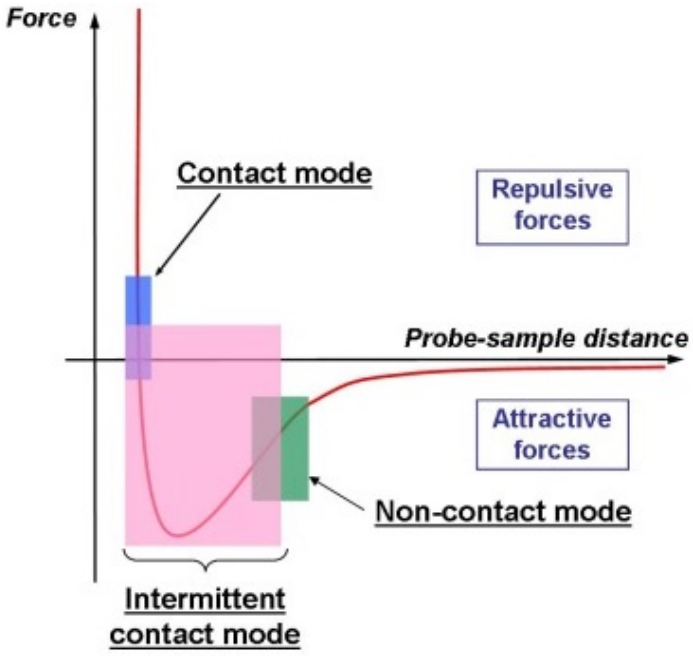

*Figure **2.13:** Plot of force as a function of probe-sample separation.*

Contact mode - In contact mode, the tip is "dragged" across the surface of the sample and the surface is measured either using the deflection of the cantilever directly or, more commonly, using the feedback signal required to keep the cantilever at a constant force. Because the measurement of a static signal is prone to noise and drift, low stiffness cantilevers are used to improve the deflection signal. Close to the surface of the sample, attractive forces can be quite strong, causing the tip to "snap-in" to the surface. Thus, contact mode AFM is almost always done at a depth where the overall force is repulsive, that is, in firm "contact" with the solid surface below any adsorbed layers.

Tapping mode - In ambient conditions, most samples develop a liquid meniscus layer thus, keeping the probe tip close enough to the sample for short-range forces to become detectable while preventing the tip from sticking to the surface is a major problem for non-contact dynamic mode in ambient conditions. Dynamic contact mode (also called intermittent contact, AC mode or tapping mode) was developed to bypass this problem. In tapping mode, the cantilever is driven to oscillate near its resonance frequency by a small piezoelectric element mounted in the AFM tip holder similarly to non-contact mode. However, the amplitude of this oscillation is greater than 10 nm. Van der Waals forces, dipole-dipole interactions, electrostatic forces, etc. acting on the cantilever when the tip comes close to the surface cause the amplitude of this oscillation to decrease as the tip gets closer to the sample. An electronic servo uses the piezoelectric actuator to control the height of the cantilever above the sample. The servo adjusts the height to maintain cantilever oscillation amplitude as the cantilever is scanned over the sample. A tapping AFM image is therefore produced by imaging the force of the intermittent contacts of the tip with the sample surface. This method of "tapping" minimizes the damage done to the surface and the tip compared to the amount done in contact mode. Tapping mode is gentle enough even for the visualization of supported lipid bilayers or adsorbed single polymer molecules under liquid medium. With proper scanning parameters, the conformation of single molecules can remain unchanged for hours.

Non-contact mode – In this imaging mode, the tip of the cantilever does not contact the sample surface; it oscillates instead above the adsorbed fluid layer on the surface during scanning at either its resonant frequency (frequency modulation) or just above (amplitude modulation) where the amplitude of oscillation is typically a few nanometers (<10 nm) down to a few picometers. Using a feedback loop to monitor changes in the amplitude due to attractive Van der Waals forces the surface topography can be measured. Advantages of this mode are: very low force exerted on the sample and an extended probe lifetime.

2.2.3 Fluorescence microscopy

Fluorescence microscopy is one of the most widely used approaches for localizing proteins and subcellular compartments at the optical microscopy level. The strategies here described take advantages of the sensitivity and specificity of non immunological as well as immunologically based fluorescent probes for revealing structure-function relationships [33].
Non-immunological fluorescent probes may be used to directly label specific subcellular components and macromolecules. Many of these probes are taken up into living cells and are incorporated and concentrated in specific organelles that can then be examined using the fluorescent microscope.
Immunofluorescence (IF), the most well known application of fluorescent microscopy, involves the use of antibodies to localize a particular protein or antigen. Direct or one-step immunofluorescence involves the conjugation of a fluorophore (i.e. fluorescein isothiocyanate FITC) directly to the primary antibody, thereby making the localization a one-step procedure. Indirect immunofluorescence, which is used more frequently, involves the initial binding of the primary antibody to the antigen in a fixed cell. Subsequently, a fluorescently labeled secondary antibody is incubated with the specimen to form a fluorescent "sandwich" at the site of the target. The secondary antibody is chosen to react with the host species in which primary antibody was raised (i.e. 1st antibody raised in mouse, 2nd antibody X species-anti mouse).

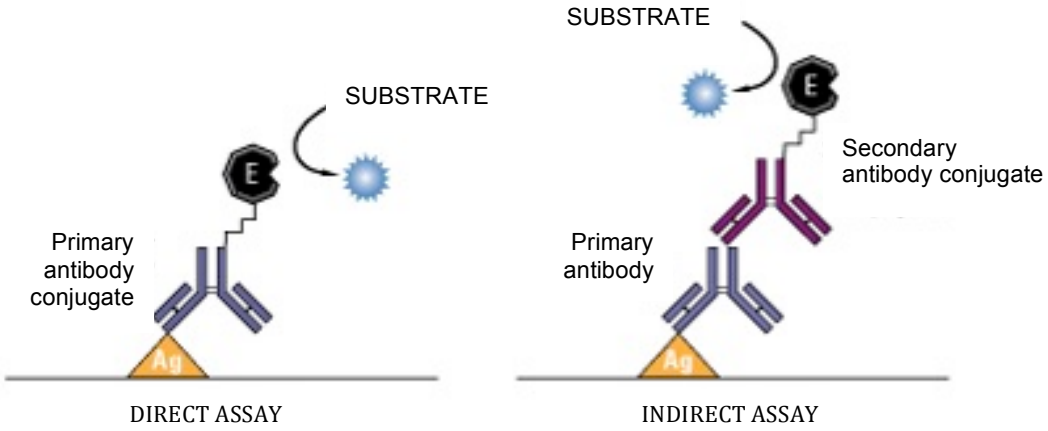

*Figure **2.14**: Direct and indirect immunoassay scheme*

Typically the overall scheme for localization of a cellular protein by indirect immunofluorescence involves:

- Fixation (unless live cells are to be studied)
- Permeabilization to allow penetration of antibodies
- Blocking sites that can promote nonspecific interactions
- Labeling fixed cells/tissues with specific antibodies

- Perform microscopic examination

We have observed both the direct and indirect immunofluorescence. Imaging was performed using a microscope Nikon Eclipse i80.

Immunofluorescence working principles.

Fluorescence is due to the absorption of a photon by a fluorochrome molecule, which excites an electron to a higher energy level, followed by a loss of energy by emission of a longer-wavelength photon after a few nanoseconds. Optical filters can be used to separate the short-wavelength excitation photons from the longer-wavelength emission photons. Specific labeling of an antigen by a fluorochrome-conjugated antibody makes possible the localization of the antigen in the specimen, since only the specific antigen lights up. Fluorescence microscopy is a high-contrast technique because the bright fluorescence stands out in high contrast against the dark background of the specimen. Moreover, fluorescence can easily be quantitated since fluorescence intensity is linearly proportional to the amount of excitation light and the amount of fluorochrome.
The limits to IF include specificity of the antibodies, specimen preparation, autofluorescence and performance of the microscope and user.

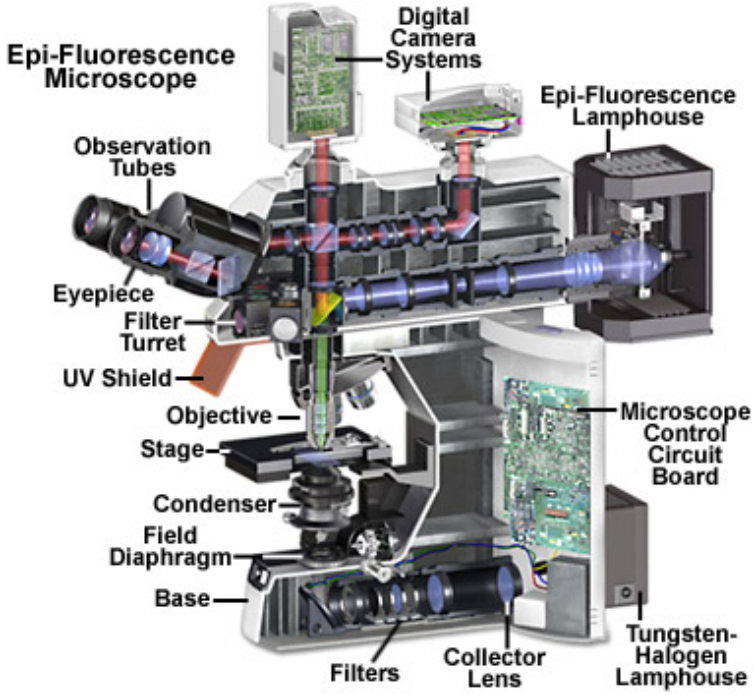

*Figure **2.15**: Schematic representation of Epi-Fluorescence Microscope.*

In the classic fluorescent microscope, light is emitted from a source (i.e. mercury or xenon lamp, in our case Mercury Arc Lamp lamphouse) and specific wavelengths are transmitted through an excitation filter. Specific excitation filters are used to allow the

excitation of specific fluorochromes. Light then reaches the dichromatic (also termed a dichroic) mirror or beam splitter, which reflects short-wavelength light to the specimen, which then emits longer-wavelength light that is transmitted by the beam splitter. The emission filter attenuates all the light transmitted by the excitation filter and very efficiently transmits any fluorescence emitted by the specimen. The light is always of longer wavelength than the excitation color.

Samples Preparation

In this thesis, we used two IF protocols: Actin Cytoskeleton and Focal Adhesion Staining (to investigate the adhesion of cells on the functionalized surfaces) and β-III Tubulin Antibody Staining (to mark the network of neuronal cells differentiated from stem cell condition).

Actin Cytoskeleton and Focal Adhesion Staining

Actin is a major component of all eukaryotic cells and is highly conserved across species. The organization of this protein in cells is highly dynamic. The actin cytoskeleton is a highly dynamic network composed of actin polymers and a large number of associated proteins. The function of the actin cytoskeleton is to mediate essential biological functions in all eukaryotic cells, including intra- and extra-cellular movement and structural support. The organization of the actin cytoskeleton is tightly regulated both temporally and spatially. The actin cytoskeleton is a dynamic structure that rapidly changes shape and organization in response to stimuli and cell cycle progression [34], [35]. Orientational distribution of actin filaments within a cell is therefore an important determinant of cellular shape and motility. Focal adhesion and adherents junctions are membrane-associated complexes that serve as nucleation sites for actin filaments and as cross-linkers between the cell exterior, plasma membrane and actin cytoskeleton [36]. The function of focal adhesions is structural, linking the extracellular matrix outside the cells to the actin cytoskeleton inside. They are also sites of signal transduction, initiating signaling pathways in response to adhesion. Focal adhesions consist of integrin-type receptors that are attached to the extracellular matrix and are intracellularly associated with protein complexes containing vinculin (universal focal adhesion marker), talin, alpha-actinin, paxillin, tensin and focal adhesion kinase [37], [38].
In both the IF protocols, we stained cell nuclei with 4',6-diamidino-2-phenylindole (DAPI) to get a more clear information about the nuclei shape and cell status. DAPI is the most common fluorochrome used for fluorescently labeling double-stranded Dna, via strongly binding to A-T rich regions (it is about 20 times more fluorescent when bound to runs of A-T bases than when free in solution or bound to G-C bases)[39]. It can pass through an intact cell membrane therefore it can be used to stain both living and fixed cells. In the immunofluorescence assays reported here the marked targets were: the focal adhesion proteins using antibodies against vinculin, cytoskeletal elements by the

TRITC-conjugated Phalloidin and nuclei by DAPI. The detailed steps of the protocol are the following:

1. Fix cultured cells with 4% paraformaldehyde in 1X PBS for 15-20 minutes at room temperature.
2. Wash twice with 1X washing buffer.
3. Permeabilize cells with 0.1% Triton X-100 in 1X PBS for 1-5 minutes at room temperature.
4. Wash twice with 1X washing buffer.
5. Apply blocking solution for 30 minutes at room temperature.
6. Dilute primary antibody (Anti-Vinculin) to a working concentration in blocking solution, and incubate for 1 hour at room temperature.
7. Wash three times (5-10 minutes each) with 1X washing buffer.
8. Dilute secondary antibody in 1X PBS just before use and incubate for 30-60 minutes at room temperature. For double labeling TRITC- conjugated Phalloidin can be incubated simultaneously with the secondary antibody for 30-60 minutes at room temperature.
9. Wash three times (5-10 minutes each) with 1X wash buffer.
10. Following this washing step, nuclei counterstaining can be performed by incubating cells with DAPI for 1-5 minutes at room temperature, followed by washing cells three times (5-10 minutes each) with 1X wash buffer.

Fluorescence images can then be visualized with a fluorescence microscope.

β-Tubulin III Antibody Staining

Tubulins are the major components of cellular cytoskeleton; these proteins form microtubules that are critical for cellular structure, migration, cell division, and intracellular trafficking. There are three types of tubulins: alpha, beta, and gamma of approximately 55 kDa of molecular weight. Microtubules are large structures (30 nm in diameter) composed of alternating alpha and beta subunits. Complexes that block microtubule formation, such as Taxol and the vinca alkaloids, inhibit cell division and are efficient anti-cancer agents. Class III β-tubulin is a microtubule element expressed exclusively in neurons, and therefore it can be used as a popular marker specific for this kind of cells. It contributes to microtubule stability in neuronal cell bodies and axons, and plays a role in axonal growth [40][41]. The detailed steps of the staining protocol are:

1. Fix cultured cells with 4% paraformaldehyde in 1X PBS for 15-20 minutes at room temperature.
2. Wash twice with 1X washing buffer.

3. Permeabilize cells with 0.1% Triton X-100 in 1X PBS for 1-5 minutes at room temperature.
4. Wash twice with 1X washing buffer.
5. Apply blocking solution for 30 minutes at room temperature.
6. Dilute primary antibody (Anti-β-Tubulin III) to the working concentration in blocking solution, and incubate for 1 hour at room temperature.
7. Wash three times (5-10 minutes each) with 1X wash buffer.
8. Dilute secondary antibody (Alexa Fluor 594) in 1X PBS just before using and incubate for 30-60 minutes at room temperature.
9. Wash three times (5-10 minutes each) with 1X washing buffer.
10. Following this washing step, nuclei counterstaining can be performed by incubating cells with DAPI for 1-5 minutes at room temperature, followed by washing cells three times (5-10 minutes each) with 1X washing buffer.

Fluorescence images can then be visualized with a fluorescence microscope.

Bibliography

[1] V. Mironov, T. Boland, T. Trusk, G. Forgacs, and R. R. Markwald, "Organ printing: computer-aided jet-based 3D tissue engineering.," *Trends Biotechnol.*, vol. 21, pp. 157–161, 2003.

[2] B. R. Ringeisen, C. M. Othon, J. A. Barron, D. Young, and B. J. Spargo, "Jet-based methods to print living cells," *Biotechnol. J.*, vol. 1, pp. 930–948, 2006.

[3] F. Guillemot, V. Mironov, and M. Nakamura, "Bioprinting is coming of ages," *Biofabrication*, vol. 2, 2010.

[4] J. Bohandy, B. F. Kim, and F. J. Adrian, "Metal deposition from a supported metal film using an excimer laser," *J. Appl. Phys.*, vol. 60, pp. 1538–1539, 1986.

[5] M. Colina, P. Serra, J. Fernández-Pradas, L. Sevilla, J. Morenza, and ., "DNA deposition through laser induced forward transfer," *Biosens. Bioelectron.*, vol. 20, pp. 1638–1642, 2005.

[6] V. Dinca, E. Kasotakis, J. Catherine, A. Mourka, A. Ranella, A. Ovsianikov, B. N. Chichkov, M. Farsari, A. Mitraki, and F. C., "Directed three-dimensional patterning of self-assembled peptide fibrils," *Nano Lett.*, vol. 8, no. 2, pp. 538–543, 2008.

[7] H. Geckil, F. Xu, X. Zhang, S. Moon, and U. Demirci, "Engineering hydrogels as extracellular matrix mimics," *Nanomedicine*, vol. 5, pp. 469–484, 2010.

[8] J. Samot, S. Moon, L. Shao, X. Zhang, F. Xu, Y. Song, H. Keles, L. Matloff, J. Markel, and U. Demirci, "Blood banking in living droplets," *PLoS One*, vol. 6, no. 3, 2011.

[9] B. Derby, "Bioprinting: inkjet printing proteins and hybrid cell-containing materials and structures," *J. Mater. Chem.*, vol. 18, no. 47, p. 5717, 2008.

[10] J. A. Barron, P. Wu, H. D. Ladouceur, and B. R. Ringeisen, "Biological laser printing: a novel technique for creating heterogeneous 3-dimensional cell patterns," *Biomed. Microdevices*, vol. 6, no. 2, pp. 139–147, 2004.

[11] M. Duocastella, M. Colina, J. M. Fernández-Pradas, P. Serra, and J. L. Morenza, "Study of the laser-induced forward transfer of liquids for laser bioprinting," *Appl. Surf. Sci.*, vol. 253, no. 19, pp. 7855–7859, Jul. 2007.

[12] A. Pearson, E. Cox, J. Blake, and S. Otto, "Bubble interactions near a free surface," *Eng. Anal. Bound. Elem.*, vol. 28, pp. 295–313, 2004.

[13] M. Longuet-Higgins, "Bubbles, breaking waves and hyperbolic jets at a free surface," *J. Fluid Mech.*, vol. 127, pp. 103–121, 1983.

[14] M. Duocastella, J. Fernandez-Pradas, P. Serra, and J. L. Morenza, "Jet formation in the laser forward transfer of liquids," *Appl. Phys. A*, vol. 93, pp. 453–456, 2008.

[15] Z. Chengping, L. David, A. M. Scott, G. John, M. S. Timothy, K. G. Barry, M. Rohit, W. Huey-Daw, and B. C. Douglas, "Laser direct write and its application in low temperature Co-fired ceramic (LTCC) technology," *Microelectron. Eng.*, vol. 70, no. 1, pp. 41–49, 2003.

[16] J. A. Barron, H. D. Young, D. D. Dlott, M. M. Darfler, D. B. Krizman, and B. R. Ringeisen, “Printing of protein microarrays via a capillary-free fluid jetting mechanism,” *Proteomics*, vol. 5, no. 16, pp. 4138–4144, 2005.
[17] V. Dinca, M. Farsari, D. Kafetzopoulos, A. Popescu, M. Dinescu, and C. V. Fotakis, “Patterning parameters for biomolecules microar- rays constructed with nanosecond and femtosecond UV lasers,” *Thin Solid Films*, vol. 516, pp. 6504–6511, 2008.
[18] P. Serra, M. Fernández-Pradas, J.M. Colina, M. Duocastella, J. Domínguez, and J. L. Morenza, “Laser-induced forward transfer: a di- rect-writing technique for biosensors preparation,” *J. Laser Micro / Nanoeng.*, vol. 1, no. 3, pp. 236–242, 2006.
[19] A. Vogel, K. Lorenz, V. Horneffer, G. Hüttmann, and D. S. A. Von Gebert, “Mechanisms of Laser-Induced Dissection and Transport of Histologic Specimens,” *Biophys. J.*, vol. 93, no. 12, pp. 4481–4500, 2007.
[20] M. Schena, D. Shalon, R. Davis, and P. Brown, “Quantitative monitoring of gene expression patterns with a comple- mentary DNA microarray,” *Science (80-.).*, vol. 270, pp. 467–470, 1995.
[21] M. Chee, R. Yang, E. Hubbell, A. Berno, X. C. Huang, D. Stern, J. Winkler, D. J. Lockhart, M. S. Morris, and S. P. Fodor, “Accessing genetic information with high-density DNA arrays,” *Science (80-.).*, vol. 274, pp. 610–614, 1996.
[22] R. S. Kane, S. Takayama, E. Ostuni, D. E. Ingber, and G. M. Whitesides, “Patterning proteins and cells using soft lithography,” vol. 20, 1999.
[23] M. Cavallini, D. Gentili, P. Greco, F. Valle, and F. Biscarini, “Micro- and nanopatterning by lithographically controlled wetting.,” *Nat. Protoc.*, vol. 7, no. 9, pp. 1668–76, Sep. 2012.
[24] M. Ventre, F. Valle, M. Bianchi, F. Biscarini, and P. a Netti, “Cell fluidics: producing cellular streams on micropatterned synthetic surfaces.,” *Langmuir*, vol. 28, no. 1, pp. 714–21, Jan. 2012.
[25] A. Ulman, “Formation and Structure of Self-Assembled Monolayers,” 1996.
[26] Z. Cui, *Nanofabrication: principles, capabilities and limits*. 2008.
[27] K. Sun, B. Jiang, and X. Jiang, “Electrochemical desorption of self-assembled monolayers and its applications in surface chemistry and cell biology,” *J. Electroanal. Chem.*, vol. 656, no. 1–2, pp. 223–230, 2011.
[28] T. Kawaguchi, H. Yasuda, K. Shimazu, and M. D. Porter, “Electrochemical quartz crystal microbalance investigation of the reductive desorption of self-assembled monolayers of alkanethiols and mercaptoalkanoic acids on Au,” *Langmuir*, vol. 16, pp. 9830–9840, 2000.
[29] J. Liang, M. Castronovo, and G. Scoles, “DNA as invisible ink for AFM nanolithography,” *J. Am. Chem. Soc.*, vol. 134, pp. 39–42, 2012.
[30] M. Liu, N. A. Amro, and G. Liu, “Nanografting for Surface Physical Chemistry,” *Annu. Rev. Phys. Chem.*, vol. 59, pp. 367–386, 2008.
[31] M. A. Hayat, *FIxation for electron microscopy*. 1981.

[32] A. L. Cohen, “Critical point drying - principles and procedures.,” *Scanning Electron Microsc. Inc., AMF O’Hare*, pp. 303–324, 1979.
[33] D. L. Spector and R. D. Goldman, *Basic Methods in Microscopy. Protocols and Concepts from Cells: A Laboratory Manual*. CSHL Press, 2006.
[34] R. R. Dubreuil, “Structure and Evolution of the Actin Cross-Linking Proteins,” *Bioessays*, vol. 13, pp. 219–226, 1991.
[35] P. Matsudaira, “Modular Organization of Actin Cross-Linking Proteins.,” *Trends Biochem. Sci.*, vol. 16, pp. 87–92, 1991.
[36] K. M. Yamada and B. Geiger, “Molecular interactions in cell adhesion complexes,” *Curr. Opin. Cell Biol.*, vol. 9, pp. 76–85, 1997.
[37] C. E. Turner and K. Burridge, “Transmembrane molecular assemblies in cell-extracellular matrix interactions,” *Curr. Opin. Cell Biol.*, vol. 3, pp. 849–853, 1991.
[38] K. Burridge, G. Nuckolls, C. Otey, F. Pavalko, K. Simon, and C. Turner, “Actin-membrane interaction in focal adhesions,” *Cell Cell Differ. Dev.*, vol. 32, no. 3, pp. 337–342, 1990.
[39] J. Kapuscinski, “DAPI: a Dna-specific fluorescent probe,” *Biotech. Histochem.*, vol. 70, no. 5, pp. 220–233, 1995.
[40] Y. Q. Jiang and M. M. Oblinger, “Differential regulation of beta III and other tubulin genes during peripheral and central neuron development,” *J. Cell Sci.*, vol. 103, pp. 643–651, 1992.
[41] K. H. Downing and E. Nogales, “Tubulin and microtubule structure,” *Curr. Opin. Cell Biol.*, vol. 10, pp. 16–22, 1998.

Chapter 3

In this chapter two applications of Laser Assisted Bioprinting for the patterning of Laminin as a cell adhesion cue are reported: the first one is suitable for neurites guiding during neural stem cell differentiation on biodegradable PLGA films; the second one for modulating cell adhesion according to droplets distance with the support of a mathematical simulation model.

Laser Assisted Bioprinting of Laminin on biodegradable PLGA substrates for stem cell adhesion and differentiation

Patterning cell-adhesive molecules on surfaces is widely used for promoting cell growth and controlling their position on different materials, including anti-fouling ones. Attempts to fabricate nano and microscopic features useful for neuronal cell guidance have been reported [1].

Polymeric materials such as poly(esters), poly(glycolic acid) (PGA), poly(lactic acid) (PLA), poly(lactic-co-glycolic acid) (PLGA) [2], are widely preferred as scaffolds for peripheral and central nerve regeneration because of their availability, ease of processing, biodegradation characteristics, and approval by the FDA.

Adhesion proteins, growth factors and in general protein signals govern the nerve regeneration process [3]. Usually these chemical cues induce plasticity in endogenous cells, which are in the proximity of the injury and stimulate the differentiation of stem cells recruited from different sites. However delivery and control of the concentration of these proteins around the site of the lesion represent a difficult task, due also to other biochemical events occurring, such as for instance the foreign body reaction to the biodegradable scaffold.

Several extracellular matrix (ECM) proteins have been studied as functional elements for patterning biodegradable scaffolds, including fibronectin, collagen, polylisine and laminin. Laminin is a large glycoprotein (approximately 900 kDa), formed by a complex of three units, with a shape that resembles a flexible cross. It is largely present on the basal lamina of stem cells and interacts with stem cells integrins, favoring neurite growth, repair and remyelination [4]. Owing to its large size, it is difficult to obtain high surface densities of it, displaying the correct orientations for ligand-receptor interaction. Different functionalization protocols propose that γ-chains monomers of laminin may also be successful in mimicking ECM, with larger surface densities of patterning and improved binding to the surface.

In vitro studies have shown that patterning may exert a guidance effect on the adhesion of cells and growth of neurites and axons [5]. Structuring the surface topography of the

scaffold with arrays of parallel lines is widely used to orient the direction of the neurites growing in restricted environment [5]. The characteristic periodicity of the channels or grooves influences the growth of neurites along or perpendicular to the structure direction [6]. However the topographical modulation is not sufficient per se to ensure a stable adhesion and the chemical cues appear to be necessary for specific cell types.

As reported in Chapter 2, Laser Assisted Bioprinting (LAB) is an emerging technology for patterning biomolecules and functional materials on substrates and devices. In this chapter we report the patterning of laminin arrays on biodegradable polimeric films of PLGA poly(lactic-co-glycolic acid) by Laser Assisted Bioprinting for promoting, regulating and guiding stem cell adhesion and neural differentiation.

3.1 Laminin functionalization of PLGA film

PLGA film has been obtained by solution casting method as reported in "Materials and Methods" The functionalization of these thin films with Laminin is done by means of LAB technique.
The laser beam power has been tuned to achieve the formation of a single drop as output of the unstable fluid microjet of LAB. The dynamics of the process implies that the solution delivered is subject to high shear stress during the jet formation, however heat transferred to the Bioink during patterning is limited. The LAB microjet deposits the laminin droplets upon the biodegradable scaffold (PLGA) which does not immediately absorb the excess of water-glycerol solution, therefore the laminin solution remains in incubation upon the surface for a defined period of time, before the complete evaporation of glycerol-water component. Due to high surface tension of glycerol, the evaporation of the 0.1 pL droplets occurs within 24 hours from the instant of deposition. Laminin has been detected by immunofluorescence assay as described in Materials and Methods paragraph (Figure **3.1**).

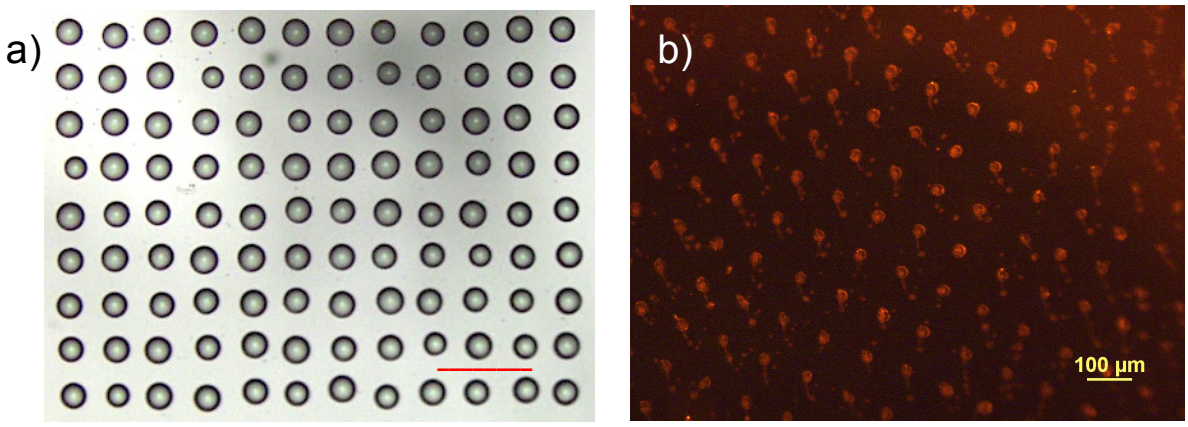

*Figure **3.1**: (a) optical microscopy image of a droplets array of Laminin just few minutes after bioprinting deposition on PLGA film. Scale bar is 100 µm. (b) Positive immunofluorescence assay for Laminin on PLGA.*

The laminin trimers dispersed in the droplet diffuse and adsorb onto the surface following a trend that may be interpreted with Lang and Coates theory [7], for initial concentration below 15 µg/ml. According to the proposed mechanism, the adsorption of biomolecules is effectively controlled just by the diffusion coefficient of laminin, in literature reported to be 1.1×10^{-9} m^2/s [8]. The surface coverage and the morphology of the protein thin film may be controlled changing the time of incubation or the concentration of the protein within the Bioink film. To verify the fabrication of a stable surface pattern on biodegradable PLGA, we performed LAB of several arrays of droplets, starting from different initial concentrations of laminin (15, 25, 50 µg/ml) and incubating the substrates for 30, 60, 120 and 240 minutes before rinsing with PBS buffer to remove the unbound protein. The resulting adsorbed pattern has been characterized by atomic force microscopy. The estimated volume of a single droplet of LAB is 0.1 pL, therefore, for an array of 100 droplets, the amount of protein in solution, at the instant of deposition, is approximately 0.2 pg, when starting from a solution of 15 µg/ml.
The size of the spots of laminin after incubation does not depend on the concentration of the protein in the starting solution. The microdroplet delivered by bioprinting is deposited on the substrate, but the controlled environmental conditions ensure that the process of evaporation of the solvent is slowed down to more than 24 hours, also thanks to the presence of glycerol. Laminin adsorbs on the substrate within the footprint of microdroplet, and the initial concentration reduces the amount of protein available per unit area. This is evident from the AFM images shown in Figure 3.2.

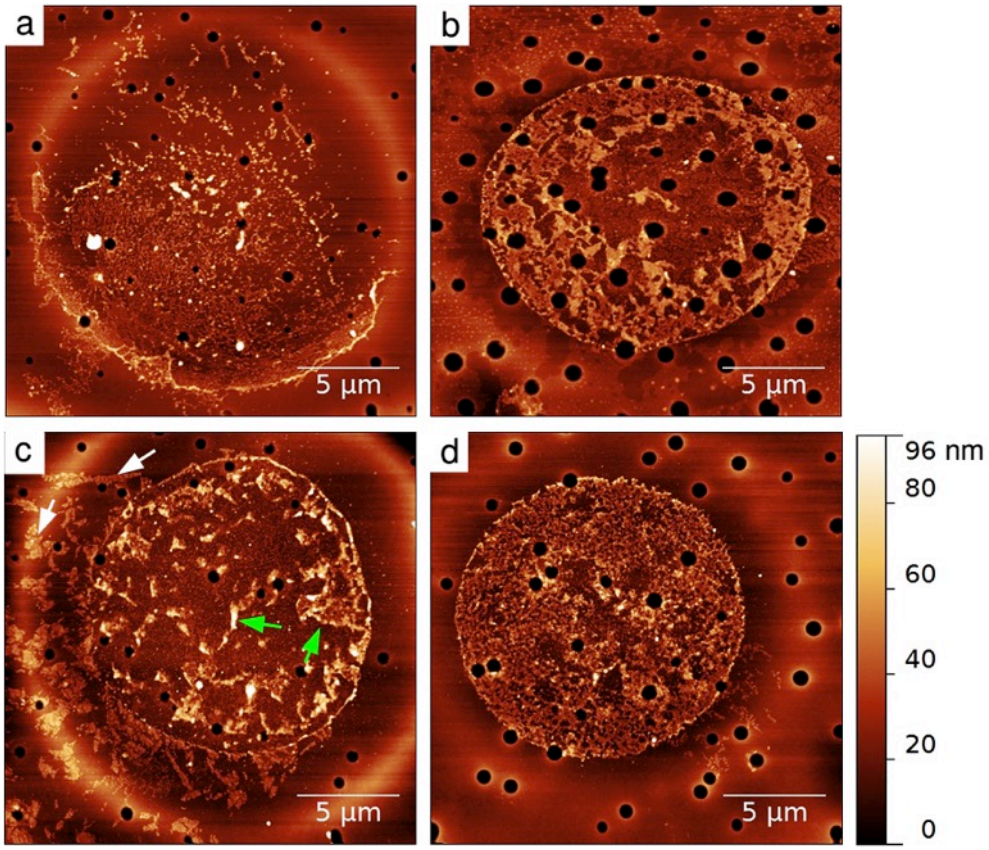

*Figure **3.2**: Laser Assisted Bioprinting of laminin on PLGA scaffold. AFM images taken at different incubation times: (a) 30 minutes, (b) 60 minutes, (c) 120 minutes, (d) 240 minutes. The white arrows indicate the protein aggregates weakly bound and displaced by the washing step. The green arrows show the beginning of a second layer of adsorbed protein.*

After 30 minutes of incubation, there is the formation of a partial monolayer of laminin, which does not entirely cover the area of the droplet. It is clear that at low concentration and incubation times the patterned areas are subject to a greater statistical variability.
After 60 minutes of incubation, the evolution of the deposition process appears to resemble Random Sequential Adsorption (RSA) [9], for which it is already noticeable the formation of 3D clusters on the surface. These aggregates have an approximate thickness of 40 nm. At 120 minutes of incubation the coverage reaches saturation in the area occupied by the microdrop and appears more clearly the presence of these aggregates weakly bound to the surface. In fact the washing operations may result in the partial displacement of these aggregates outside of the footprint of the microdrop. The random sequential adsorption modeling is suggested by the increase of the amount of protein with incubation time, in accordance with the trend line shown in Figure 3.3.

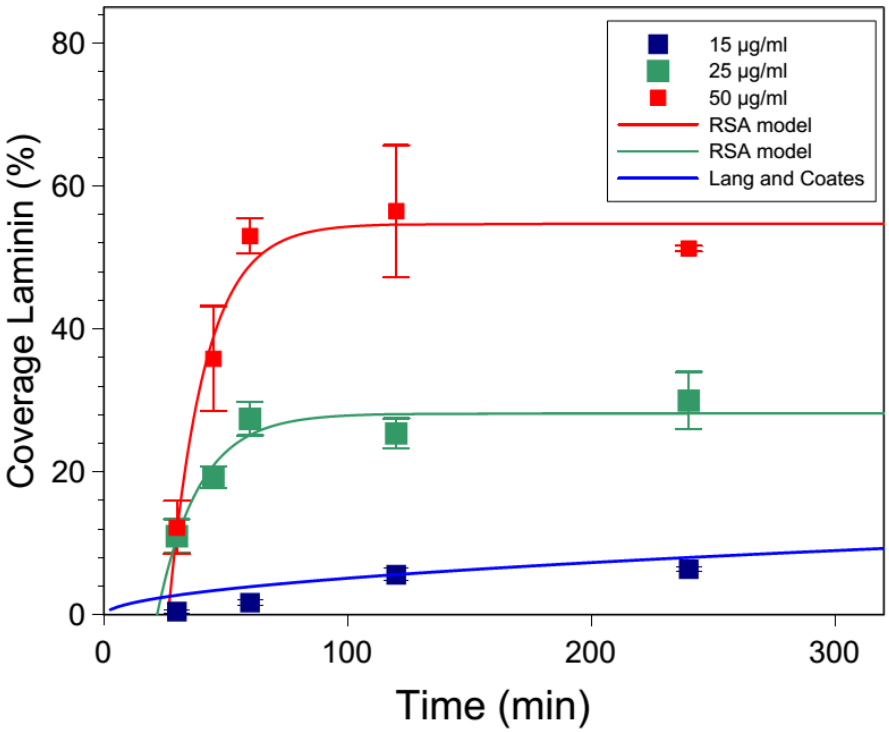

*Figure **3.3**: Laminin coverage, within the droplet footprint, obtained after threshold analysis of AFM images, for different initial concentration and incubation times. Continuous lines are fitting with Lang and Coates diffusion controlled theory for concentration of starting protein lower than 15 µg/ml, whereas for higher concentration Random Sequential Adsorption model provides a correct approximation of the experimental results.*

At 240 minutes, the footprint of the microdroplet is completely saturated with laminin, but the amount of protein available is not substantially different from what it was found for 120 minutes of incubation, according to AFM coverage results. The root mean squared (rms) roughness (Rrms) measured on the pattern of laminin, at 120 minutes, is 11 nm, increasing by 10% the roughness of the pristine PLGA thin film (Rrms= 10nm). Therefore the laminin patterns performed by LAB do not change significantly the overall roughness of the PLGA scaffold.

It is important to say that the "bioprinted" droplet contains less than 0.05 pL of water, and the hydrolitic degradation of PLGA is almost negligible compared to dimensions of the scaffold employed in the experiment. From the AFM and SEM images a smooth concavity surrounding the laminin pattern can be spotted.

The analysis of surface topography confirms the absence of any degradation for LAB patterns compared to surface roughening occurring during hydration of the PLGA film in contact with a large volume of PBS buffer (see Figure 3.4). Surface waviness, in this case, exhibits a characteristic length around 20 µm and conveys to PLGA peculiar topographic features that exert a guidance effect on adhering cells.

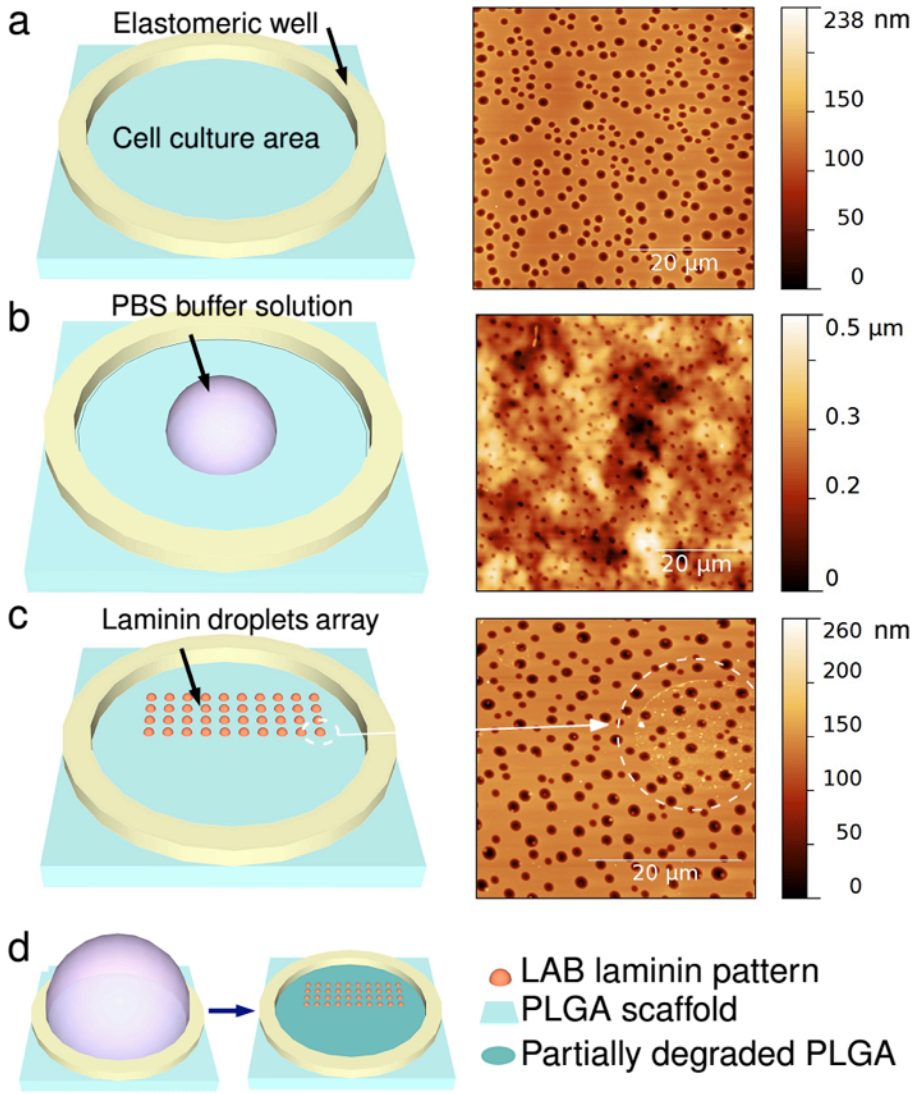

*Figure **3.4**: Fabrication process of topographical and chemical cues upon biodegradable PLGA scaffold. (a) The PLGA thin slab is placed in contact with elastomeric well to confine the cell culture area. Pristine PLGA has a characteristic smooth morphology, with even distribution of pores. (b) After incubation with PBS buffer 0.1x (24h, 37 C), the surface of PLGA undergoes a partial degradation, leading to an increase of surface roughness larger than 60 nm, on 50 µm² window of analysis. (c) Upon the PLGA surface, a regular array of laminin droplets was patterned by LAB, so that the protein adsorbs on the surface, with modest topographical variation (d) Samples for differentiation experiment. Configuration of the scaffold where chemical cues are patterned on top of partially degraded PLGA.*

3.2 Adhesion of NE4C cells

To detect the effect of combined topographical and chemical cues, we investigated the adhesion of NE4C cultured on PLGA (as cast, Figure 3.4c) scaffolds patterned with LAB. Immunofluorescence against adhesion proteins (Vinculin and Phalloidin) and nucleus (DAPI) revealed the presence and the positioning of neural stem cells, with respect to the PLGA scaffold and LAB array of laminin. The adhesion of NE-4C on the functional scaffold is homogeneous on the first 5 hours after seeding. The shape of the cells was controlled with optical microscopy and confirmed the viability of proliferating cells on top of the hydrophobic PLGA film.
After 24 hours, the number of adhered cells diminished sensibly in the area of the PLGA scaffold which was not functionalized with LAB and eventually a large percentage detached from the substrates. Besides, the shape of neural stem cells firmly attached to the functionalized PLGA is consistent with the picture of a proliferating culture (see Figure 3.5).

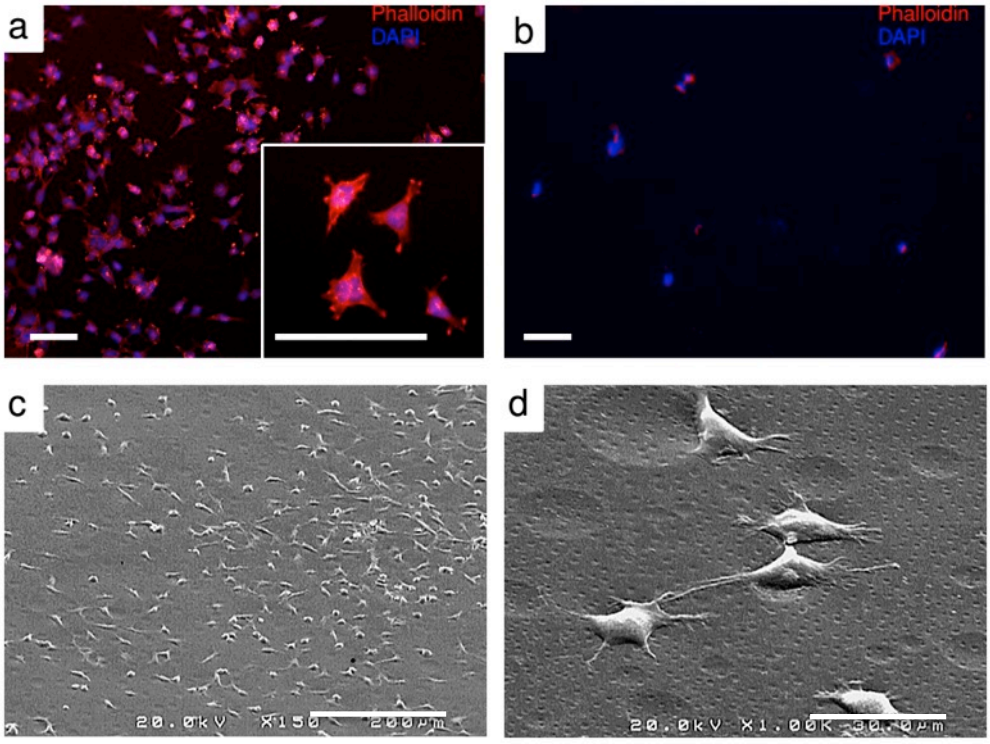

*Figure **3.5**: Adhesion of NE-4C cells on pattern of laminin spots obtained with Laser Assisted Bioprinting. (a) Immunofluorescence of focal contacts (Phalloidin in red, merged with DAPI staining for the nuclei) after 24h from seeding. The focal contacts are found mainly at the edges of cells soma. Scale bars are 100 μm. (b) Immunofluorescence of focal contacts of cells seeded on PLGA scaffold (as cast, not degraded), showing a compromised activity after 24h. (c) SEM image of stem cells adhering on PLGA scaffold isotropically*

patterned with laminin spots. Scale bar is 200 μm. (d) SEM image of stem cells following the concavities left by evaporation of glycerol from LAB droplets. Scale bar is 30 μm.

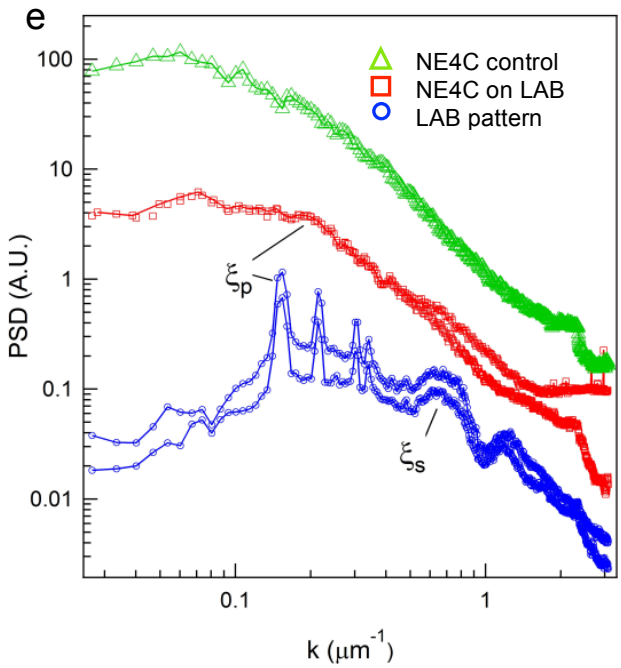

In e) the comparison of power spectrum density of the images taken after deposition of laminin droplets and after immunostaining of focal contacts is shown. The correlation length pointed with ξp accounts for periodicity characteristic of the droplet array, whereas the correlation length termed ξs is due to the statistic diameter of the droplets. The correlation length ξp can be appreciated also on the PSD of the focal contacts, extracted from thresholding of fluorescence image.

The soma is extended upon the smooth scaffold and the processes start to develop towards the spots of laminin, deposited by Laser Assisted Bioprinting. From the SEM images, taken after 24 hours of culture, it is possible to see the shallow concavity, left by the evaporation of the glycerol-water mixture. The ridge of the concavity seems to attract particularly the stem cells, and it may be considered a slight topographic feature effect.

To confirm that neural stem cells are attracted just by the chemical cues, we performed the experiment with PLGA thin scaffold, functionalized with laminin droplets, on a half of the culture plate, leaving the other half surface free from any kind of functionalization. The videomicroscopy coaxial with the laser beam allowed for precise alignment of droplets on the substrate, with large reproducibility. The patterning process guarantees that the surface of the substrate is preserved from contact with any solution other than the laminin one, therefore the PLGA does not undergo hydration or degradation during the functionalization steps. After the evaporation of glycerol, the substrates were put in culture with NE4C and monitored at defined time intervals. The cells attached most promptly on the area containing the laminin droplets, and almost none on the bare PLGA surface (see Figure 3.5b). These results confirm that the bare flat surface of PLGA,

hydrophobic with pores, is not a favorable substrate and cells detach after few days. The laminin deposited by LAB, instead, permit a stable adhesion to the majority of neural stem cells population.

3.3 Control and modulation of NE4C adhesion: cell adhesion mathematic model

Since we can adjust Laminin droplets' distance, we explored NE4C adhesion when protein droplets were spaced at 40, 70 and 100 μm (Figure 3.6).

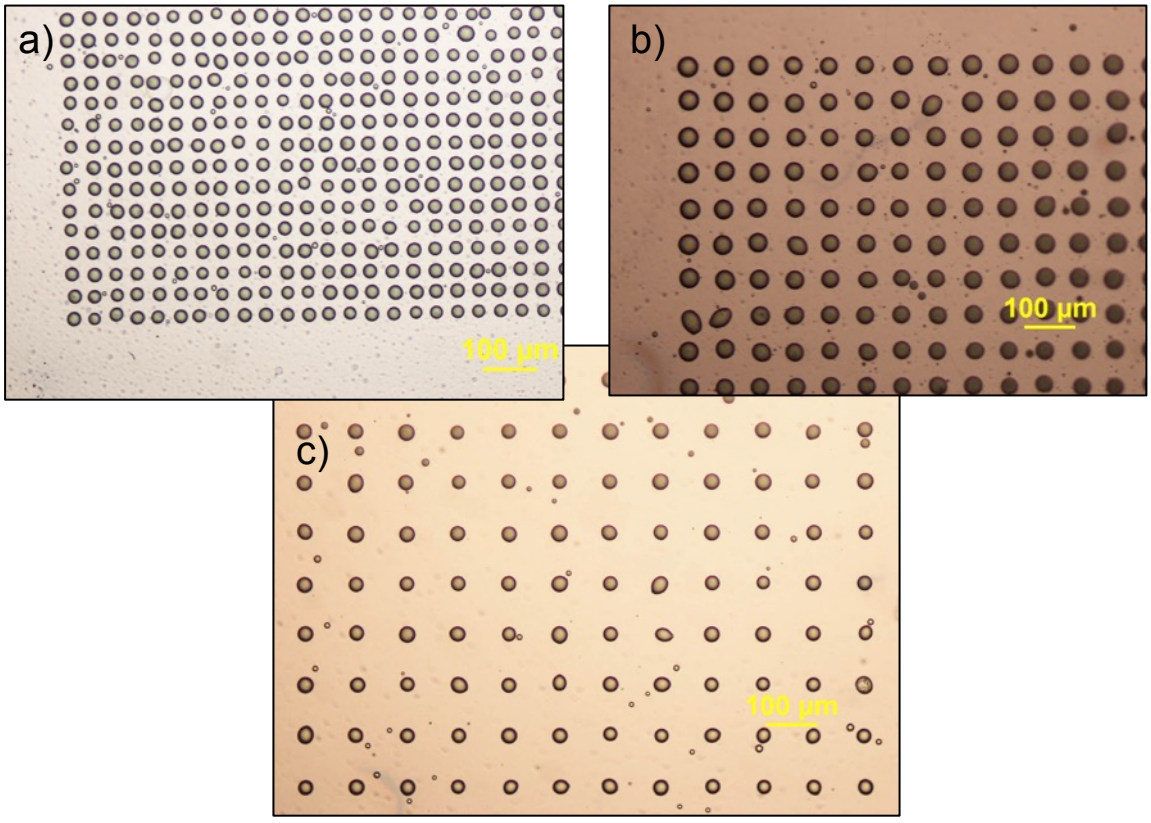

*Figure **3.6**: Optical microscopy (10X, bright field) of Laminin droplets arrays after deposition by Laser Assisted Bioprinting. Droplets are spaced 40 (a), 70 (b) e 100* μm *(c) apart.*

A mathematic model for cell-adhesion formulated by the group of prof. Zerbetto from Chemistry Department G. Ciamician, from University of Bologna, has supported this study.
A soft matter cell model was developed to improve the understanding and control of the interface between biological cells and material surfaces. Cells are modeled as soft matter

drop-like aggregates. This approach is mostly suited to describe stem cells. The stem cells cytoskeleton is less developed than that of other cells and its cytoplasm region consists mostly of liquid. Stem cells are expected to be much softer with respect to other cells (e.g. endothelial, erythrocytes) [10]. The proposed model is based on the mesoscopic particle-based method called Dissipative Particle Dynamics (DPD), initially invented by Hoogerbrugge and Koelman [11] for simulating the dynamic and rheological properties of simple and complex fluids.

DPD is an off-lattice mesoscopic simulation technique, which involves a set of particles moving in continuous space and discrete time. DPD particles may represent portions of molecules, whole molecules or fluid regions, rather than single atoms as in MM (molecular mechanics) or MD (molecular dynamics) methods, and atomistic details are not considered relevant to the addressed processes. The particles' internal degrees of freedom are integrated out and replaced by simplified pairwise dissipative and random forces, so as to conserve momentum locally and ensure correct hydrodynamic behaviour. The main advantage of this method is that it gives access to longer time and length scales than are possible using conventional MD simulations.

Cells are treated as soft matter aggregates described by a collection of DPD beads immersed in a liquid medium. A single cell is placed on a planar solid surface occupying the bottom section of the simulation box. The surface beads are arranged in a face-centred cubic structure kept frozen during the simulation. The simulation setup is depicted in Figure 3.7. Computations are performed for cells of 30 μm diameter.

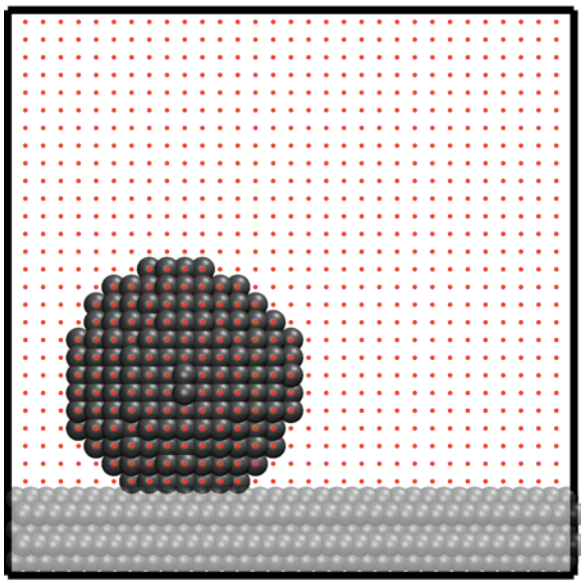

*Figure **3.7**: Initial configuration of the model. The cell (dark grey beads) is located on top of a planar solid surface (light grey beads) in the presence of a surrounding medium (red points).*

The degree of adhesion of a biological cell onto a solid surface can be simulated by opportunely tuning the interaction parameter a_{ij} (adhesiveness) between cell/medium,

cell/substrate and medium/substrate beads. The adhesiveness of the cell is measured by the spreading of the cell soft beads onto the surface. A quantitative measure of the spreading is given by the contact angle, θ_C. The cell/surface contact angle θ_C is determined as proposed by Spenley et al. [12] by fitting a spherical segment to the simulated shape.
A quantitative description of the cell shape is provided by the dimensionless parameter SP:

$$SP = R_1/R_2$$

where R_1 is defined as the mean radius of the slice closest to the surface, while R_2 stands for the mean radius of the slice crossing the midpoint of cell height. For a perfect sphere, SP approaches zero. For non-adhering L1210 leukaemia cells the SP parameter has been estimated to range between 0.2 and 0.6. For adhering cells SP is reported to be in-between 0.8 and 1.5 [13].
It has been demonstrated that patterning cell-adhesive molecules on material surfaces provides a powerful tool for controlling cell adhesion [14].

This model has been used for estimating the probability of cell adhesion (P_A) onto a chemically patterned surface as a function of the pattern geometry (see Figure 3.8).

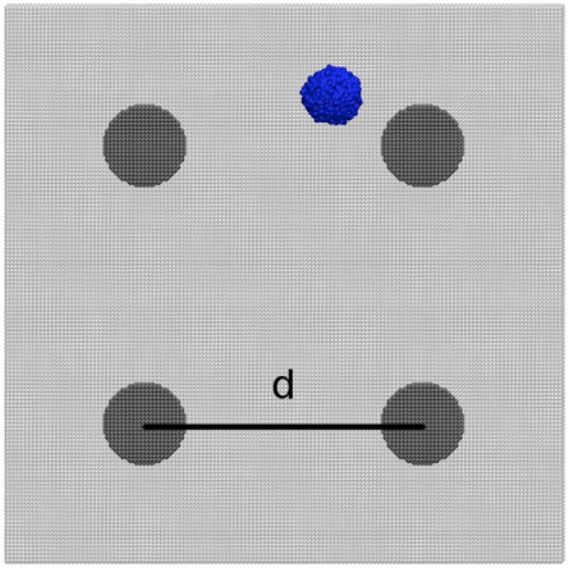

*Figure **3.8**: Model setup for DPD simulations of cell adhesion onto chemically patterned surfaces. Blue beads represent the cells, PLGA surface is depicted in light grey and 20* μm *diameter laminin droplets in dark grey. **d** is the pattern parameter which represents the distance between laminin droplets.*

The PLGA surface has been created by freezing the motion of DPD particles in a crystalline configuration (grey particles in Figure 3.8). Laminin droplets of 20 μm

diameter, which are experimentally patterned on the surface by LAB technique, are created by modifying beads types on the surface (dark grey particles in Figure 3.8).
The adhesion probability (P_A) of a 15 μm size cell has been studied as a function of the pattern size, *d*, expressed as the distance between the centres of laminin droplets. In particular, droplet distances of 40, 70, 100 μm were considered.
The probability of adhesion of a single cell was estimated by running 100 statistically independent simulations with the following procedure:
1) initially the cell is randomly placed on the surface;
2) a short DPD simulation is carried out in order to equilibrate the structure;
3) in the short time interval (comparable with the lifetime of the cell), the cell can moves on the surface by diffusion;
4) if the cell eventually reaches a laminin droplets, which has a favourable interaction with cell beads, it spreads on it and it can be considered attached on the surface. If not, the cell does not adhere and eventually can die.
5) the probability of adhesion is calculated as a function of pattern geometry by averaging the results of the N simulations (see Table 1).

d (μm)	***P_A***
40	99 %
70	46 %
100	21 %

*Table **1**: Probability of adhesion (P_A) as a function of pattern geometry (d).*

From a statistical point of view we interpreted the cells seeded on PLGA functionalized with LAB droplets as a point pattern (obviously the points are given by the position i.e. the coordinates of the cells and the droplets). A statistical tool to characterize the spatial correlation between the marks of a point pattern with discrete marks is the *mark connection function* (MCF) $p_{ij}(r)$, which represents the conditional probability to find two points of type i and j at positions separated by a distance r, under the condition that at these positions there is the geometric center of the cell nucleus or the geometric center of the laminin droplet [15].
The idea is simple: for two points i and j, the MCF gives the probability that the first is of type i and the second of type j. If the patterns contains only type i and j points, the sum of the four possible mark connection functions equals one, that is

$$p_{ii}(r) + p_{ji}(r) + p_{ij}(r) + p_{jj}(r) = 1$$

If the process distributes the marks randomly over the points, the MCFs yield

$$p_{ij}(r) = p_i\, p_j$$

where p_i and p_j are the proportions of type i and j points in the pattern, respectively. However, if the process that distributed the mark i (e.g. cells on PLGA) is positively auto correlated at some distance r (e.g. cells at distance r from have a higher probability of being on LAB droplets), the MCF $p_{ij}(r)$ yields $p_{ii}(r) > p_i p_i$ and it will be above the simulation describing the random point pattern, with uncorrelated marks

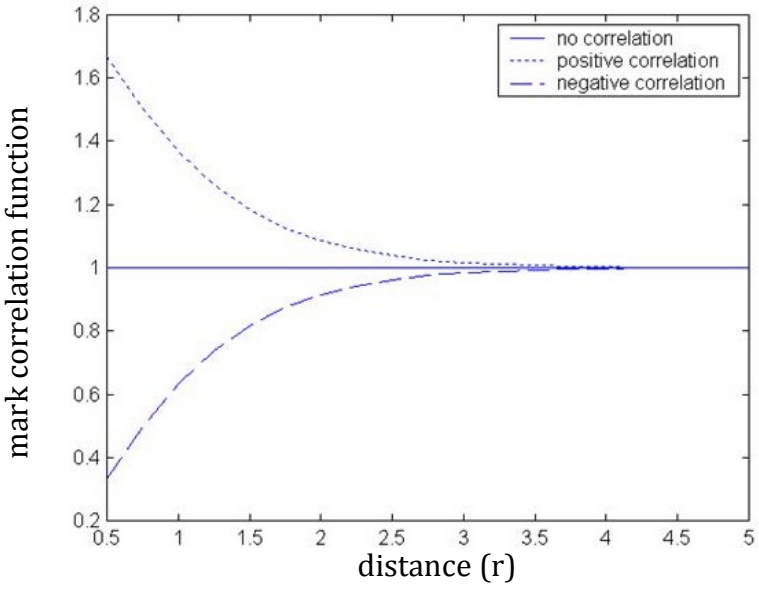

*Figure **3.9:** Mark correlation function indicating positive correlation (dotted line), negative correlation (dashed line) and independence (solid line); respectively, the positive correlation means $p_{ij}(r)>1$, the negative $p_{ij}(r)<1$ and finally, if the marks are uncorrelated, we obtain $p_{ij}(r)=1$.*

Mark connection functions are closely related to pair-correlation functions **g(r)** (that describes how particles distance changes as a function of a sample particle position) and product densities, as follows: if we consider two disjoint disks of infinitesimally small size dx_i and dx_j, centered on locations x_i and x_j, respectively, then the quantity $p_{ij}(r)$ $\mathbf{dx_i}$ $\mathbf{dx_j}$ approximates the probability that a type i point occurs within the first disk and a type j occurs within the second disk. Additionally, we can introduce a quantity $p_{i+j,\ j+i}$ (r) $\mathbf{dx_i}$ $\mathbf{dx_j}$ (where the subscript i+j indicates the combined pattern of type i and type j points), which approximates the probability that a type i or a type j point occurs within the first disk and a type i or a type j occurs within the second disk. Thus the quantity $p_{ij}(r)$ / $p_{i+j,\ j+i}(r)$ yields the probability that the first point is of type i and the second of type j.

Pair correlation function (or radial distribution function) says that for two positions **x** and **y** separated by a distance **r**, the probability **p(r)** of finding a point type i localized in x and a point type j localized in y is

$$p(r) = \lambda_i \times \lambda_j \times g_{ij}(r) d_x d_y$$

where λ_i and λ_j are intensities of i and j points. If i and j are independent to each other, then $g_{ij}(r)=1$. Pair correlation function is generally used for studying and describing quantitatively the internal structure of fluids [16] and quantifies how the particle of interest is surrounded by other particles.

The statistical analysis has been performed on tilted SEM images (see Figure 3.10 underneath) for enhancing cell contrast; obviously the representative distances are subject to these plane transformations.

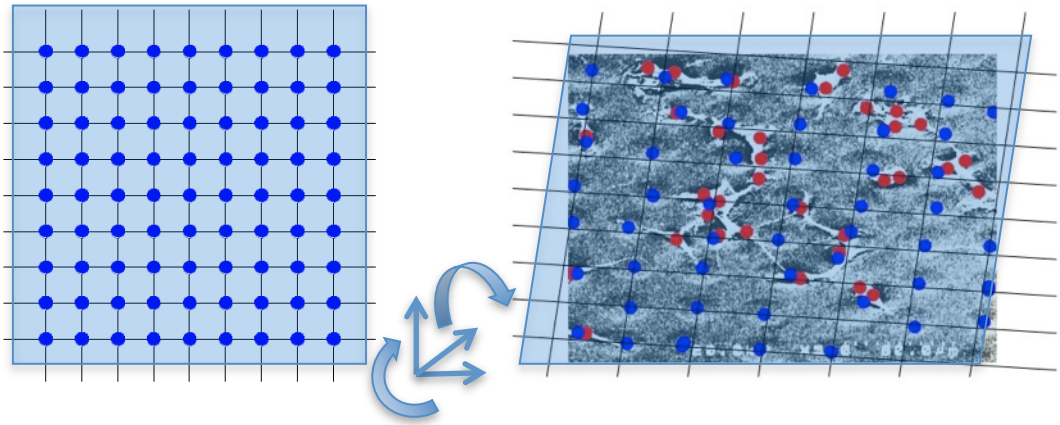

*Figure **3.10**: On the left image we have the Laminin droplets pattern scheme, on the right image, the SEM picture projection.*

The position identification of droplets (blue disks) and cells (red disks) is manually made, coordinates are extracted and a matrix with each point of the two types is generated. Spatial correlation between LAB droplets and cells is made using *spatstat* functions of the statistical analysis software **R**.

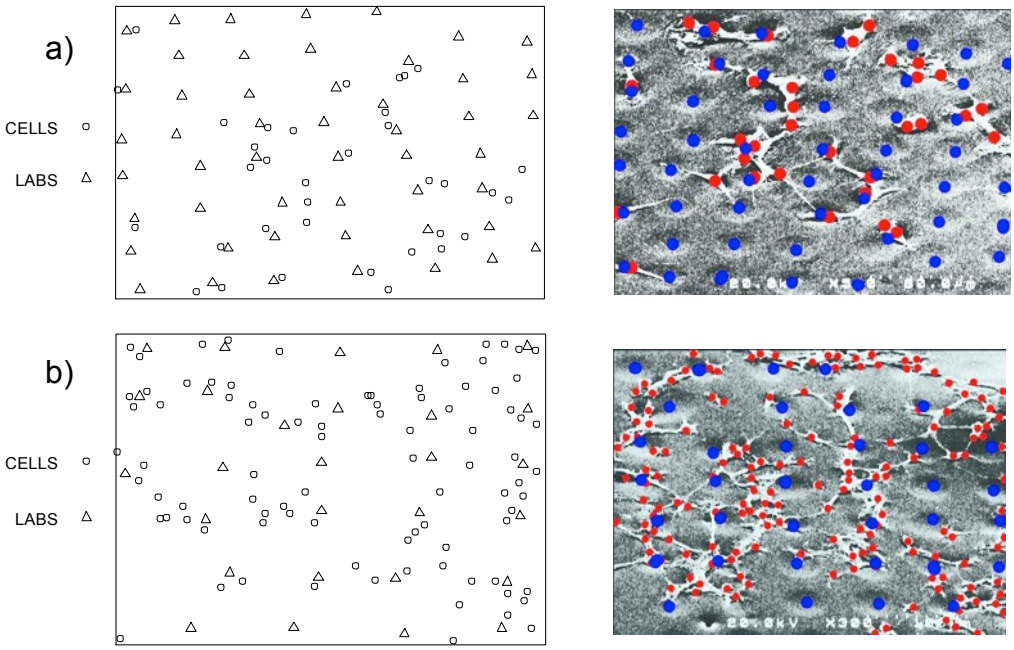

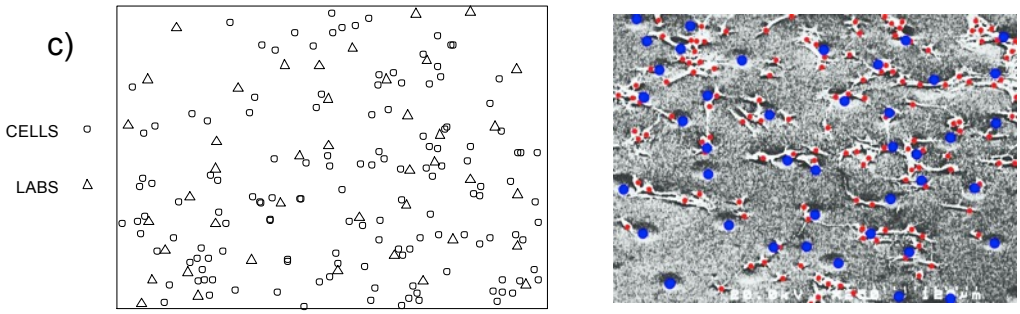

*Figure **3.11**: Extrapolated coordinates on x-axis for cells on droplets spaced a) 40 (a), 70 (b) e 100 μm (c) apart referred to the SEM image on right.*

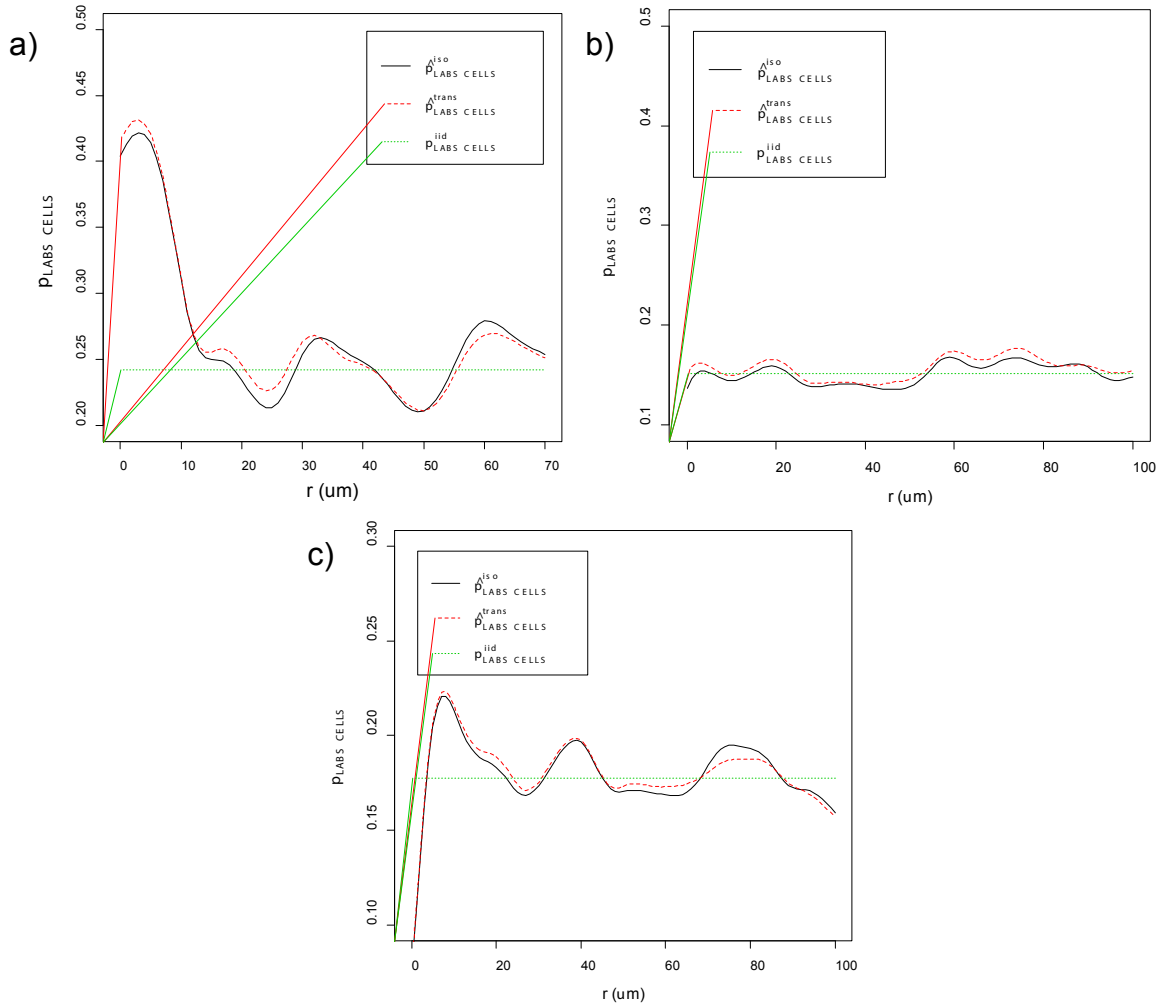

*Figure **3.12**: Mark connection function analysis for correlating lab droplets and cells on 40 (a), 70 (b) e 100 μm (c) samples. It appears that a positive correlation between cells and LAB pattern is more probable for the 40 μm periodicity (peak evident for small r values), whereas for 70 and 100 μm, the probability is not effectively distant from the random spatial distribution hypothesis (dashed dotted horizontal line).*

From the MCF analysis we can say that droplets at 40 μm of distance (r) have higher probability to induce controlled adhesion of NE4C cells in correspondence to the

pattern. For 70 and 100 μm samples, cells adhere following the characteristic adhesion pattern, but the matching seems to get smaller.
Looking at the graph in Figure 3.13 we can see the probabilities evaluated on the samples characterized with SEM.

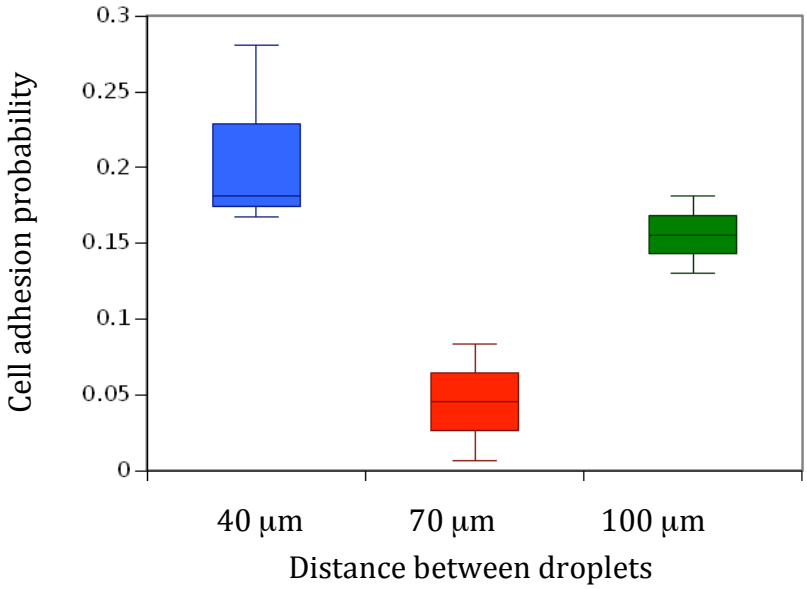

*Figure **3.13**: Cell adhesion probability for each kind of sample. As we can easily see, the trend is not linear and cells are susceptible more to 100 μm droplets distance than 70 μm droplets distance.*

3.4 Differentiation of NE4C cells

To investigate the competitive effect of morphological and chemical cues on differentiation of neural stem cells, PLGA substrates were prepared and incubated with 0.1x PBS buffer solution, in order to achieve a partial modification of surface morphology (see Figure 3.4b). The AFM images return a rough surface morphology (Rrms 60 nm) with the superimposed textures of small pores, characteristic of pristine PLGA.
The PLGA slabs with topographical cues were afterwards patterned with laminin droplets by LAB, producing an array of 1 x 4 mm, aligned on the middle of the cell culture area. In this manner, the neural stem cells felt either the topographical or the topographical and chemical cues on the substrates. As demonstrated in previous section, the LAB technique does not induce change in the morphology but simply the adsorption of thin film of laminin.
NE4C cultures were seeded in DMEM medium upon the PLGA scaffold. After a couple of days upon RA addition, the stem cells differentiated and started forming the initial connections that later developed into neural networks. The cell cultures were cross-

linked after eight days and marked fluorescently for β-Tubulin III, to characterize the direction of neural processes.
The cells differentiated on the full substrate independently on the presence of the laminin chemical cue. This is a clear indication that topographical stimuli are sufficient for differentiation. It is known, in fact, that during differentiation the NE4C stem cells start to synthetize laminin directly, and therefore the role of chemical cue patterned substrates is diminished.
Upon the area functionalized with laminin spots, there is no evidence of an altered cell shape or density, but the neurites protruding from the cell aggregates are mostly oriented along the long axis of the LAB pattern (see Figure 3.14 and Figure 3.15).

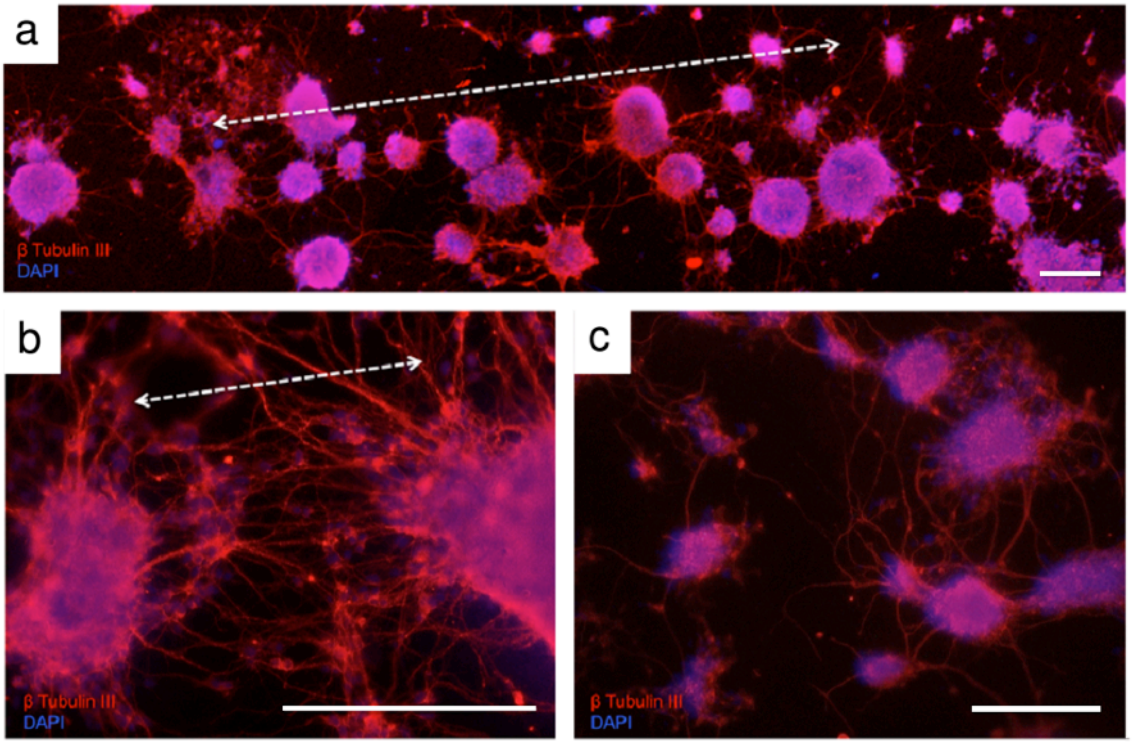

*Figure **3.14**: Differentiation of* NE4C *upon biodegradable PLGA scaffold, with topographical and chemical cues. (a) Immunofluorescence staining after 8 days from seeding. The configuration of the samples sees the superimposition of laminin droplets on a partially degraded PLGA scaffold (see fig. 3.4d). Dotted lines indicate the direction of the LAB pattern under neural clusters. (b) Detailed view of the neural processes, where a slight anisotropy may be appreciated in correlation with the droplets array. (c) View of control sample, where the neurites are extending almost isotropically from cell clusters. Scale bars are 100 μm.*

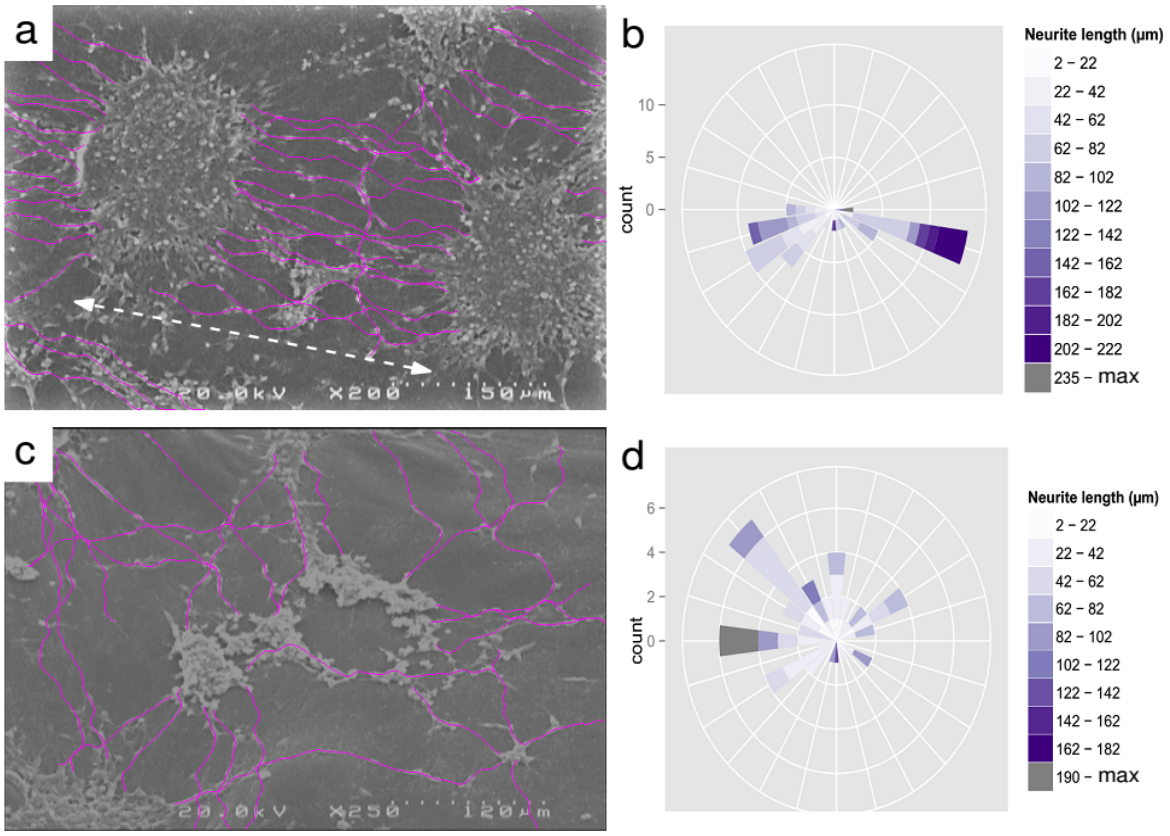

*Figure **3.15**: (a) SEM images of neurites alignment. The arrow indicates the LAB pattern direction. (b) Windrose plot showing the orientation of traced neurites. The color scale represents the length of neural processes (c) The SEM image of the control sample, without LAB pattern, confirms the isotropic orientation (d) of the neural processes when cells grow on substrates without chemical cues.*

This anisotropic feature is not present in the control experiment, where neural stem cells have been cultured in the absence of laminin bioprinting (see Fig. 3.15c). During the differentiation process, the laminin pattern appears to influence the direction of neurite growth, more than the positioning of the cell's soma, which is instead regulated by secreted factors. Moreover, the growth of cell aggregates is three-dimensional with neuron precursors extending from the center of the clusters.
Whether the adhesion promoting chemical cues could be sufficient to determine the direction of growing neural network was addressed in the control experiment, where the laminin droplets array was aligned on the surface upon flat, non degraded, PLGA substrate. On the same scaffold, but on different location, the surface morphology of PLGA was changed by incubation with PBS buffer.
The results show that the neural stem cells are able to differentiate only on the areas where the morphology of PLGA yields a larger surface roughness. The laminin pattern, without effective surface roughness morphology, is not sufficient to achieve the proper environment for growth and differentiation of neural cells' aggregates. No evident neurites orientation could be obtained, except for few isolated cells.

3.5 Discussion and conclusions

The detailed description of the influence of micro and nanoscale roughness upon stem cell differentiation is still under debate [17]. Several works in recent literature have proposed a mechanism of selective differentiation by means of linear micropatterns [18], [19] or nanometric ridge/groove arrays that induce differentiation of human embryonic stem cells into neurons [20]. However most of the literature employs simultaneously a fabrication process to accomplish a topographical cue on the scaffold surface and a functionalization process to anchor adhesion proteins or peptides over the topographical guidances.

Previous works reported in literature on the alignment induced by microstructures fabricated on the scaffolds are based on a strict spatial correlation between the topographical features and chemical cues (i.e. laminin stripes). In cases where the topographic element, favoring cell growth, is obtained with fabrication methods that modify the surface roughness, generally the chemical cue is made by a functionalization of the overall surface, or by diffusion processes that segregate the molecules on the surface during the fabrication of the scaffold. In our case, we tried to separate the processes to make uncorrelated overlapping between topographic stimulus (surface with high roughness) and chemical functionalization. This was achieved using an additive and low-impact technique as the Laser Assisted Bioprinting.

We performed fabrication and functionalization of biodegradable scaffolds, in order to decouple the two effects: the roughness increase of partially degraded PLGA scaffold and the functionalization, in specific areas, with laminin, a protein promoting cell adhesion.

Microdroplets of laminin solution were deposited on PLGA scaffolds; the polymer surface on which the droplets collide has a roughness varying approximately between 10 nm to 60 nm. The coverage of laminin was estimated by a threshold algorithm from the AFM images and is reported in Figure 3.3 for all the concentrations. The total coverage increases with time and reaches a saturation level, after 120 minutes. The morphology of the Laminin film is made up together by a carpet of molecules and large aggregates; the first has an average height of less than 10 nm, the aggregates rise till more than 30 nm. The film growth resembles random sequential adsorption, since aggregates with 3D structure are formed preserving the underlying monolayer (See arrows in Figure 3.2).

The trend of coverage increase versus time is consistent with all the initial concentrations and may be exploited to fabricate a pattern with less than 100 molecules per μm^2. The laminin is generally confined within the droplets footprint, however the aggregates appear to be weakly adsorbed on PLGA, as the washing step in some cases displaces the layers of protein deposited on top of the first adsorbed layer.

The PLGA scaffold surface has characteristic pores, due to the evaporation of the solvent during casting. The distribution of pore diameters is homogeneous and can be described with the appearance of breathing figures in humid environment. We made changes at the topographical level by means of hydration in PBS solution. This partial degradation

has determined over the entire surface of the scaffold a significant increase of the roughness, up to 60 nm (see Figure 3.4).
It is important to stress at this point, that during the cell adhesion experiment, the morphology of the PLGA surface was not significantly changed by LAB patterning at the scale of single cell. If we look at the correlations between the LAB pattern and the focal contacts of adhering cells, we can assess whether the laminin pattern is really influential for the placement of each cell. The optical fluorescence images from focal contacts immunostaining were compared with the droplets pattern immediately after deposition. The power spectrum densities (PSD) of the two images revealed that the correlation length ξ_p, relative to the mean statistical distance between the laminin droplets, can be observed also in the PSD calculated from the images of focal points (see Figure 3.5). This accounts for a statistical close relationship between the laminin spots and the position of the focal contacts, during adhesion. The recurrence of this correlation length on the PSD spectra of the cell culture is characterized by a broader peak with respect to the periodicities of the droplets array. This effect can be explained by the intrinsic variability of the cell culture, as well as natural displacement occurring during adhesion and proliferation.
Cell adhesion has been assessed also on PLGA films patterned with Laminin droplets spaced apart at increasing distances from 40, 70 'till 100 μm. From the analysis made by the mathematical simulation, the probability of adhesion (PA) as a function of pattern geometry (d) increases when droplet distance decreases; however, the quantitative and statistical evaluations made by Mark Connection Function calculation disclose a difference in this estimated probability. In fact the probability of adhesion on droplets spaced 70 μm is less than the probability on droplets spaced 100 μm, and the trend is not linear as we can predict. There can be two reasons to explain these dissimilar results: the first reason lie on the simulation parameters that maybe have been set too much "small" for what concerns cell-substrate interaction (i.e. PLGA surface set more anti-fouling). The second cause is probably due to the experimental data, maybe insufficient for a correct statistical evaluation. For better elucidating this incongruity, other simulations and further experiments need to be performed in the future.
Alignment of neurites on the pattern obtained with LAB represents an experimental result not yet described in the literature. In the present work, the induced alignment has been investigated by looking at the connections between groups of stem cells that are facing differentiation. Previous works focused the attention just on the extension of neural processes from a population of primary neurons, in the presence of geometrical confinement [21]–[23]. Exerting a control on the alignment between connections of developing neural networks is interesting for potential applications in the field of regenerative medicine, because the patterning protocol can be exploited for integration of implants that promote regeneration of nervous tissues, after a trauma, according to a geometry required for the correct function recovery [24], [25].
The development of neural processes statistically oriented along the array of laminin droplets follows in time the growth of clusters of differentiated stem cells, which, on their behalf, start to synthetize laminin in the phase of differentiation. The potential

attraction exerted by the pattern depends on the concentration of the adhesion proteins on the surface that must exceed the one synthetized by the cells in the surrounding of the cellular membrane.

Results show the clear effect of the LAB pattern of laminin on PLGA on the growth of thicker neuronal processes along a preferential direction. Moreover the length of neurites arranged along the preferential axis is larger than the length of neurites protruding in other directions. From the applicative point of view, along the direction of the pattern we are able to build interconnected networks starting from an initial seed of stem cells.
The statistical analysis of alignment was performed in order to compare the distribution of neurites with circular uniform distribution. Several tests were applied to the vectors containing the sampled angles (Watson, Kuiper and Rayleigh) [26], [27] and all of them returned statistics rejecting the uniform null hypothesis. The percentage of neurites aligned along the axis of the pattern is larger than 2/3, whereas the remaining 1/3 is still distributed in an isotropic way on the substrate and reflects the tendency of cell aggregates to look for chemical cues in every direction.
The morphology of neurites is influenced by the topographical characteristics of the substrate upon which they develop. The wavy path behavior has been observed also on neurites growing isotropically upon PLGA substrates, which were not patterned with LAB, confirming the hypothesis that surface topography, obtained on PLGA scaffold by hydration, plays a major role in the differentiation processes.

We presented Laser Assisted Bioprinting [28] as a new technology for patterning biodegradable scaffolds to be employed in regenerative medicine. The capability to optically see through the LAB target and align the beam with the underlying substrate features represents, in our opinion, a step ahead in the microfabrication of implantable devices for nerve regeneration. Within the described experiments, LAB was applied to pattern arrays of laminin droplets upon PLGA scaffolds, with variable surface roughness. We found that neural stem cells adhere upon laminin pattern, also when PLGA had no topographic guidance. Differentiation, however, occurs only in presence of hydrated PLGA scaffolds, with roughness larger than 60 nm. The presence of laminin spots induced anisotropic orientation of the neurite processes from large clusters of cells.
Exploitation of simple microfabrication steps, to tailor the morphological and chemical cues for adhesion and differentiation, represents a valuable tool in engineering devices for studying the recruiting and differentiation of autologous stem cells.

Materials and Methods

Bioink-Ribbon preparation.

The laminin stock solution [500µg/ml] is diluted first in bi-distilled water and then in glycerol 1:2 to a final protein concentration ranging between 15µg/ml and 150µg/ml. The ribbons used were supplied by Organic Spintronics s.r.l. and consist in glass slides coated by Pulsed Plasma Deposition (PPD) with a stainless steel layer (thickness = 20 nm). PPD is a physical vapor deposition (PVD) technique employed to deposit thin films of numerous materials such as oxides, complex oxides, nitrides, carbides, carbon based films, semiconductors, etc. The deposition of thin films using PPD is done by ablation of a target material using a fast pulse of electrons (100 ns) and the material is deposited on the substrate. Ablation by the fast electron beam causes the formation of an hot, dense, and high-velocity plasma. The ribbons were cleaned in Ethanol 99,9% (15' sonication) and then gently dried with nitrogen flow. Before the deposition of the Bioink, each ribbon was placed in plasma chamber (5', 30 mA) in order to make the surface more hydrophilic and suitable for spin-coating of target solution. A volume of the Bioink solution was spread onto the metallic layer of the ribbon forming a film of about 10 µm thick. Finally the ribbon was placed over the receiving substrate, using two PDMS spacers in between (approximate thickness = 600 µm).

Substrate preparation

PLGA was purchased from Sigma Aldrich (P1941, lactide:glycolide (75:25), mol wt 66000-107000). PLGA films (thickness= 20µm) were prepared by solution casting using 5%wt PLGA chloroform solution onto a cleaned glass substrate in a confining elastomeric frame (1,2cm x 1,2cm) or onto cleaned circle coverslips (∅ 1cm). The glass slides, the circle coverslips and the elastomeric confining frames were cleaned with 15' sonication in Ethanol 99,9% and allowed to dry under chemical hood. Then the frames, when used, were mounted on the glass surfaces taking care to make them adhering to each other. Once the PLGA was completely dissolved in chloroform, the liquid solution was poured onto the glass slides. After the complete evaporation of chloroform (5h in oven 37°C), the frame was removed from the slides. The resulting transparent film was then sterilized before use.
Samples of PLGA scaffolds were further processed to obtain substrates with controlled roughness as reported in Fig.3.4 (Chapter 3). To obtain hydration and roughening of the scaffold, PLGA has been incubated in PBS buffer, 0.1x, for 24 hrs at 37 ° C. After incubation the PLGA film was rinsed in deionized water. To obtain scaffolds with chemical cues, the PLGA thin film, non hydrated, was used as substrate for LAB. The two protocols have been performed as consecutive steps in order to achieve a scaffold with both increased surface roughness and chemical functionalization. The films were incubated with PBS buffer for 24 hours, and subsequently the corrugated thin film was patterned with microdroplets of laminin. LAB allows patterning of biomolecules also on substrates with high roughness

since the drop impacts the substrate with high kinetic, overcoming the resistance to wetting induced by increased roughness.

Laser Assisted Bioprinting

The Laser Assisted Bioprinting workstation in ScribaR setup (see Figure 2.2 in Chapter 2), consists of a laser source: a solid Nd:YAG crystal laser (1064 nm wavelength, 10ns pulse duration, frequency in a range of 5-50 Hz, variable driving voltage from 7500 to maximum 9000mV) and a precision motor stage for an accurate positioning of the samples. The Laser Assisted Bioprinting system is controlled by a dedicated software (Laser Mark) that allows the fabrication of the pattern starting from an externally supplied CAD file describing the desired geometry and features. The software itself allows directly tailoring the pattern by drawing vectorial projects and tuning the timing and intensity of the laser pulses.
As specified in previous section the Ribbon was coupled with the receiving poly(lactic-co-glycolic acid) (PLGA) substrate by means of two elastomeric supports, keeping a gap of 600 μm between the corresponding facing surfaces. A fast infrared laser beam, with pulse width of 10 ns, was focused on the target to emit a single pulse of approximately 15 mW on a spot of 20 μm in diameter. The laser pulse irradiates the metallic layer, which absorbs the energy and consequently heats up the metal to the melting point, within few picoseconds. The liquid metal is vaporized by further nanosecond laser absorption. Afterwards, the gas expands in all direction and encounters less resistance at the level of Bioink, facing the PLGA scaffold. Finally a liquid jet is emitted, travelling at a large speed towards the substrate and breaking up into fine droplets induced by concurrent Rayleigh instabilities.

Laminin pattern characterization

Protein patterns were characterized by different microscopy techniques. Optical microscopy (Olympus BX51, software Infinity) was employed mostly during the bioprinting session to provide a rapid detection of the droplets deposited onto the substrate. Atomic Force Microscopy (AFM) has been used to achieve a high resolution surface characterization of the patterned areas. AFM images were acquired with a Smena microscope (NT-MDT, Moskow, Russia) operated in semicontact mode under ambient conditions. The cantilevers employed were NSG01 (NT-MDT, Moscow, Russia) with a nominal tip radius of curvature of 10 nm and a resonance frequency of between 87 and 230 kHz. Images were analyzed using the opensource software Gwyddion ; the size and the height of the pattern features were measured by the section analysis tool. SEM analyses were performed using a SEM-FEG Hitachi S4000 (Vext = 20 keV; i = mA) (Hitachi, Tokyo, Japan). Immunofluorescence assays were performed using a specific anti-laminin primary antibody produced in rabbit (Sigma Aldrich L9393) and a secondary fluorescent antibody (AlexaFluor 594 Goat Anti-Rabbit IgG, Invitrogen A11012). Bioprinted laminin samples were blocked for 30 min with phosphate buffer saline (PBS) 1X containing 1% bovine

serum albumin (blocking solution). They were incubated 1h at room temperature with antilaminin antibody diluted 1:25 in blocking solution, washed three times with PBS 1X, and incubated for 90 min at room temperature with the fluorescent Alexa Fluor 594 anti-rabbit antibody diluted 1:200 in PBS 1X. The fluorescent signal has been detected using optical microscopy (Nikon Eclipse 80i, software NIS-Elements) equipped with high pressure mercury lamp (Nikon).

Cell culture and characterization

Maintenance of stem cell line NE4C was carried out according to the published protocol [29]. *The stem cells were seeded at 25000 cells per cm^2 in a final volume of 400 μL of the complete medium (CM) (MEM containing 10% FBS, 4 mM glutamine, 40 mg/ml, 1 gentamicin and 2.5 mg/ml, 1 amphotericin) and incubated under the standard cell culture conditions (37°C, 5% CO2 and 95% relative humidity).*
Cell differentiation, when performed, was induced by replacing CM, after 3 hours, with the differentiation medium composed of DMEM-F12 Ham (1:1), ITS 1X, 4mM glutamine, 40 μg ml^{-1} gentamicin and 2.5 μg ml^{-1} amphotericin (DM), containing all-trans retinoic acid (RA) 1μM, according to protocol already reported in literature [30] [31]. *After 2 days, the DM was replaced by DM containing 40 ng ml^{-1} brain-derived neurotropic factor (BDNF). Half of the DM was then changed every subsequent day by replacing it with DM, without any inducers until the end of experiment.*

Immunostaining

Immunofluorescence of actin cytoskeleton and focal adhesions was performed with the Millipore staining kit (FAK 100) that contains fluorescent-labeled Phalloidin (TRITC-conjugated Phalloidin) to map the local orientation of actin filaments within the cell and a monoclonal antibody to Vinculin that is specific for the staining of focal contacts in cells. DAPI staining for the fluorescent labeling of nuclei was carried out simultaneously.
Immunofluorescence staining of β-Tubulin III, a neural differentiation marker, was performed co-labeling the nuclei with DAPI [32]. *All the images were captured using an epifluorescence microscope (Nikon Eclipse 80i) endowed with NIKON excitation band DAPI-FITC-TRITC filter set and equipped with a digital camera (Nikon-DS-Fi1).*
The morphology of the cells was monitored by using an optical microscopy (Nikon Eclipse 80i) at different times of incubation. Samples of differentiated cells were analyzed by Scanning Electron Microscopy (SEM). For SEM sample preparation, the cells were fixed with 2.5% glutaraldehyde (1 hr; 4°C), post-fixed with 1% osmium tetroxide (1 hr; r.t.) and then dehydrated in an increasing series of ethanol concentrations. Subsequently, a gold thin film coating (10 nm) was sputtered before analysis with a SEM-FEG Hitachi S4000.

Statistics of neurite alignment

Alignment of neurites has been calculated, starting from SEM images, from cells cultivated 11 days since the beginning of the differentiation protocol. Morphological contrast given by SEM image provides the coordinates of neural processes connecting populations of cells. These neurites have been tracked using NeuronJ software [33] *as a plugin of image analysis software ImageJ. The route of advancing neurites has been traced with coordinates of consecutive segments approximating the shape of the neural process. The orientation of the line joining the starting and final points was classified according to the main direction of the pattern of adhesion protein, with histograms in polar coordinates that report in color scale the length of analyzed neurites. Particular attention has been paid in selecting only neurites and elements clearly visible, excluding fake positives, which may come from the thick population of cells. Use of SEM images instead of fluorescence microscopy, in present evaluation, is due to the conditions of the biodegradable polymeric substrate. After 11 days of culture, the PLGA scaffold was not transparent, due to bulk degradation processes; therefore fluorescence microscopy returned low contrast images.*

Bibliography

[1] K. E. Schmalenberg and K. E. Uhrich, "Micropatterned polymer substrates control alignment of proliferating Schwann cells to direct neuronal regeneration," *2005*, vol. 26, pp. 1423–1430.

[2] C. E. Schmidt and J. B. Leach, "Neural tissue engineering: strategies for repair and regeneration.," *Annu. Rev. Biomed. Eng.*, vol. 5, pp. 293–347, Jan. 2003.

[3] F. Cimadamore, K. Fishwick, E. Giusto, K. Gnedeva, G. Cattarossi, A. Miller, S. Pluchino, L. M. Brill, and A. V. Bronner-Fraser, M. Terskikh, "Human ESC-Derived Neural Crest Model Reveals a Key Role for SOX2 in Sensory Neurogenesis.," *Cell Stem Cell*, vol. 8, pp. 538–551, 2011.

[4] W. Daly, L. Yao, D. Zeugolis, A. Windebank, and A. Pandit, "A biomaterials approach to peripheral nerve regeneration: bridging the peripheral nerve gap and enhancing functional recovery," *J. R. Soc. Interface*, vol. 9, pp. 202–221, 2012.

[5] L. Yao, S. Wang, W. Cui, R. Sherlock, C. O'Connell, G. Damodaran, A. Gorman, A. Windebank, and A. Pandit, "Effect of functionalized micropatterned PLGA on guided neurite growth," *Acta Biomater.*, vol. 5, pp. 580–588, 2009.

[6] J. Xie, M. R. MacEwan, X. Li, S. E. Sakiyama-Elbert, and Y. Xia, "Neurite Outgrowth on Nanofiber Scaffolds with Different Orders, Structures, and Surface Properties," *ACS Nano*, vol. 3, pp. 1151–1159, 2009.

[7] D. Lang and P. Coates, "Diffusion coefficient of DNA in solution at 'zero' concentration as measured by electron microscopy," *J. Mol. Biol.*, vol. 36, pp. 137–151, 1968.

[8] K. Onuma and N. Kanzaki, "Size Distribution and Intermolecular Interaction of Laminin-1 in Physiological Solutions," *J. Phys. Chem. B*, vol. 107, no. 42, pp. 11799–11804, 2003.

[9] M. Rabe, D. Verdes, and S. Seeger, "Understanding protein adsorption phenomena at solid surfaces," *Adv. Colloid Interface Sci.*, vol. 162, no. 1–2, pp. 87–106, Feb. 2011.

[10] X. Zeng and S. Li, "Multiscale modeling and simulation of soft adhesion and contact of stem cells," *J. Mech. Behav. Biomed. Mater.*, vol. 4, pp. 180–189, 2011.

[11] J. M. V. A. Koelman and P. J. Hoogerbrugge, "Dynamics simulations of hard-sphere suspensions under steady shear," *Europhys. Lett.*, vol. 21, pp. 363–368, 1993.

[12] J. L. Jones, M. Lal, J. N. Ruddock, and N. A. Spenley, "Dynamics of a drop at a liquid/solid interface in simple shear fields: A mesoscopic simulation study," *Faraday Discuss.*, vol. 112, pp. 129–142, 1999.

[13] H. M. Kowalczyńska, M. Inkielman, M. Nowak-Wyrzykowska, L. Stołowska, and J. Doroszewski, "Interaction of L1210 cells with sulfonated polystyrene in the absence of serum: Adhesion and three-dimensional cell shape," *Colloids Surf. B. Biointerfaces*, vol. 30, pp. 193–206, 2003.

[14] M. Ventre, F. Valle, M. Bianchi, F. Biscarini, and P. a Netti, “Cell fluidics: producing cellular streams on micropatterned synthetic surfaces.,” *Langmuir*, vol. 28, no. 1, pp. 714–21, Jan. 2012.

[15] V. J. Martinez, P. Arnalte-Mur, and D. Stoyan, “Measuring galaxy segregation using the mark connection function,” p. 6, Jan. 2010.

[16] A. Satoh, *Introduction to Molecular Microsimulation for Colloidal Dispersions*. Elsevier, 2003.

[17] I. Tonazzini, E. Bystrenova, B. Chelli, P. Greco, P. Stoliar, A. Calo, A. Lazar, F. Borgatti, P. D’Angelo, C. Martini, and F. BIscarini, “No TitleMultiscale Morphology of Organic Semiconductor Thin Films Controls the Adhesion and Viability of Human Neural Cells,” *Biophys. J.*, vol. 98, no. 12, pp. 2804–2812, 2010.

[18] B. Chelli, M. Barbalinardo, F. Valle, P. Greco, E. Bystrenova, M. Bianchi, and F. Biscarini, “Neural cell alignment by patterning gradients of the extracellular matrix protein laminin,” *Interface Focus*, vol. 4, 2013.

[19] L. Qi, N. Li, R. Huang, Q. Song, L. Wang, Q. Zhang, R. Su, T. Kong, M. Tang, and G. Cheng, “The Effects of Topographical Patterns and Sizes on Neural Stem Cell Behavior,” *PLoS One*, vol. 8, no. 3, p. e59022, Mar. 2013.

[20] M. R. Lee, K. W. Kwon, H. Jung, H. N. Kim, K. Y. Suh, K. Kim, and K.-S. Kim, “Direct differentiation of human embryonic stem cells into selective neurons on nanoscale ridge/groove pattern arrays,” *Biomaterials*, vol. 31, no. 15, pp. 4360–4366, 2010.

[21] J. M. Corey, D. Y. Lin, K. B. Mycek, Q. Chen, S. Samuel, E. L. Feldman, and D. C. Martin, “Aligned electrospun nanofibers specify the direction of dorsal root ganglia neurite growth,” *J. Biomed. Mater. Res. Part A*, vol. 83A, no. 3, pp. 636–645, Dec. 2007.

[22] F. Johansson, P. Carlberg, N. Danielsen, L. Montelius, and M. Kanje, “Axonal outgrowth on nano-imprinted patterns,” *Biomaterials*, vol. 27, no. 8, pp. 1251–1258, Mar. 2006.

[23] I. Tonazzini, S. Meucci, P. Faraci, F. Beltram, and M. Cecchini, “Neuronal differentiation on anisotropic substrates and the influence of nanotopographical noise on neurite contact guidance,” *Biomaterials*, vol. 34, no. 25, pp. 6027–6036, Aug. 2013.

[24] C. Cossetti, C. Alfaro-Cervello, M. Donegà, G. Tyzack, and S. Pluchino, “New perspectives of tissue remodelling with neural stem and progenitor cell-based therapies,” *Cell Tissue Res.*, vol. 349, no. 1, pp. 321–329, Jul. 2012.

[25] M. Cusimano, D. Biziato, E. Brambilla, M. Donegà, C. Alfaro-Cervello, S. Snider, G. Salani, F. Pucci, G. Comi, J. M. Garcia-Verdugo, M. De Palma, G. Martino, and S. Pluchino, “Transplanted neural stem/precursor cells instruct phagocytes and reduce secondary tissue damage in the injured spinal cord,” *Brain*, vol. 135, no. 2, pp. 447–460, Jan. 2012.

[26] G. N. Li and D. Hoffman-Kim, “Evaluation of neurite outgrowth anisotropy using a novel application of circular analysis,” *J. Neurosci. Methods*, vol. 174, no. 2, pp. 202–214, Sep. 2008.

[27] J. A. Mitchel and D. Hoffman-Kim, “Cellular Scale Anisotropic Topography Guides Schwann Cell Motility,” *PLoS One*, vol. 6, no. 9, p. e24316, 2011.
[28] B. Guillotin, A. Souquet, S. Catros, M. Duocastella, B. Pippenger, S. Bellance, R. Bareille, M. Rémy, L. Bordenave, J. Amédée, and F. Guillemot, “Laser assisted bioprinting of engineered tissue with high cell density and microscale organization.,” *Biomaterials*, vol. 31, no. 28, pp. 7250–6, Oct. 2010.
[29] Z. Környei, V. Szlávik, B. Szabó, E. Gócza, A. Czirók, and E. Madarász, “Humoral and contact interactions in astroglia/stem cell co-cultures in the course of glia-induced neurogenesis.,” *Glia*, vol. 49, no. 3, pp. 430–444, 2005.
[30] Z. Kornyei, E. Gozca, R. Ruhl, B. Orsolits, E. Voros, B. Szabó, B. Vagovits, and E. Madarász, “Astroglia-derived retinoic acid is a key factor in glia-induced neurogenesis,” *FASEB J.*, vol. 21, no. 10, pp. 2496–2509, 2007.
[31] T. Cramer, B. Chelli, M. Murgia, M. Barbalinardo, E. Bystrenova, D. M. de Leeuw, and F. Biscarini, “Organic ultra-thin film transistors with a liquid gate for extracellular stimulation and recording of electric activity of stem cell-derived neuronal networks,” *Phys. Chem. Chem. Phys.*, vol. 15, no. 11, pp. 3897–3905, Feb. 2013.
[32] B. I. Tarnowski, F. G. Spinale, and H. J. Nicholson, “DAPI as a useful stain for nuclear quantitation,” *Biotech. Histochem.*, vol. 66, pp. 297–302., 1991.
[33] E. Meijering, M. Jacob, J.-C. f. Sarria, P. Steiner, H. Hirling, and M. Unser, “Design and validation of a tool for neurite tracing and analysis in fluorescence microscopy images,” *Cytom. Part A*, vol. 58A, no. 2, pp. 167–176, Apr. 2004.

Chapter 4 - Laser Assisted Bioprinting of Laminin micrometric spots on cantilevers

In collaboration with the Politecnico of Torino, we implemented Laser Assisted Bioprinting for the functionalization of Microcantilevers (MCs) with Laminin droplets. The idea originated from the combination of our expertise and knowhow on this deposition technique and the cantilever frequency resonance analysis aiming at the fabrication of a novel type of biosensor.

4.1 (Micro)Cantilevers-based biosensors

A biosensor measures the physicochemical changes that a biological recognition layer, usually attached to a solid transducer, undergoes when it interacts with a sample that contains the targeted molecules. Thus it harnesses the capability of some biomolecules (receptors) to specifically bind and recognize complementary biomolecules (ligands).
Biosensors are increasingly demanded in fundamental biological studies, health science research, drug discovery and clinical diagnosis. The physicochemical change has to be transduced into a measurable signal and, depending upon the nature of the transduction signal, biosensors can be classified into optical, electrical and mechanical (Figure 4.1a). Advances in micro- and nano-fabrication technologies enable us to achieve increasingly smaller mechanical transducers with micro- and nano-sized moving parts whose deformation and vibration are sensitively modified upon molecular adsorption. The use of well established semiconductor technology enables the batch-production of arrays of hundreds of nanomechanical systems. Nanomechanical biosensors are usually cantilever-shaped [1].
A microcantilever is a single side clamped beam commonly fabricated from silicon (Si) or polymers, whose typical dimensions correspond to: length ≈ 50 –500 μm; thickness = 1 – 10 μm.

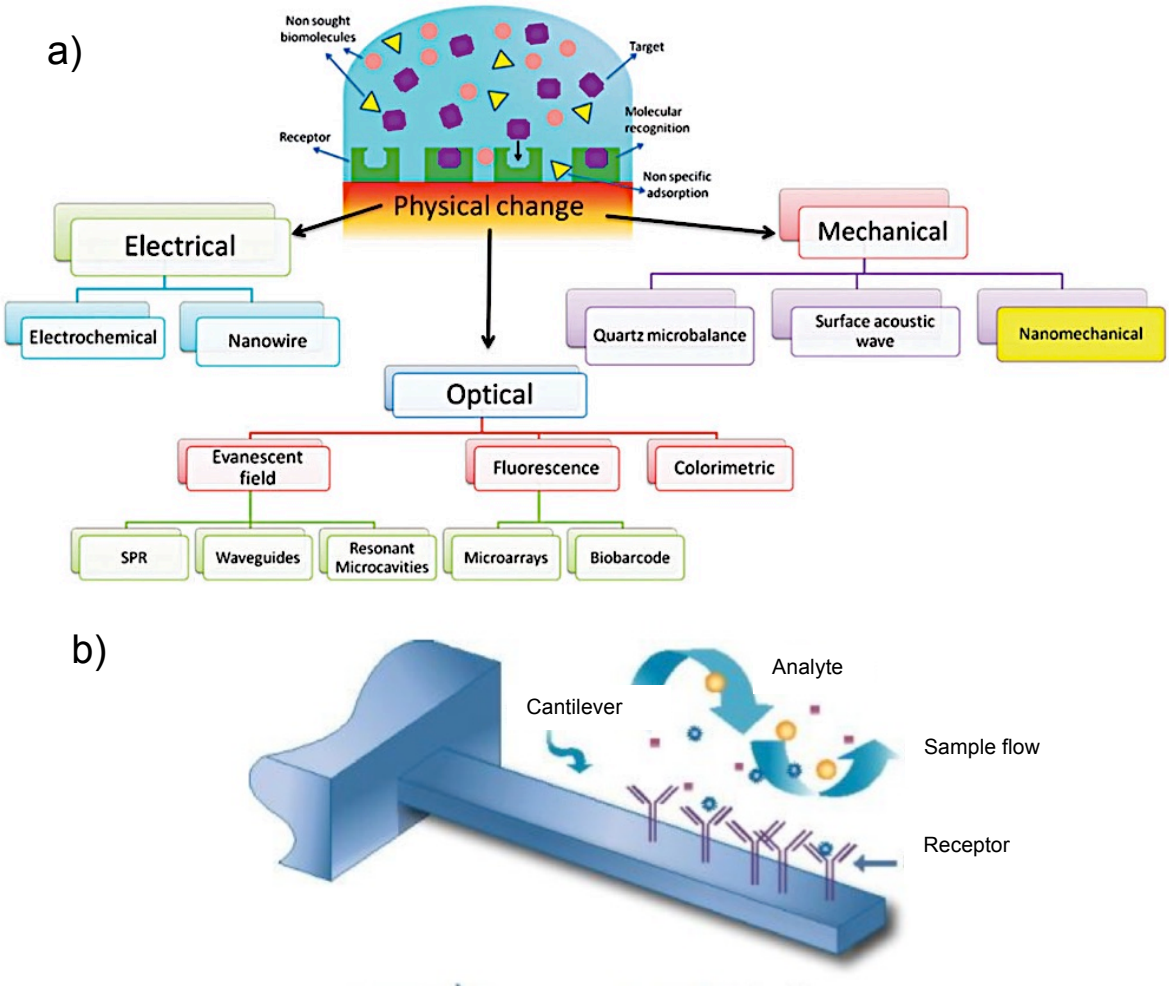

*Figure **4.1**: (a) Schematics of a biosensor and biosensor subclasses. Depending on the kind of physical change that is measured in the transducer surface, biosensors can be divided into electrical, optical and mechanical biosensors. Each category includes different types of biosensor devices. (b) Biosensor cantilever-based scheme.*

The working principle is simple: the microcantilever is functionalized with the proper probes that can selectively bind target molecules. This functionalized microcantilever is then placed into an environment that includes the target compounds and the interactions between the binding sites of the probes and those target compounds bring to a change in the mechanical response of the system (see Figure 4.1b). The readout of this deviation is at the base of the sensing mechanism.

In comparison to quartz crystal resonators, the increasingly smaller size of nanomechanical systems produces outstanding mass resolution on the boundary of single atoms. Furthermore, nanomechanical systems can exhibit very low mechanical compliances translating biomolecular recognition events into measurable displacements. Since the size of the biomolecules is comparable to one of the dimensions of the mechanical system, mainly the thickness, the mechanical response is also extremely sensitive to the mechanical properties of the adsorbed biomolecules, making this tool unique.

Their sensitivity is very high and is also possible to do a label-free quantitative measurement of biomolecular interactions. They have been used to measure the mass of cells and biomolecules [2], concentrations of dilute cell suspensions [3], nucleic acids [4], as well as bacterial and fungal growth [5]. They have been extensively investigated also for low-level detection applications and for studying biomolecular interactions. There are two modes in which cantilever sensors are used: the *static-mode* and the *dynamic-mode* depending on whether the static displacement or the resonant properties of the nanomechanical system are measured (Figure 4.2). In the first one, the biomolecular interactions are sensed by binding-induced changes in the cantilever deflection caused by differential surface stress. The dynamic-mode (also called resonant-mode) is based on binding-induced changes in cantilever resonant frequency caused by mass-change or stiffness-change. Thus, in the dynamic-mode, the surface biochemical binding is sensed directly since the resonant frequency is a function of the cantilever mass.
The dynamic-mode cantilever biosensor is the one that is examined in our case.

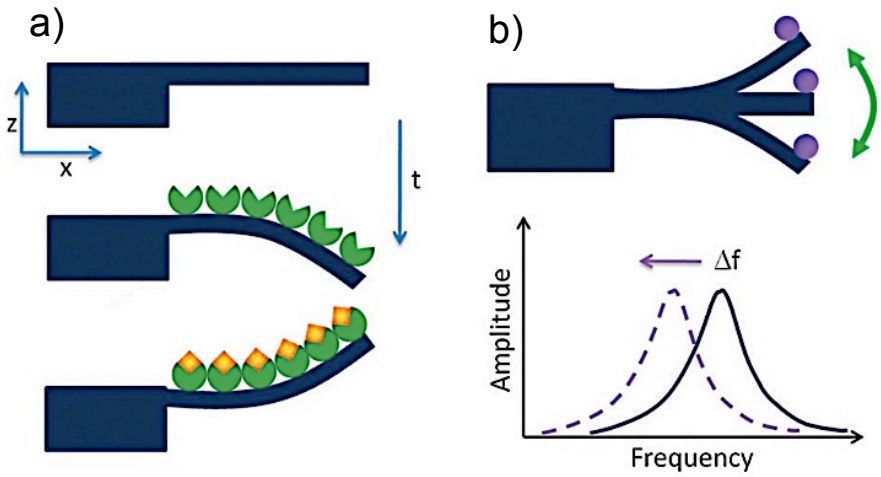

*Figure **4.2**: Main operation modes of nanomechanical biosensors: static mode (a) and dynamic mode (b). In the static mode one side of the cantilever is functionalized to attach a monolayer of biomolecular receptors that exhibit high affinity to the targeted biomolecule. Molecular recognition induces changes in the surface stress of the upper side with respect to the lower that is mechanically relaxed by the cantilever bending. Displacement detection methods directly or indirectly measure the curvature change to derive the surface stress. In the dynamic mode, the cantilever is usually driven at its resonance frequency. When a biomolecule lands on the free end of a cantilever, the resonance frequency shifts downwards due to the added mass.*

The operation of measurement of resonance frequency shifts, in dynamic-mode cantilevers, requires them to be excited by a perturbing driving force. In addition, the resulting motion must be measured and gathered for post-processing through a read-out technique. A variety of different techniques exist for both operations and their

components can either be internal or external to the microcantilever structure. Exciting vibrations using an external source has been possible through the use of electrostatic forces, piezoelectric base elements, thermal noise and optics; while exciting by internal sources means that the excitation has been done via piezoelectric and magnetoelastic active layers, or generating Lorentz forces from embedded circuits. Measurement of resonant frequency using an external component has been done through the use of optical or capacitive techniques. In contrast, measurement using an internal component has been done by measuring property changes of the active layer; examples include electrical impedance, electrical charge or property changes of embedded resistive components in areas of the sensor significantly subjected to mechanical deformation.
The detection mechanisms commonly used for microcantilever sensors are based upon changes in surface stress, resonance frequency, capacitance and resistance induced by the adsorption or attachment of analyte molecules on the cantilever surface. Each of these transduction mechanisms can be associated with the two different operating modes. In *static mode*, cantilever deflections can be caused by intrinsic stresses generated on the cantilever surface or within the cantilever. In *dynamic mode* the cantilever sensors are essentially mechanical oscillators, whose resonance characteristics depend on the attached mass, as well as the viscoelastic properties of the medium

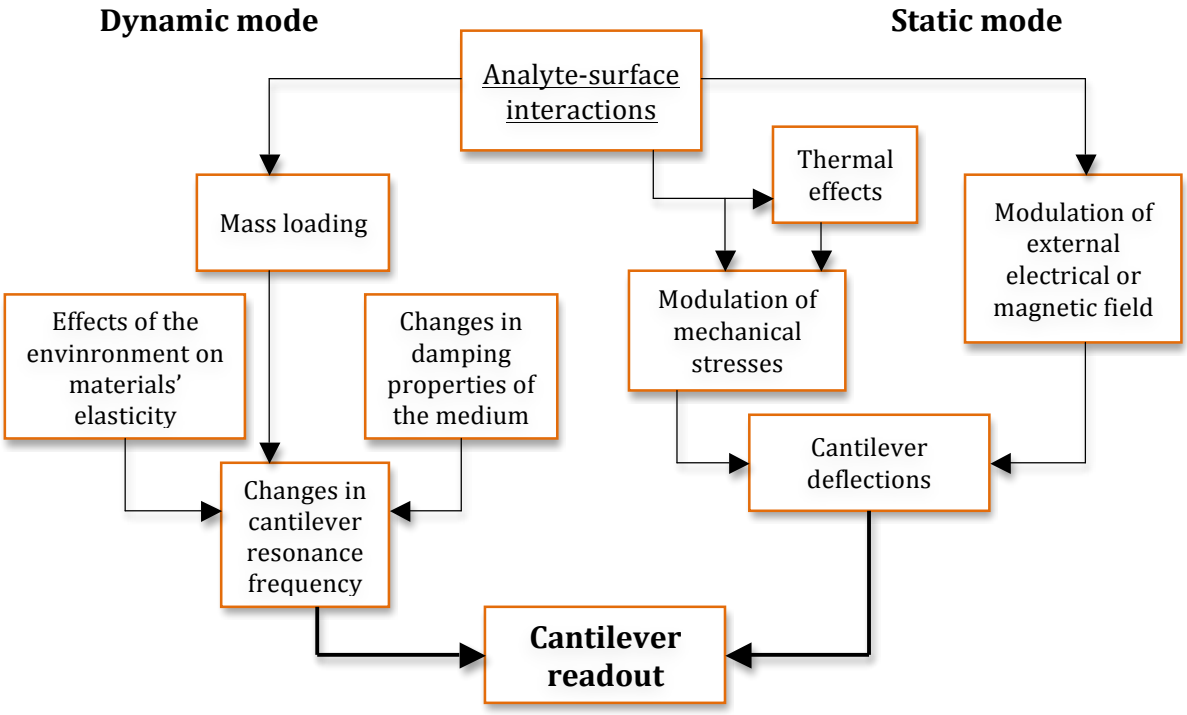

*Figure **4.3**: Scheme of transduction mechanisms of microcantilever sensors.*

The dynamic operation mode is the readout method used in the experimental part of this chapter. In this section, the main features and physical principles of *dynamic mode* microcantilever-based sensors are discussed. In first approximation, the resonant frequency of a microcantilever is dependent on its stiffness, mass and geometry. Changes of the microcantilever mass or stiffness, due to molecule absorption, induce a detectable frequency shift [5], [6].
A microcantilever can be considered as a harmonic oscillator if little displacements, from its equilibrium position, are assumed. Microcantilever transducers, vibrating in gases or in vacuum, can thus be treated as weakly damped mechanical oscillators.
This consideration is very important, because the formula which gives the possibility to make the mass loading evaluation is strictly based on this approximation. The displacement of the free end of the cantilever is directly proportional to the force exerted by the cantilever tip (linear regime described by the Hooke's law):

$$F = -k \cdot z$$

where F is the force related to the displacement z, and k is the cantilever spring constant. For a cantilever vibration the force can be considered as concentrated at the free end of the beam.
In such harmonic approximation, the resonance condition can be evaluated as:

$$f_{\mathrm{n}} = \frac{1}{2\pi}\sqrt{\frac{k}{m^*}}$$

Where f_n is the resonance frequency and m^* is the modal mass of the oscillator, related to the real (physical mass) m as:

$$m^* = nm$$

Where n is a constant related to the geometry of the oscillator and to the vibration mode (for example for the first vibration mode of a rectangular beam). Although the resonant frequency is used to detect molecular binding, a variety of different resonant modes may be used for sensing as illustrated in Figure 4.4, which shows schematics of the various possible resonant mode shapes.

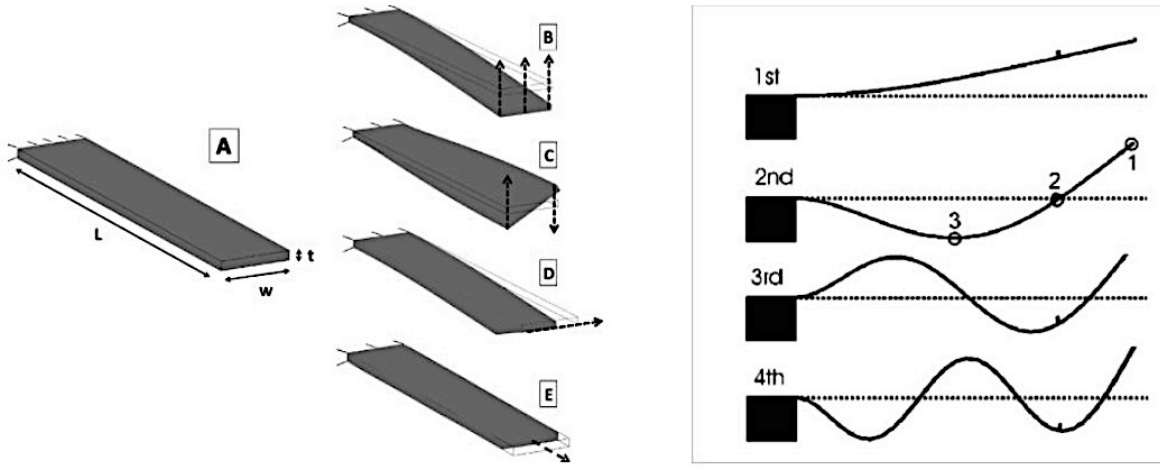

*Figure **4.4**: General schematic of a traditional cantilever (A) and various types of resonant modes found in idealized cantilever sensors (B-E). Transverse mode (B), torsional mode (C), lateral mode (D), and longitudinal mode (E) are shown. Only fundamental mode shapes of each mode are shown for clarity. Displacements are arbitrarily scaled for mode shape clarity. Dashed arrows represent cantilever motion through the resonant cycle.*

Each of the four modes exhibits a resonance condition when excited at its characteristic frequency. Moreover, the cantilevers may exhibit mode coupling depending on the device characteristics. Analytical expressions for various mode shapes can be derived mathematically from the corresponding equations of motion under the following assumptions: the aspect ratio is sufficiently large, the deflection is small compared to cantilever thickness, the geometry is of the single-layer uniform rectangular cross-section and the material is isotropic.
The vibration characteristics depend on the mass of the oscillator, so a mass variation Δm is reflected on a consequent variation of the resonance frequency Δf. Considering a spring constant k independent from the mass variation, the two parameters can be related with this simple approximation:

$$\Delta m = -2 \frac{\Delta f}{f_{\mathrm{n},0}} \cdot m$$

Using this equation is possible to quantify the amount of mass adsorbed during a chemical/biological interaction procedure. Anyway, this equation is founded on an important assumption: the spring constant of the beam remains the same before and after mass change. In other words, surface stress related to external molecules adsorptions is assumed to not affect the cantilever rigidity. It is well established from the static analysis and from theoretical works that formation of a surface adsorbed layer is accompanied by a change in surface stress. If the surface stress influences the spring constant k, the last equation cannot be written and a gravimetric evaluation of surface

changes becomes non-applicable with this simple model. It is yet an open question to understand if this “static” surface stress influences the dynamic properties of the beam. The cantilever vibration is also influenced by the surrounding medium in which the vibration occurs. For example, the drag force related to the surrounding gas has an influence on cantilever vibration characteristics. Obviously, the denser is the medium in which the vibration occurs, the more difficult is the oscillation. In other terms, the quality factor of the oscillator will be lower for vibrations in a denser fluid. This simple fact suggests the idea that a sensor based on oscillating cantilevers finds a more difficult application for measurements in a liquid environment. However, in the last years, the increasing interest in biosensors to carry out real-time measurements in liquid environment has motivated several works concerning the quality factor enhancement.

4.2 Laser Assisted Bioprinting of Laminin on MCs

The microcantilever arrays used in this work have planar dimensions of 7 mm x 7 mm and are composed by 11 microcantilevers each. The reason of this choice is for managing simultaneously multiple signals concerning the same analytical sample. They are manufactured from a silicon substrate material, since single crystal silicon has excellent mechanical properties that allow the design and fabrication of micromechanical structures. Moreover, microcantilever beam structure and mass define the quality of the microcantilever resonator. It is clear that the performance reached is proportional to the natural vibration frequency that is inversely proportional to the effective mass of the structure. The dimensions of microcantilever beams comprising the arrays are of the order of 400-500 μm in length, 7 μm thick and 50 μm width. Those dimensions were engineered in order to facilitate the laser alignment of the readout system and to avoid laser scattering out of the cantilever structure. Center to center distance between each couple of microcantilever beam is 200 μm. A microcantilever array is represented in Figure 4.5.

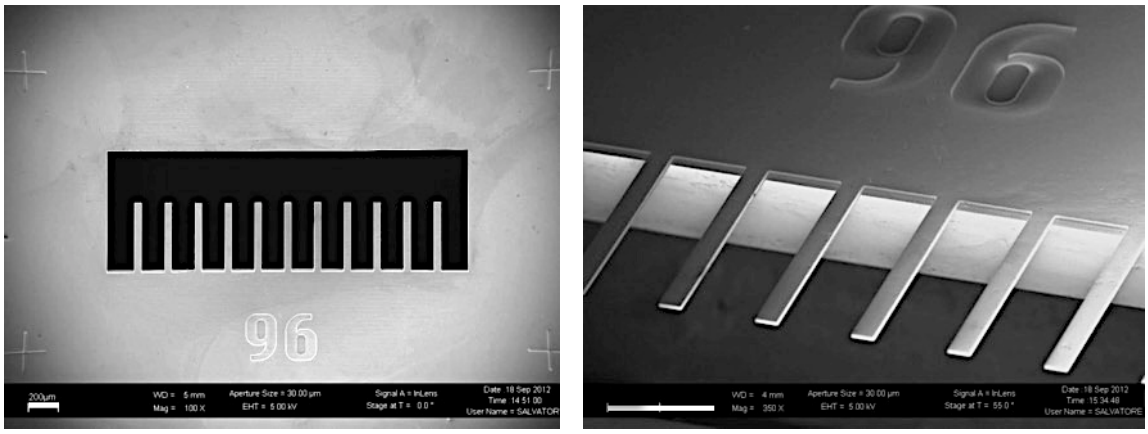

*Figure **4.5**: Design of a microcantilever array: FESEM images kindly provided by Carlo Ricciardi (Politecnico di Torino, Applied Science and Technology Dep.). Scale bar is 200 µm.*

We functionalized 9 out of 11 microcantilevers with Laminin droplets by LAB. The procedure is fully described in "Material and Method" together with the fabrication of the arrays.

The protein deposition has been performed in three different positions on the MCs area as shown in Figure 4.6: on the clumping base, in the mid-zone along the length and on the oscillating end.

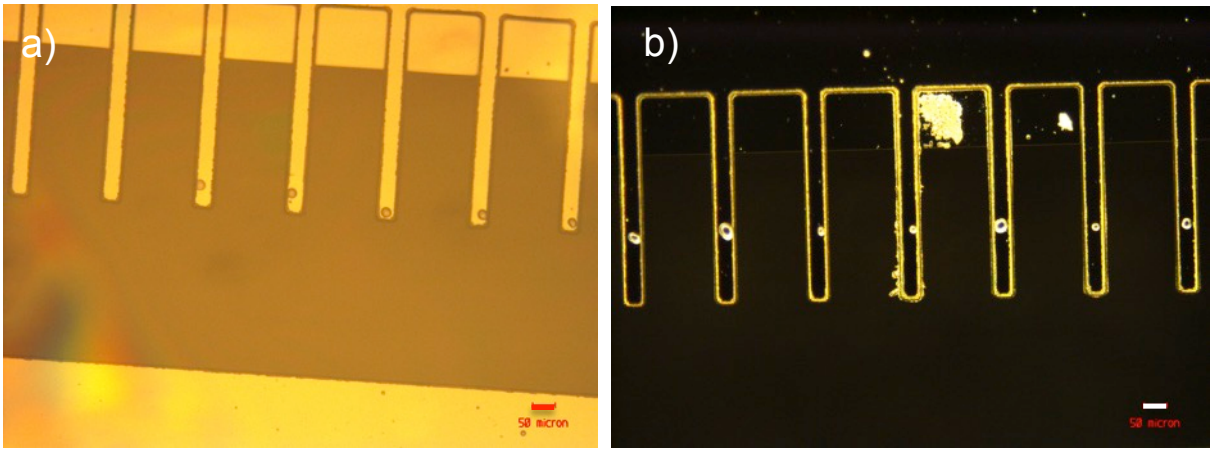

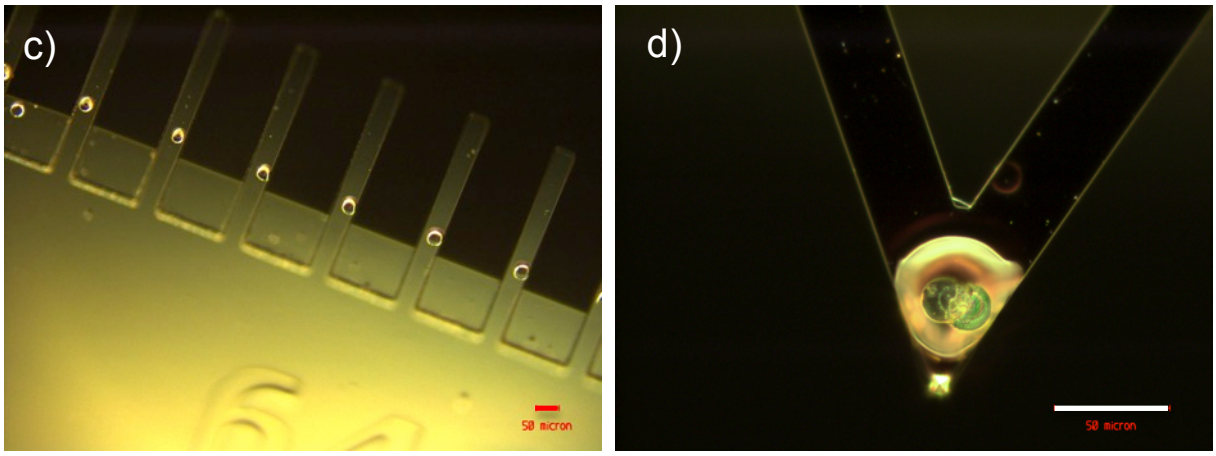

*Figure **4.6**: Laminin spots deposition on Microcantilevers (a) on the oscillating end, (b) in the central part and (c) on the clumping base. In (d), a detail of a higher magnification of another functionalized tip type is shown. Scale bar is 50 μm.*

Frequency resonance has been achieved using the in vacuum high throughput readout and data processing system. The instrument was specifically developed by the company Microla s.r.l. in order to have a suitable, flexible and stable instrumentation able to perform high sensitive, high precise and high throughput cantilever characterizations. The system is able to operate an automatic sequential readout of nine arrays, composed by eleven microcantilevers each, with no limitation in their geometry and size. Automatic measurements of several modes of vibration of microcantilevers, automatic data fitting, data processing and data post processing are required to combine the analysis from different modes of vibration of microcantilever and consequently obtaining more precise results. The detection of the cantilever resonance is made with the optical lever method. The main components of the system apparatus are:

- The actuation system, based on a piezoelectric crystal;
- The readout system: a laser diode focussed on the microcantilever tip surface, and revealed, upon reflection, by a Position Sensitive Detector (PSD);
- The electronics, collecting the signal from the PSD and filtering it from the external noise components before sending it to a pc for the data storage;

The vacuum system, placed over a two-axis motor movimentation, allows the control of the pressure into the chamber where microcantilever arrays are mounted.
A block scheme of the entire experimental set-up is represented in Figure 4.7.

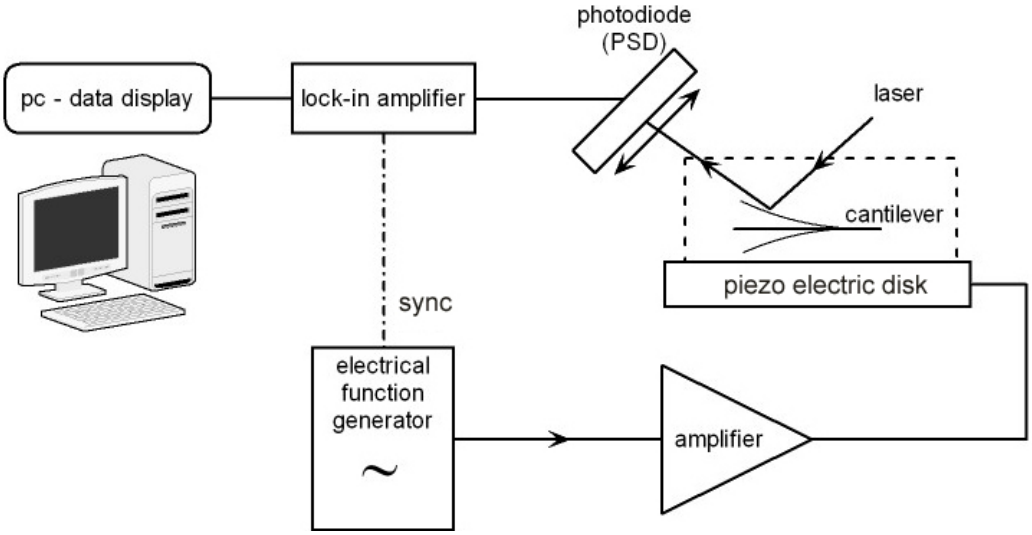

*Figure **4.7**: Schematic of the circuit and components, which constitutes the system for microcantilever sensors characterization.*

More detailed description of the high throughput automatic instrumentation is given in "Materials and Method" section.

4.3 Frequency resonance analysis

First of all, the uncertainty of the experimental set-up in the best conditions was evaluated combining results coming from the first two modes of vibration. The first and second flexural mode of vibration of 2 different arrays were monitored in vacuum: for each cantilever of the array three repeated measurements of their resonant frequency, under the same setup conditions, were performed just breaking the vacuum and repositioning the array in the same holder position. First flexural modes of vibration (M1) were found in the range 41–53 kHz, while second modes (M2) in the range 259–326 kHz.

As already proposed in the literature, but not yet demonstrated with experiments that were not "simulation" or "model" experiments, the position of droplet analyte induces opposite shifts (Figure 4.8).

a)

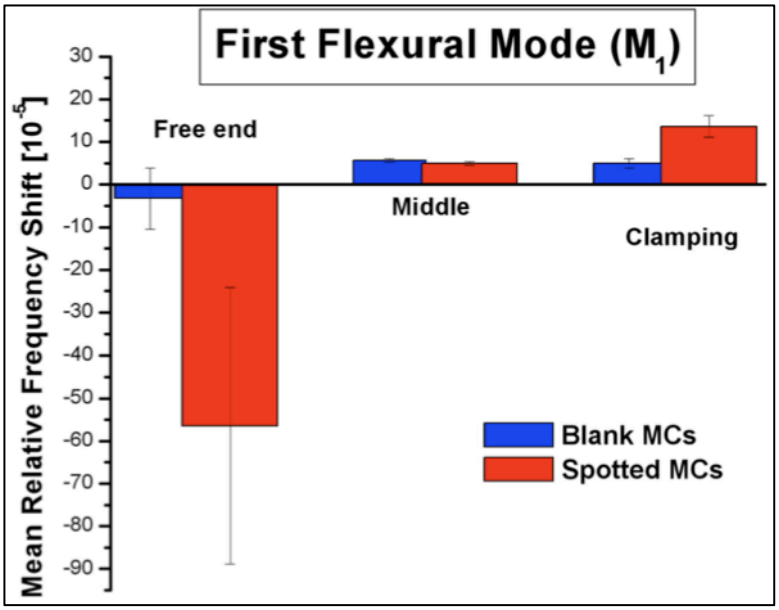
First Flexural Mode (M1)
Mean Relative Frequency Shift [10-5]
30
20
10
0
-10
-20
-30
-40
-50
-60
-70
-80
-90
Free end
Middle
Clamping
Blank MCs
Spotted MCs

b)

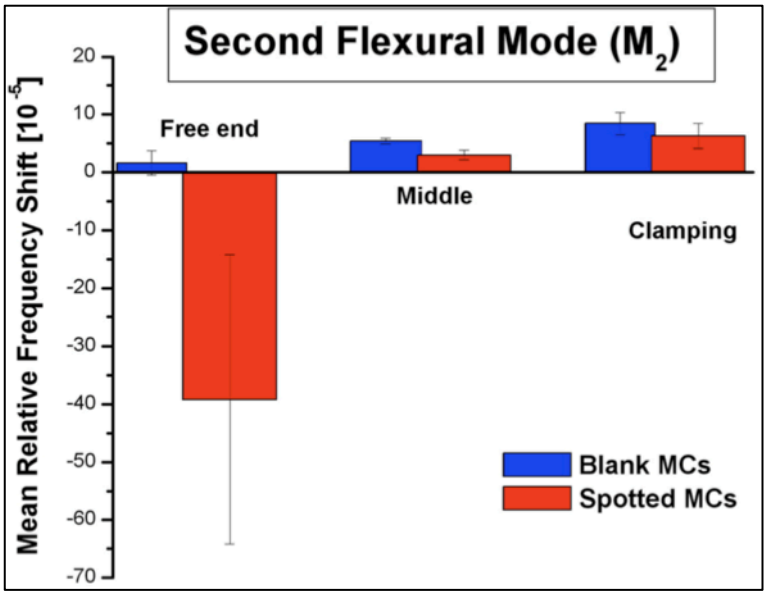
Second Flexural Mode (M2)
Mean Relative Frequency Shift [10-5]
20
10
0
-10
-20
-30
-40
-50
-60
-70
Free end
Middle
Clamping
Blank MCs
Spotted MCs

c)

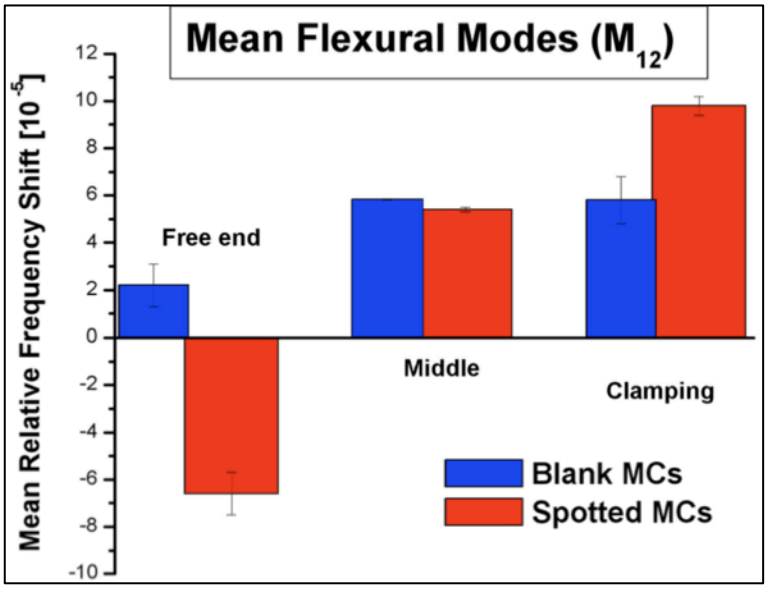

*Figure **4.8**: Frequency resonance analysis of microcantilevers measured for each droplet position: (a) with the first flexural mode (M1) and (b) with the second flexural mode (M2). In (c) is shown the mean value between M1 and M2: the main noticeable difference is when the Laminin droplet is spotted on the free end and on the clamping base of the microcantilever beam.*

If droplets are located on the oscillating end of the cantilever, where mass effects dominate, we observe a negative shift from the frequency resonance. When droplets are deposited on the clumping base, where stiffness effects are relevant, we observe a positive shift. In the central part of the cantilever length the two effects offset each other, so the whole shift is equal to zero.

4.4 Discussions and conclusions

The development of biosensors with high sensitivity and high selectivity remains of paramount importance in different fields, such as biology, healthcare, and food technology. Nanomechanical resonators have a huge potential for ultrasensitive detection of biomolecules. As described in the first paragraph, the shift of the resonance frequency induced by the adsorbed molecule onto a nanomechanical resonator arises from three effects: added mass (negative shift), mechanical stiffness (positive shift), and surface stress (either positive or negative shift). The last effect is usually the smallest of the three and it can be neglected. However, designing nanomechanical resonators with geometries and dimensions that amplify the non-linear effects of surface stress can significantly enhance it. The stiffness effect has received little attention, despite its importance and potential. Experiments and theory unequivocally teach us that the resonance frequency is a convolution of the stiffness and mass of the adsorbate. Since

both effects exhibit opposite signs, the sensitivity can be reduced and the mass underestimated. There are different methods that turn this apparent disadvantage into a striking unique asset, enabling the simultaneous measurement of the mass and stiffness induced by the biomolecular interaction on the resonator surface [7].

We tuned one strategy to achieve this goal using Laser Assisted Bioprinting for functionalizing microcantilevers with single droplets of Laminin on three different positions along the beam length. We have demonstrated that, by using arrays of ultrathin cantilevers with confining sensing regions alternately placed at the free end, in the middle and the fixed end (Fig. 4.6), a threefold signature of the adsorbed molecules can be obtained: the added mass reported by the cantilevers with the droplet at the tip, the nanoscale elasticity reported by the cantilevers with the droplet at the clamp and the surface stress reported by the cantilevers with the droplet positioned in the middle.

Laminin, the spotted molecule, is the most important protein for cells and also bacteria adhesion; Laminin droplets area act as sensing regions as they can recognize a specific anti-Laminin antibody fluorescent-conjugated as shown in Chapter 3 of this thesis, Figure 3.1.

A deeper understanding and a better localization could be carried out using more oscillating modes and changing the protein concentration.

The improvement of LAB in the biosensor microcantilever-based field is an important novelty that will provide a real-time measurement with high sensitivity of both mass and frequency

Furthermore theoretical and experimental developments are still required in order to elucidate the intermolecular interactions responsible of the flexural rigidity variation due to the adsorption of biomolecule monolayers. However, the results suggest that the combination of nanomechanical resonators with different geometries that make them sensitive to different properties of the adsorbates is a promising route for ultrasensitive and specific detection of biological targets.

Materials and Methods

Bioink-Ribbon preparation.
Laser Assisted Bioprinting
(see Materials and Methods in Chapter 3)

Microcantilevers fabrication

Microcantilever arrays fabrication, together with Frequency Resonance Analysis described in the following paragraph, has been entirely performed by the work group of Prof. Fabrizio Pirri and Dott. Carlo Ricciardi from Politecnico of Torino (Applied Science and Technology Dep).
Microcantilever arrays have planar dimensions of 7 mm x 7 mm and are composed by 11 microcantilevers each. Microcantilever arrays used in this thesis work, as belonging to the family of Micro-Electro-Mechanical Systems (MEMS), were manufactured through microfabrication technology. Fabrication of a suspended microstructure, such as a cantilever transducer, consists of patterning and etching steps that define, respectively, lateral sizes and the surrounding of the microcantilever: sometimes also a deposition step could be added if a material different from the bulk is needed. The most commonly used surface micromachining process is the ***sacrificial-layer etching****. In this process, a microstructure such as a microcantilever beam is released by removing a sacrificial thin-film material, which was previously deposited underneath the microstructure. A quarter of Silicon-On-Insulator (SOI) wafer was used for microcantilever arrays fabrication. Several chips were realized on the substrate, and V-shape trenches were defined on the backside of the wafer in order to obtain initial guide for the release of the array. In the process flow the cantilevers are released through the following steps: photolithography on the back side, wet etching in buffered oxide etch (BOE) solution for the patterning of the mask layer on the back side, front side protection with a polymeric coating (ProTEKR_B2®), wet etching in KOH solution, sample cleaning, photolithography on the front side of the membrane, Reactive Ion Etching (RIE) of silicon, removal of the buried oxide layer in BOE and cleaning by piranha solution (75% H_2SO_4 : 25% H_2O_2).*

Frequency Resonance Analysis

Actuation system
Piezoelectric crystals and an electronic apparatus are used to actuate and control the vibration of microcantilevers. A high frequency lock-in amplifier (HF2LI, Zurich Instruments) generates a sinusoidal signal sent to a piezoelectric disk actuator (PI Ceramic). By controlling the amplitude of the modulating signal, the amplitude of the piezo movement can be controlled. The piezoelectric disk is 300 μm thin, 56 mm in diameter and it is made of lead zirconium titanate (PZT). Since the disk frontal dimensions are much greater compared to its thickness, the acquired vibration remains directed mainly along

the z direction and no lateral vibrations are present. The disk presents a nickel/copper metallization on both sides. The bottom side of the disk was attached to a Peltier element by means of thermal-conductive glue. The actuation system is able to put in vibration the microcantilever arrays when excited by a voltage at a definite frequency. Consequently, microcantilevers vibrate at the same frequency of the excitation input. Moreover, exploiting a frequency scan to the piezo disk, microcantilevers are let oscillate around their resonance frequency by monitoring its oscillation amplitude. The sample holder is placed onto the actuator and the microcantilever arrays are attached using a double-sided tape, to guarantee a proper propagation of mechanical vibration.

Readout system

The readout system of the instrument is based on the so-called "optical lever method". A laser diode (by AMS Technologies) beam has to be focused onto the plane of the sensor array, precisely on the tip of the microcantilever, with the aim of detecting the resonator oscillation. The light source has to have a good stability during time and a low power density to prevent an excessive heating of the sample. Using low power laser (minimum light spot focalization) the thermal induced noise can be neglected (especially for cantilever on the micrometer scale, while for nano-cantilever the thermal noise becomes meaningful). An optical microscope (magnification 50x) is focused on the cantilever surface, to control the laser spot positioning on the free end of the beam. An optical lens system collimates the light reflected by the cantilever and focuses it on the small area of the Position Sensitive Diode (PSD – by Edmund Optics), exploited because of its high speed (very low rise time) for high frequency characterizations. The incident light is so translated in a photocurrent, collected on the two lateral electrodes. The amount of charge collected at each electrode is inversely proportional to the distance between the electrode and the hitting point of the detector light spot.

The power of the incident light and shape-dimension of the light spot don't influence the differential result. It is clear that such kind of photodiode can only detect a dynamic light signal, because is the position divergence of the light spot that gives the differential variation of the charge collected at the electrodes. Thus, this kind of detection system allows only an evaluation of the vibration shape. The output signal of the PSD is then amplified and filtered through the lock-in, and it is finally stored in a PC. An automated 2D scanning system composed by two actuators (by Physik Instrumente GmbH & Co) has been employed for achieving a fast serial characterization of all resonators: their 100 mm travel range allows a scan of a large area, leading to the advantage of sequentially measuring several array chips, with a speed up to 10 mm/s, high resolution (0.25 μm) and repeatability (1 μm) which assure a fast and accurate scan.

Data collection, filtering and storage

The PSD detector collects the signal related to the movement of the cantilever, but also every other moving light (such as the ambient environment surrounding light) adds a new element on the detectable signal. Furthermore, generic low frequency mechanical vibrations of the structure on which the system is attached, especially thermal noise,

influence the final signal. The pure output of the photodiode is thus very noisy and a signal filtering is requested: at this purpose, a lock-in amplifier is used. It works as a narrow band pass filter, centered on an input main frequency (which corresponds to the driving frequency of the piezo actuator). The output of the lock-in (HF2LI by Zurich Instruments) is proportional to the amplitude of the cantilever amplitude displacement and considers only the vibration component related to the driving frequency of the piezo vibration. The application of the lock-in filtering is very useful to analyze such noisy and weak signal as the ones revealed by the photo-detector. The electronic chain (the lock-in amplifier plus the function generator) is controlled by a Labview® codified program. The program allows to set up automatic measurement up to nine arrays of microcantilever, controlling the range of the frequency scan, the main acquisition parameters and to store data on a pc.

Vacuum system

The vacuum system is constituted by a vacuum chamber displaced by a series of a membrane and turbo molecular pumps (MINI-Task System, Varian Inc. Vacuum Technologies). The customized chamber is an aluminum empty cylinder (internal diameter = 100 mm). At the center of the chamber there is a cylindrical pivot (with a diameter of 30 mm), on which a peltier element was mounted. The piezoelectric disk was locked over the peltier. The chamber was closed on the upper side by a transparent plexiglass stopper. Passing across the transparent closing system, the laser light can hit the cantilever surface, from which it is reflected towards the PSD detector. A Viton® circular o-ring is employed to avoid leakages. The membrane pump of the vacuum system supplies the primary vacuum, down to a minimum pressure of about 1 mbar. The turbo molecular pump allows reaching the maximum vacuum value of, at least, 10-5 mbar. The two pumps were connected to an interlock, which gives the opportunity to use both of them or only the primary one. The pressure conditions obtained with this method were uniform inside the chamber and stable during time.

Temperature controller

Temperature is set by using both a temperature controller (by Electron Dynamics Ltd) and a peltier element (by SuperCool): the feedback signal necessary to keep a stable temperature is obtained interfacing the Proportional Integral Derivative (PID) controller to a thermistor set in contact with the upper surface of the piezo element: temperature is kept constant with a precision of 0.01 °C.

Bibliography

[1] J. Arlett, E. Myers, and M. Roukes, “Comparative advantages of mechanical biosensors,” *Nat. Nanotechnol.*, vol. 6, pp. 203–215, 2011.

[2] B. Ilic, D. Czaplewski, M. Zalalutdinov, H. G. Craighead, P. Neuzil, C. Campagnolo, and C. Batt, “Single cell detection with micromechanical oscillators,” *J. Vac. Sci. Technol. B*, vol. 19, p. 2825, 2001.

[3] G. A. Campbell and R. Mutharasan, “Detection and quantification of proteins using selfexcite PZT-glass millimeter-sized cantilever,” *Biosens. Bioelectron.*, vol. 21, pp. 597–607, 2005.

[4] M. Su, S. Li, and V. P. Dravid, “Microcantilever resonance-based DNA detection with nanoparticle probes,” *Appl. Phys. Lett.*, vol. 82, no. 20, pp. 3562–3564, 2003.

[5] K. Y. Gfeller, N. Nugaeva, and M. Hegner, “Micromechanical oscillators as rapid biosensor for the detection of active growth of Escherichia coli.,” *Biosens. Bioelectron.*, vol. 21, no. 3, pp. 528–33, Sep. 2005.

[6] A. Gupta, D. Akin, and R. Bashir, “Single virus particle mass detection using microresonators with nanoscale thickness,” *Appl. Phys. Lett.*, vol. 84, pp. 1976–1978, 2004.

[7] J. Tamayo, P. M. Kosaka, J. J. Ruz, Á. San Paulo, and M. Calleja, “Biosensors based on nanomechanical systems.,” *Chem. Soc. Rev.*, vol. 42, no. 3, pp. 1287–311, Feb. 2013.

Chapter 5 – Amphiphilic β-cyclodextrins (ACyDs) patterning

5.1 Introduction

Cyclodextrins (CDs) are cyclic oligosaccharides made of 6-8 D-glucose units well known for the ability to form host-guest inclusion complexes with a variety of substrates. Appropriate stepwise modifications of their primary and/or secondary faces lead to amphiphilic derivatives, able to self-assembling into micelles, vesicles, and nanoparticles with great potential as drug delivery systems. In 1891, for the first time, Villiers extracted 3 gr of cyclodextrins from *Bacillus amylobacter* and he expressed the composition $(C_6H_{10}O_5)_2 \cdot 3H_2O$ [1].
We can find cyclodextrins α, β, e γ that respectively have six, seven and eight sugar ring molecule (α-D-glucopyranoside units linked 1-4). Typical cyclodextrins can be topologically represented as *toroids* with the larger and the smaller openings of the toroid exposing to the solvent secondary and primary hydroxyl groups respectively. Because of this arrangement, the interior of the toroids is not hydrophobic, but considerably less hydrophilic than the aqueous environment and thus able to host other hydrophobic molecules. In contrast, the exterior is sufficiently hydrophilic to impart cyclodextrins (or their complexes) water solubility.

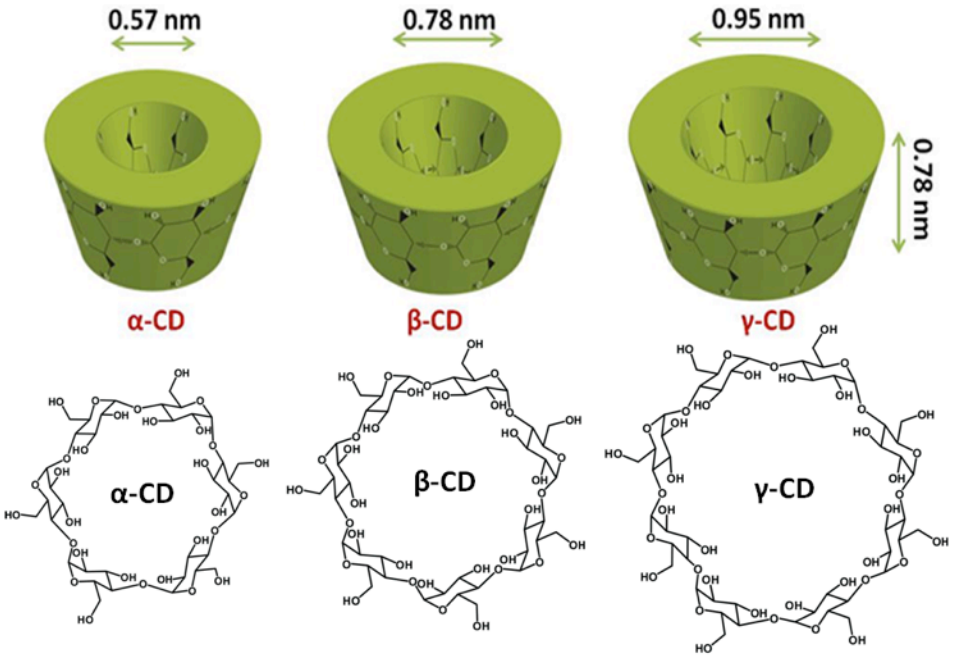

*Figure **5.1**: 3D morphology and chemical structure of the three main types of cyclodextrins.*

Cyclodextrins have a well-defined chemical structure; they have a wide range of concavities with different sizes in which it is possible to incorporate an active molecule. The main crater has an exact dimension, not changeable, that makes the CD competitive for recognizing molecules (see Figure 5.1). The formation of the inclusion compounds greatly modifies the physical and chemical properties of the guest molecule, mostly in terms of water solubility. This is the reason why cyclodextrins have attracted a large interest in many fields. For instance [2] inclusion compounds of cyclodextrins with hydrophobic molecules are able to penetrate body tissues and thus can be used to release biologically active compounds under specific conditions.

This chapter of my PhD thesis is related to the work performed in the frame of a research project called ICS (Intelligent Cell Surfaces) that is part of the European program ESF EUROCORE EuroBioSAS (bio-inspired Engineering of Sensors, Actuators & Systems), in collaboration with CNR-ISMN U.O.S. Palermo.

The aim of the ICS project is the synthesis of various amphiphilic β-Cyclodextrins to be used as chemical cues for cells to guide their adhesion and proliferation. ACyD supramolecular assemblies (vesicles, micelles) are building blocks for ultra-thin layers as they can be fused on surface by tuning surface tension. Specific objectives of the project were (i) mimicking the *in vivo* environment by integrating different stimuli; (II) monitoring cell behavior in-situ by a combination of local probes; (iii) establishing quantitative correlations between external stimuli and cell behavior (in terms of motility, adhesion, self-aggregation, functionality, and differentiation).

5.2 β-Cyclodextrins ($SC16NH_2$) surface patterning

Our project partner provided us ACyD using the method described in the Materials and Methods section [3][4]. The complexes of ACyD with FITC were then used as molecular cues for patterning surfaces for cell culture. This was one of the main steps of the ICS project that was aiming at fabricating smart surfaces for controlling cell fate combining unconventional lithographic techniques with solutions of *ad hoc* tailored ACyD. The strategy that has been followed is herein illustrated.

First of all the patterning of ACyD by Lithographically Controlled Wetting was investigated as a possible fabrication technique; in parallel the effect of ACyD, both supplied in solution or previously deposited onto a surface, on the chosen cell lines (SH-SY5Y) was assessed. Finally SHSY5Y cells were cultured onto patterned substrates.

The characterization was done mainly by microscopy techniques, ranging from the high resolution Atomic Force Microscopy and Scanning Electron Microscopy for imaging the patterned features to the immunofluorescence assays for assessing the cell behavior.

The ACyD $SC16NH_2$ (Figure **5.2**) has been patterned on surfaces suitable for the cell cultures to achieve good cell guidance and sorting.

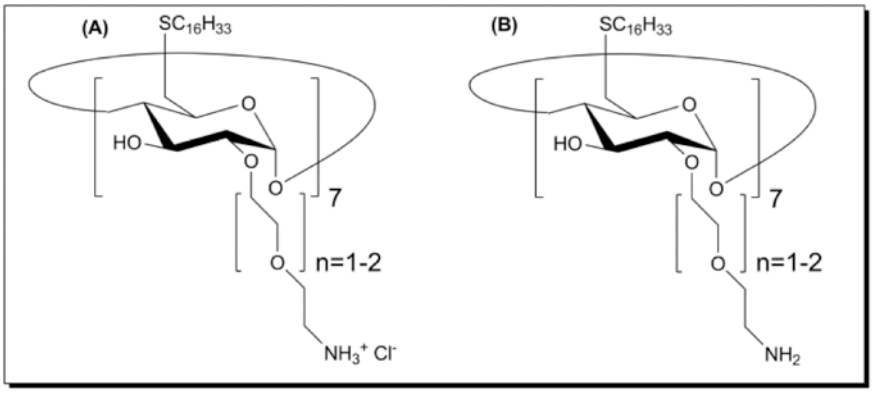

*Figure **5.2**: Cyclodextrin SC16NH2 plausibly present at pH ≤8 as protonated form (A) and in neutral form (B) at pH ≥8.*

The first method applied to ACyD patterning has been Lithographically Controlled Wetting (LCW). This technique is based on the controlled formation of the menisci of a solution tethered between the surface to be functionalized and the patterning stamp, as shown in Chapter 2. The solute is deposited where the solution has been pinned thus reproducing the pattern present in the stamp; LCW is highly versatile because it can use a wide range of templating stamps: soft and hard polymers and metals. In Figure **5.3** the first results obtained in the frame of the ICS project by LCW are reported. In particular one can see that using a metallic hexagonal copper grid a cell culture dish can be functionalized with the same pattern over a macroscopic scale; the Atomic Force Microscope (AFM) (Fig. **5.3**b) and Scanning Electron Microscope (SEM) (Fig. **5.3**c, **5.3**d) reported are important to get high resolution information about the fabricated pattern, in particular in figure 5.3d the ACyD vesicles are visible along the patterned part of the surface.

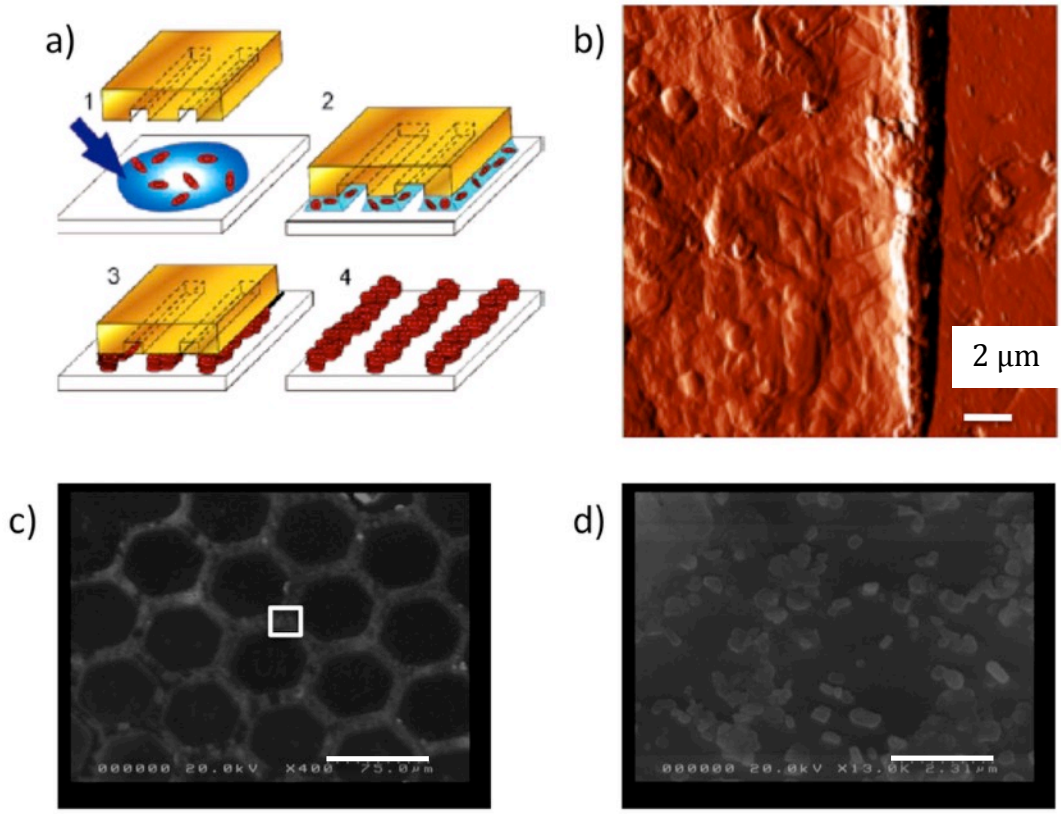

*Figure **5.3**: ACyD patterned by Lithographically Controlled Wetting (LCW) using a hexagonal copper grid as stamp. In (a) a schematic description of the LCW process is reported. In (b) one can see an AFM image of the surface right on the edge of the pattern (c) and (d) show two different magnifications of the same pattern using SEM, in the first the pattern can be seen, while in the second the ACyD vesicles are evident. Scale bar is 75µm in (c) and 2,5µm in (d).*
(Images from Michele Bianchi PhD Thesis, 2011 published by Springer Berlin Hidelberg).

5.3 SH-SY5Y cells and $SC16NH_2$

To study the interaction between ACyD and cells, we decided, at first, to fabricate two types of samples: in the first one, we coated a clean glass coverslip (1 h at RT) with ACyD and then cells were seeded on it (Fig **5.4**a, **5.4**b); in the second one, we performed cell seeding and then a defined volume of ACyD solution was supplied in the cell medium (Fig **5.4**c-d). A control sample of cells on bare coverslip is always done to verify cell viability (Fig. **5.4**e).

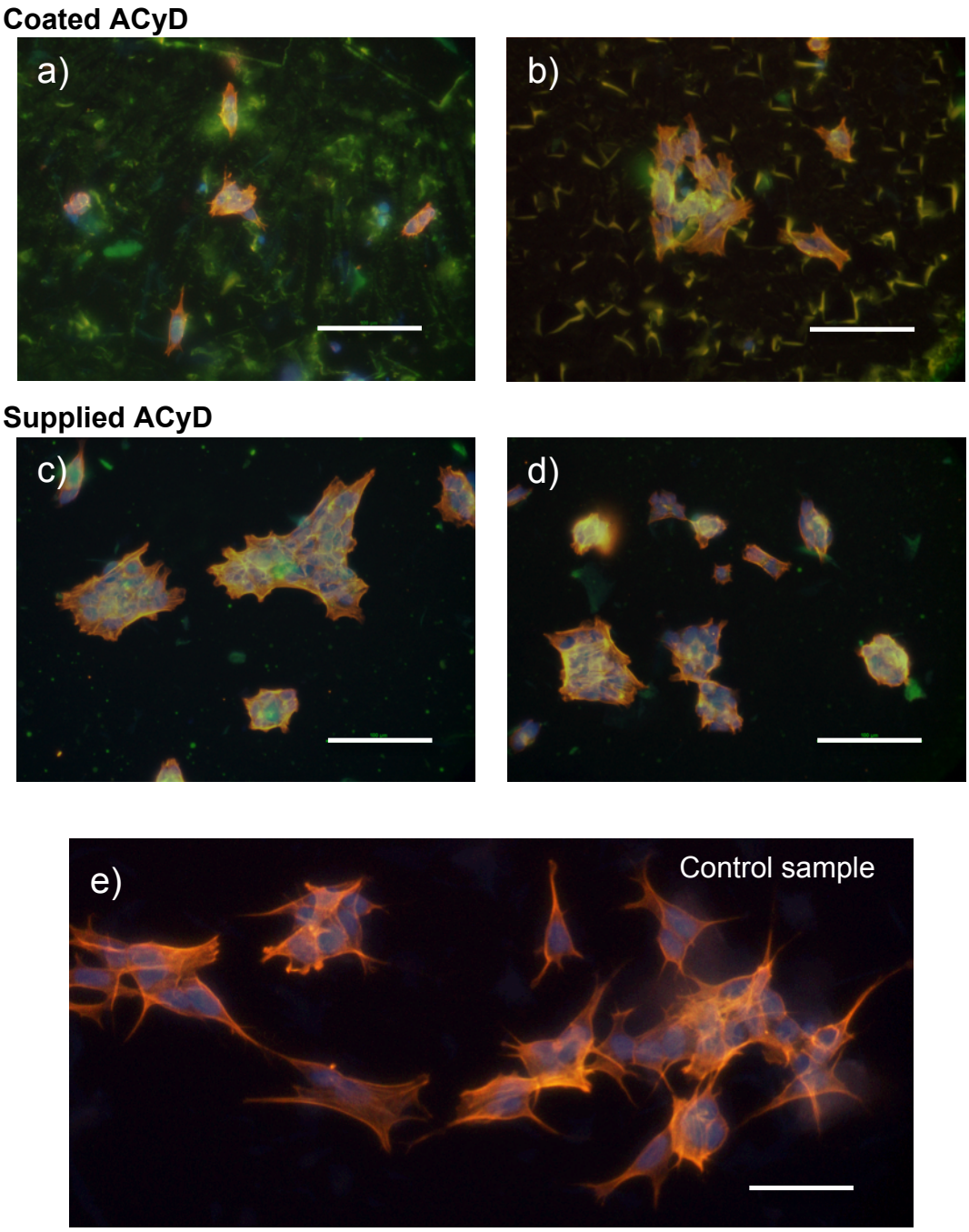

*Figure **5.4** (a,b) Coating samples show a low number of cells that adhere onto the coverslip and an unusual morphology (roundish and aggregated) compared to the control sample (e). In supplied samples (c,d) the cell number is similar to the control sample, likewise the morphology. Scale bar is 100 µm.*

These results support the idea that the presence of ACyD onto the substrate plays a role for cell adhesion. To exploit this effect for locally controlling the cell adhesion we thus patterned the ACyD using Lithographically Controlled Wetting (LCW).

LCW ACyD

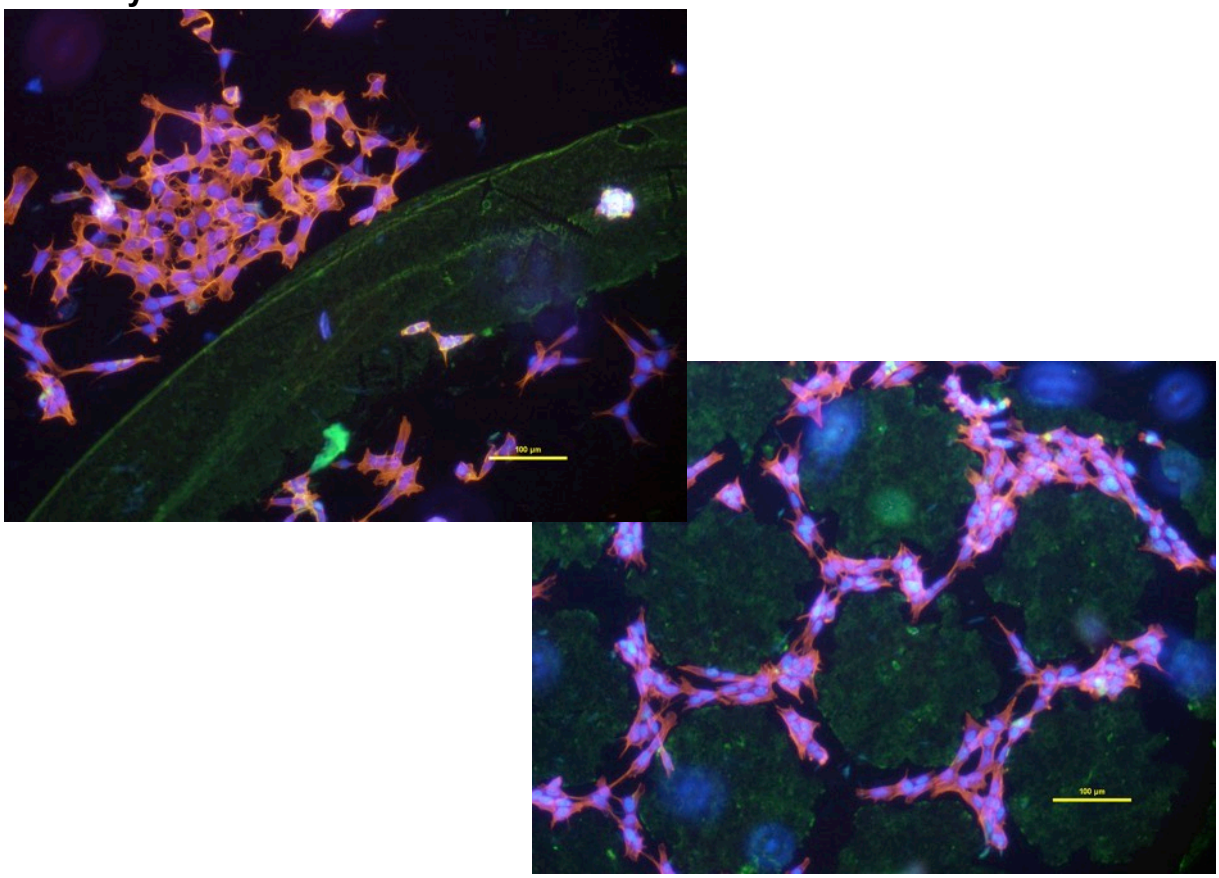

*Figure. **5.5**: LCW of ACyD revealed that cells adhered onto empty spaces between the ACyD pattern. Scale bar is 100 µm.*

In agreement with the results obtained onto the unpatterned samples, in Figure **5.5** it is possible to see that cells prefer the regions where ACyD are not present; their adhesion is prevented where ACyD are located. This is important in the perspective of using ACyD as adhesion controlling cues.

ACyD, being amphiphilic objects, assume different orientation onto the surfaces according to the surface energy of the latter. To understand whether is the orientation to play a role in controlling the cell adhesion rather than the simple ACyD presence, they were deposited onto surface with different hydrophobicity. A cleaned glass coverslip of the type used in these experiments has a contact angle of 35,4±4,2° that denotes a hydrophilic character. To further investigate this effect we changed the surface energy of the glass by an O_2 plasma treatment making the substrate more hydrophilic as shown by the water contact angles between 3,3°± 0,6° and 3,0° ± 1,4° (Figure 4); when an air plasma was used, a contact angle of 14,3° ± 4,7° was achieved). So we did the second experiment with the same set of samples, but using cleaned coverslips and cleaned coverslips after 1' of O_2 plasma treatment.

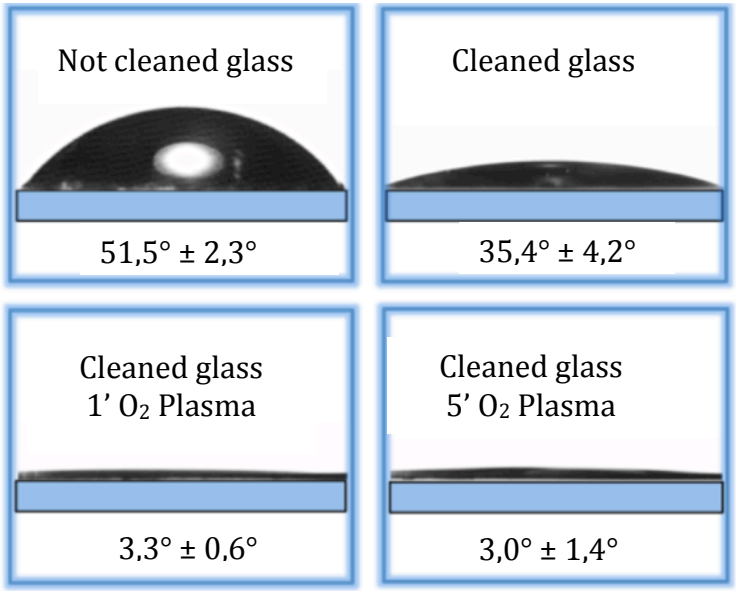

*Figure **5.6**: Glass contact angle measurements after chemical cleaning steps (images overhead) and after 1' and 5' of O_2 plasma treatment (images below).*

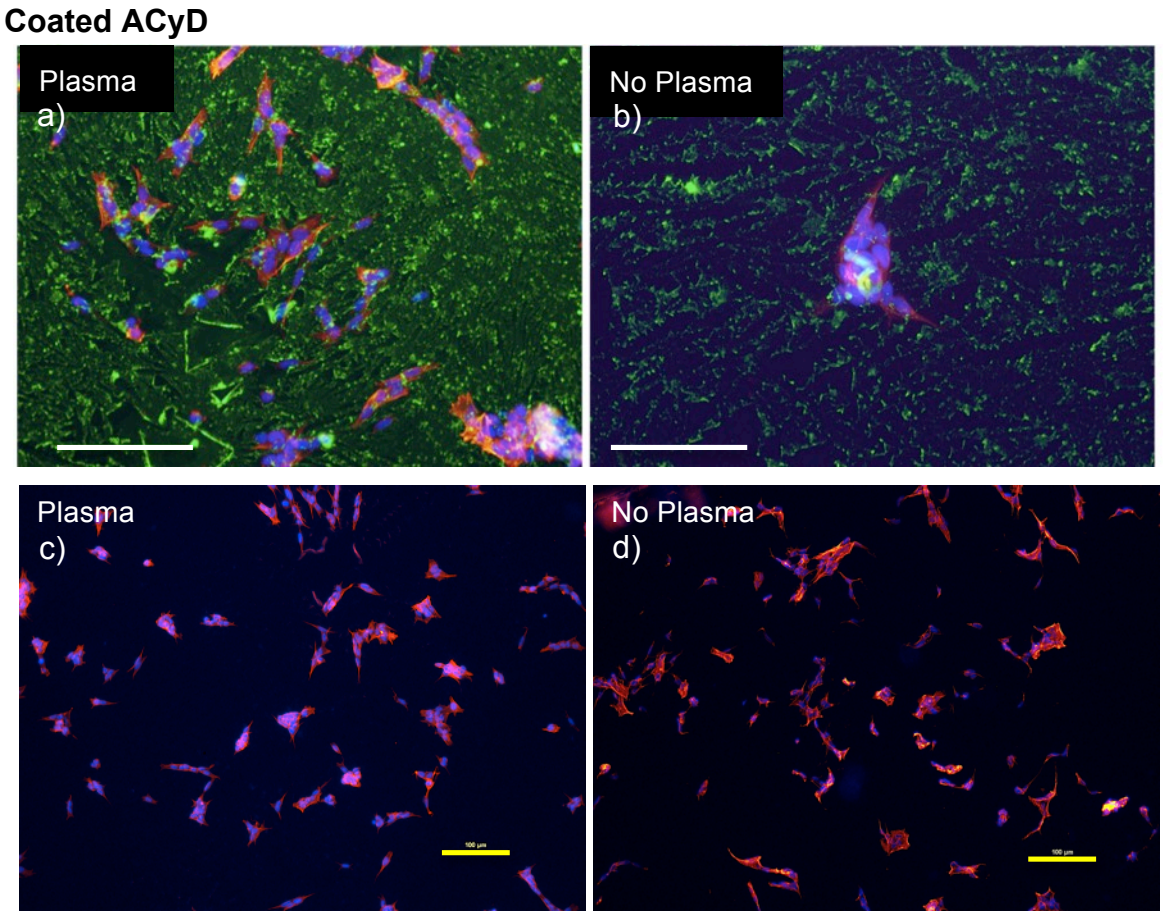

*Figure **5.7**: Cells in (a) are seeded onto sample coated after O_2 plasma treatment; they are completely different in shape and number compared to the image in (b), that refers to a coating sample without plasma treatment. Scale bar is 100 µm.*

Cells in (c) and (d) are equivalent to (a) and (b) but ACyD were not loaded with FITC. They are almost identical with or without plasma treatment. Scale bar is 100 µm.

LCW of ACyD

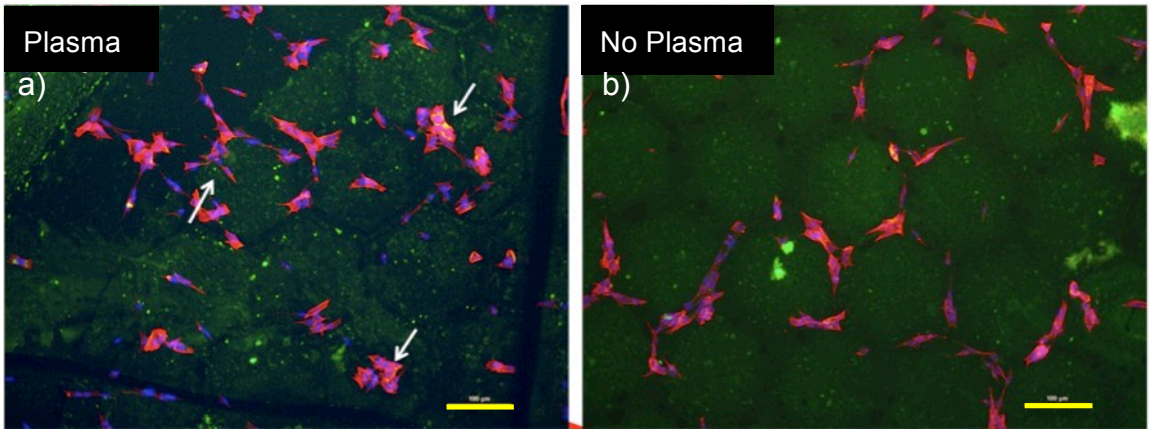

*Figure **5.8**: LCW results: (a) after plasma treatment cells adhere also in the patterned zone (see white arrows); in (b) cells are confined in the spaces between the ACyD pattern. Scale bar is 100µm.*

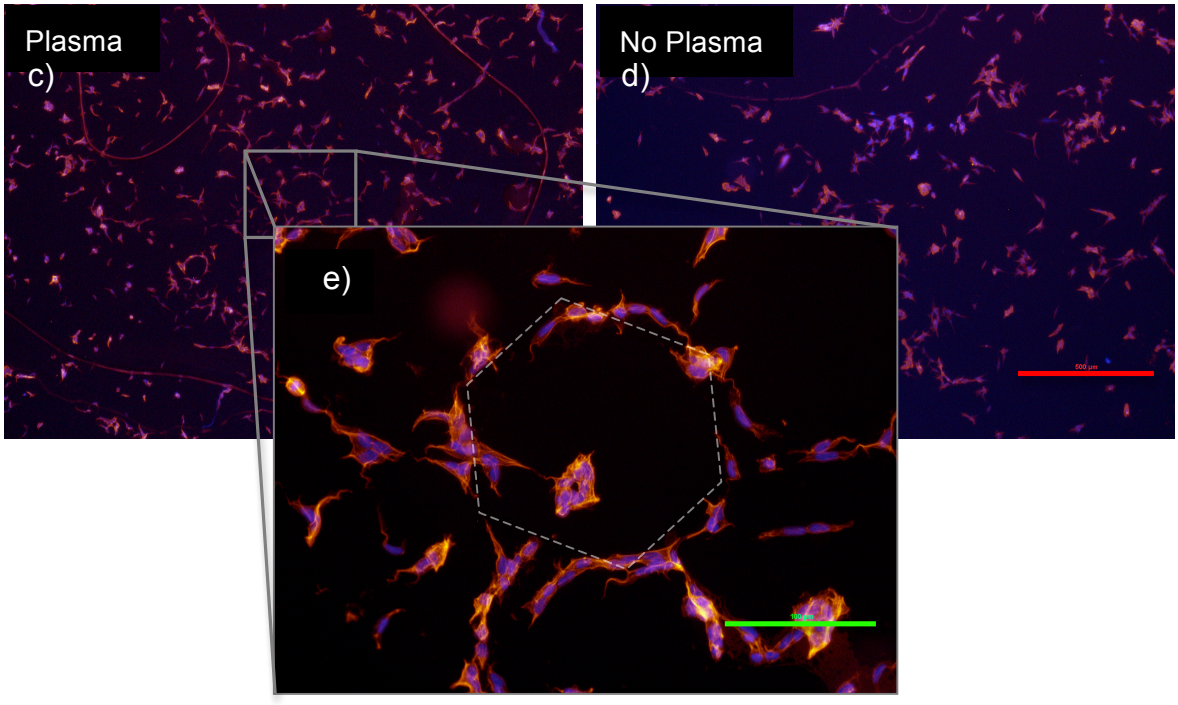

In (c) and (d) (without FITC filter merge) samples are comparable to each other as seen in Figure 5.7 for coated samples. Red scale is 500 µm. In (e) an enlargement of LCW is reported. Green scale is 100 µm.

The change of surface tension seems to influence the binding and orientation of the ACyDs onto the glass; this lead to a different cell confinement achieved by the patterned

ACyD according to the different substrate hydrophobicity. When the surface is untreated, the cells avoid the areas where ACyD are present, conversely, when the hydrophilicity is increased, cells adhered both on the covered and onto the empty features of the pattern.
We performed also the in liquid delivery of ACyD after 5' of cell seeding, on glasses with and without plasma treatment. In this case it has been necessary to exclusively use ACyD+FITC to 'see' and understand the results.

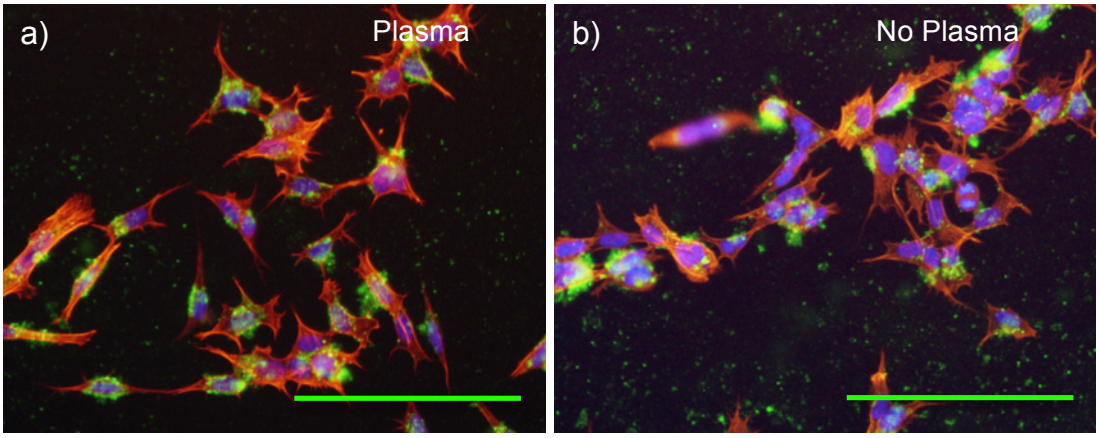

*Figure **5.9:** No difference has been noticed in the two types of samples: in both cases, cells uptake the molecule showing the fluorescence inside the cytoplasm. Scale bar is 100 µm.*

The numerical analysis revealed a higher amount of cells in the sample *coated* with ACyD upon plasma treatment compared to the one without plasma treatment; this effect can be monitored in detail by fluorescence microscopy, thanks to the combination of ACyD with FITC.

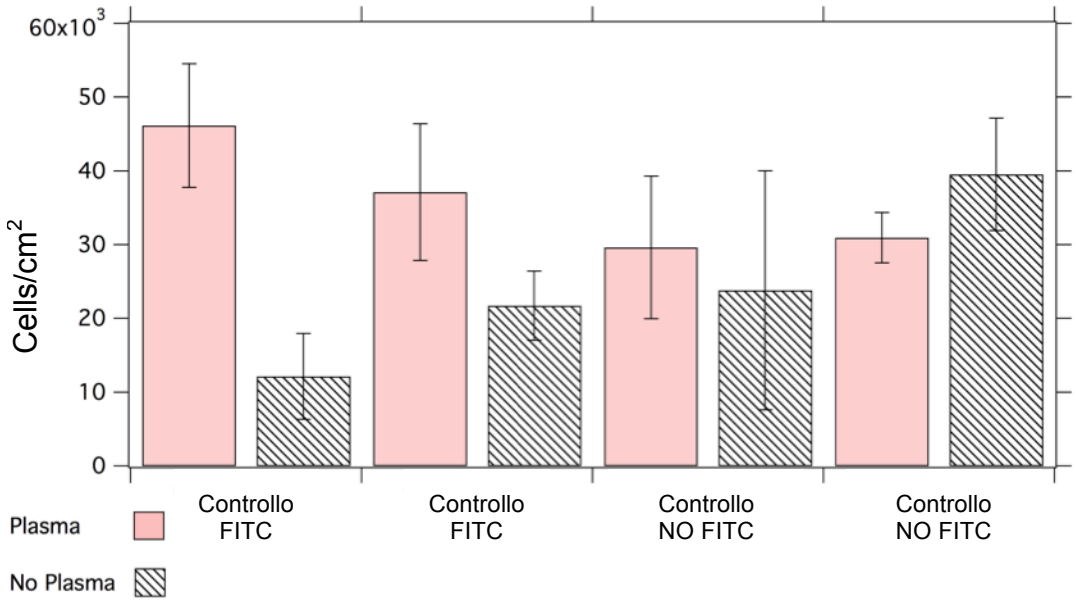

*Figure **5.10**: Comparison of the number of cells adhered onto glasses coated by ACyD±FITC both upon plasma treatment (pink columns) and not (B&W stripes columns).*

To better understand and verify our observations, we used PDMS (Polydimethylsiloxane) as a very hydrophobic material (contact angle higher than 100°) to see how it affects the ACyD coating. We made the coating with ACyD+FITC in the middle of the PDMS surface (the drop was restricted to a small area, due to the high hydrophobicity) and then we observed cell behavior.
As we expected, very few cells grown in the ACyD+FITC *coating* zone (Figure 5.11b), compared to the zone where no ACyD+FITC coating was present.

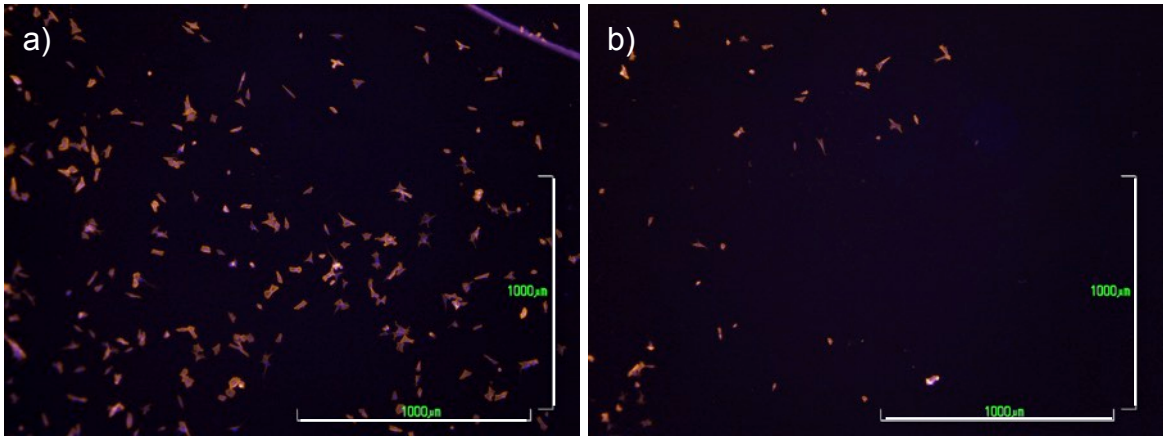

*Figure **5.11**: The image on the left refers to the PDMS area that was un-coated, while figure on the right was taken in the ACyD+FITC coating area. (FITC is not shown). Scale bar is 1000 µm.*

5.4 Discussion and conclusions

The aim of these experiments was to valuate the capability of cells to uptake AcyD patterned onto the surfaces.

We can say that ACyD+FITC orientation is crucial for cell adhesion on the surfaces. The most significant difference is related to the surface tension of the substrate that we use for the coating. On hydrophilic surfaces, ACyD+FITC positioning does not influence cell adhesion; if the surface is rather hydrophobic, cells prefer to avoid the cyclodextrins rich areas and adhere in regions where they are not present.

LCW patterning supported this evidence. In samples where LCW was performed on glass coverslips 'cleaned' by plasma treatment, cell adhesion occurred also in the patterned areas, otherwise, if the coverslip doesn't receive any plasma treatment, cells adhere exclusively in the areas deprived of ACyD.

When ACyD+FITC solution was directly supplied in culture medium, cells were obviously not affected in their adhesion behavior, they achieved an uptake of the cyclodextrins and therefore of the fluorescent molecule complexed to ACyD is delivered in the cytoplasm.

Our hypothesis is that these differences in cell adhesion not only depend on the hydrophilic/hydrophobic of the substrates, but it also largely depends on the presence of FITC molecule conjugated to ACyD. Pilot tests were made coating ACyD without FITC on coverslip (both 'cleaned' and not with plasma treatment) and performing cell seeding: in this preliminary attempts no differences in cell number on the two samples was observed. This is a first clue that perhaps FITC conjugation influences the interaction with the surfaces displaying different surface tensions. The orientation of the ACyD is then affecting cellular adhesion because, depending on the exposed side, cells will find on the surface a polyethylene glycol chain or an alkyl one that are known to have different antifouling behavior.

Materials and Methods

Synthesis of novel ACyD

ACyDs are obtained by covalent grafting of a hydrophobic group (alkyl chain) and a hydrophilic group (polyethylene glycol chain -PEG-) respectively on the narrow and wide rims of the CD cavity. Furthermore, the presence of various terminal groups (NH_2 for attractive, OH repulsive, sugar for specific interactions) allows specific recognition useful for sensor, materials engineering and biological applications.
With this in mind, a novel ACyD ($SC16NH_2$), with one –NH_2 ending on one of the PEG chains, able to form a covalent shell on gold/silver surfaces has been prepared. The PEG amination of SC16OH has been realized starting from the commercial β-cyclodextrin, through a multi step synthesis. The step-by-step synthetic procedure is reported in Scheme 1. The detailed description is reported in the electronic supplementary information (ESI) available online of [5].

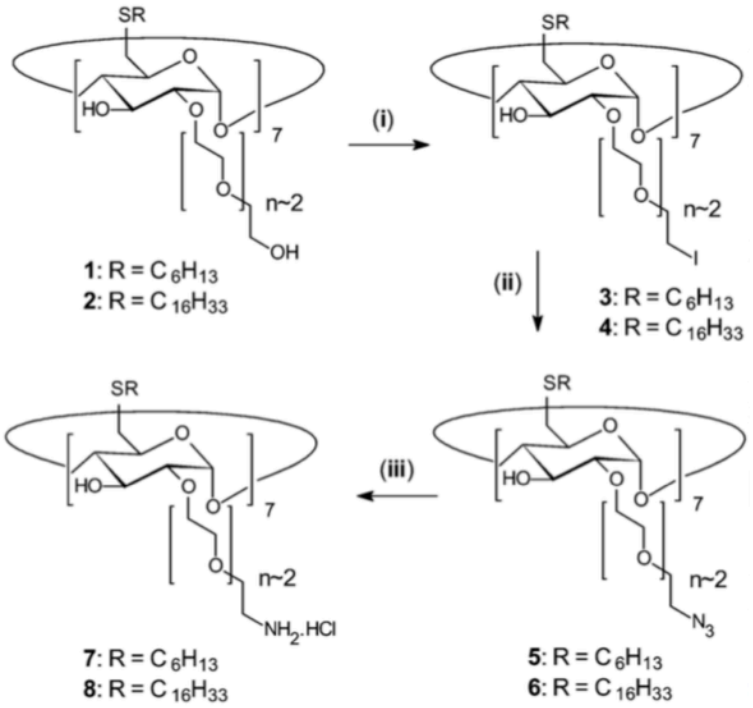

Scheme 1*: ACyDs multi-step synthesis.*

$SC16NH_2$ solution preparation

$SC16NH_2$ ACyDs are brought to us as a thin film in glass vials. From the ACyD molecular weight (3683,5 g/mol) and the amount in milligrams (3mg), we can calculate the initial concentration and then, after dissolution of the entire film in CH_2Cl_2, we can take a certain volume that contains the desired quantity of ACyD in mg. After evaporation of chlorinated solvent, we suspend ACyD in physiological solution NaCl 0,9% 'till the final concentration of

120mM (5h in sonication at 50°C). Complexes of FITC/ $SC16NH_2$ were prepared at 1:20 molar ratio by hydratation of ACyD organic film with FITC solution.

Cell culture and characterization

Human SH-SY5Y neuroblastoma cells (purchased from European Collection of Cell Cultures, ECACC, Salisbury, UK) maintenance was carried out according to the published protocol. The cells were seeded at 7500 cells per cm^2 in a final volume of 400 mL of the complete medium (CM) (MEM (Minimum Essential Medium) and F12 (Nutrient Mixture F-12 Ham) 1:1, 15% FBS, 1% Pen-strep, 1% non-essential aminoacids and 1% L-Glutamine 200mM) and incubated under the standard cell culture conditions (37°C, 5% CO2 and 95% relative humidity). Cells were maintained under standard culture conditions and fed every 2–3 days.

LCW, coated and supplied samples preparation

Coverslip (∅ 0,8cm) were cleaned by 1h dipping in HCl 37%; 15' sonication in aceton and 15' in ethanol; UV lamp treatment over-night and sterilization in autoclave.
LCW has been performed using a copper TEM grid (Trasmission Electron Microscope) with a hexagonal motif (side of 100µm) and a drop (10µl) of $SC16NH_2$±FITC solution. Coated samples were obtained using a volume of 100µl of $SC16NH_2$±FITC solution (1h of incubation at RT). Supplied samples used the same volume (100µl) distributed in cell suspension 5' after cell seeding.

Immunostaining

Immunofluorescence of actin cytoskeleton and focal adhesions was performed with the Millipore staining kit (FAK 100), that contains fluorescent-labeled Phalloidin (TRITC-conjugated Phalloidin) to map the local orientation of actin filaments within the cell. DAPI staining for the fluorescent labeling of nuclei was carried out simultaneously.
All the images were captured using an epifluorescence microscope (Nikon Eclipse 80i) endowed with NIKON excitation band DAPI-FITC-TRITC filter set and equipped with a digital camera (Nikon-DS-Fi1).

Bibliography

[1] J. Szejtli, “Introduction and General Overview of Cyclodextrin Chemistry,” *Chem. Rev.*, vol. 98, pp. 1743–1753, 1998.

[2] F. Quaglia, L. Ostacolo, A. Mazzaglia, V. Villari, D. Zaccaria, and M. T. Sciortino, “The intracellular effects of non-ionic amphiphilic cyclodextrin nanoparticles in the delivery of anticancer drugs,” *Biomaterials*, vol. 30, pp. 374–382, 2009.

[3] A. Mazzaglia, M. L. Bondì, A. Scala, F. Zito, G. Barbieri, F. Crea, G. Vianelli, P. Mineo, T. Fiore, C. Pellerito, L. Pellerito, and M. A. Costa, “Supramolecular Assemblies Based on Complexes of Nonionic Amphiphilic Cyclodextrins and a meso -Tetra(4-sulfonatophenyl)porphine Tributyltin(IV) Derivative: Potential Nanotherapeutics against Melanoma,” *Biomacromolecules*, vol. 14, pp. 3820–3829, 2013.

[4] A. Mazzaglia, N. Angelini, R. Darcy, R. Donohue, D. Lombardo, N. Micali, M. T. Sciortino, V. Villari, and M. L. Scolaro, “Novel Heterotopic Colloids of Anionic Porphyrins Entagled in Cationic Amphiphilic Cyclodextrins: Spectroscopic Investigation and Intracellular Delivery,” *Chemistry (Easton).*, vol. 9, no. 23, pp. 5762–5769, 2003.

[5] R. Donohue, A. Mazzaglia, B. J. Ravoo, and R. Darcy, “Cationic b -cyclodextrin bilayer vesicles †,” vol. 7, pp. 2864–2865, 2002.
ESI available online http://www.rsc.org/suppdata/cc/b2/b207238f/

Chapter 6 – Microcontact Printing (μCP) patterning and surface chemical gradient of anti-fouling thiols affect cell orientation, adhesion and growth

6.1 Introduction

Multiscale topographical features act on the interfacial forces guiding the cytoskeleton deformation and assembly and the membrane receptor distribution thus governing cell adhesion, proliferation, morphology and gene expression [1]–[3]. A direct approach for the control of cell fate is based on the fabrication of neighboring surface features exhibiting opposite cell anchoring properties. Cell growth and migration can thus be guided through the creation of a pattern of antifouling regions coexisting with regions favoring cell growth.

This chapter describes a set of experiments wherein an oligo ethylene-glycol-terminated alkylthiol (HS-(CH2)11-(OCH2CH2)6-OH: **TOEG6**) was used as anti-fouling cue for perform both alignment and guiding of NIH-3T3 cells.

Thiols, also called mercaptans, are organosulfur compounds that contain a carbon-bonded sulfhydryl group (R-SH). They're widely used for their inclination to create robust chemical bonds Au-S [4]. In particular, the most renowned monolayer is made of alkylthiols adsorbed on Au surfaces on Si wafer or glass. These layers, called self-assembled monolayers (SAM) are highly ordered, with a geometrical configuration due to the Au (111) pattern that allows the S atoms to be distributed according to a very dense, hexagonal grid. Van der Waals forces between alkyl chains $(CH_2)_n$ in the upper part make the thiol layer thermodynamically stable.

Structure and properties of TOEG6 SAMs has been investigated using AFM, contact angle and mass spectroscopy; monolayer substrate functionalization can be then additionally tuned changing the group at the end of the alkyl chain.

6.2 Microcontact Printing (μCP) of TOEG6 on gold

As already described in Chapter 2, μCP is a contact technique that belongs to the soft lithography group. A silicon master, created by photolithography techniques, is used to fabricate polydimethylsiloxane (PDMS) replicas with stripes 10 μm large and 15 μm spaced. The relief patterns on the PDMS stamp print the patterns of the chosen SAM ink on the surface of a substrate, Au in our experiments (see *Materials and Methods* section for details).

In this way we have generated a pattern in which 10 μm thick *antifouling* stripes are alternated to 15 μm thick stripes. Cells (NIH-3T3) are supposed to adhere on 15 μm stripes and not along the stripes covered by the *antifouling* TOEG6. For observing cells, we performed immunofluorescence (IF) assay to detect the Phalloidin staining the cytoskeleton and the DAPI staining the nuclei; green fluorescence of the entire cell visible in Figure 6.1 is due to the inherent GFP (Green Fluorescent Protein) expressed by NIH-3T3 cells.

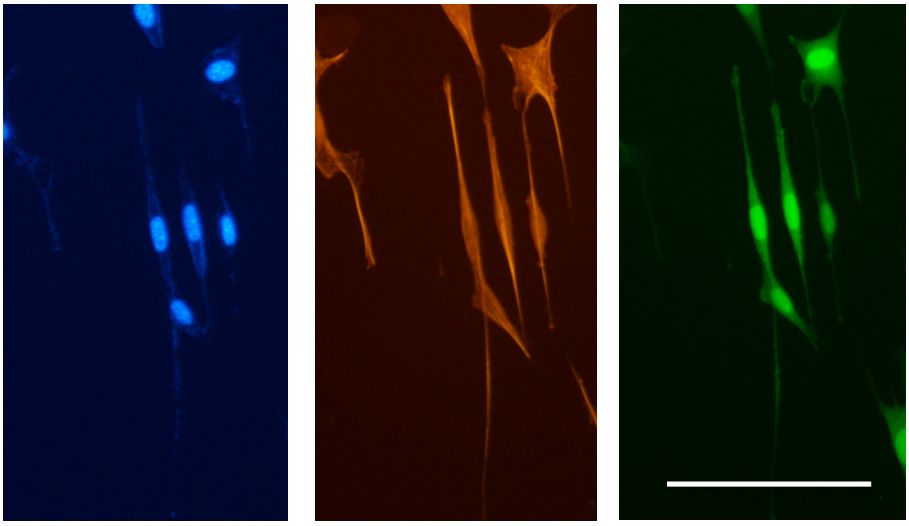

*Figure **6.1**: From left to right, DAPI staining (for nuclei), TRITC and FITC filter observation (for the entire cytoplasm) of the same three cells. NIH-3T3 cells are stretched both in the cytoplasm and nucleus. Scale bar is 100 μm.*

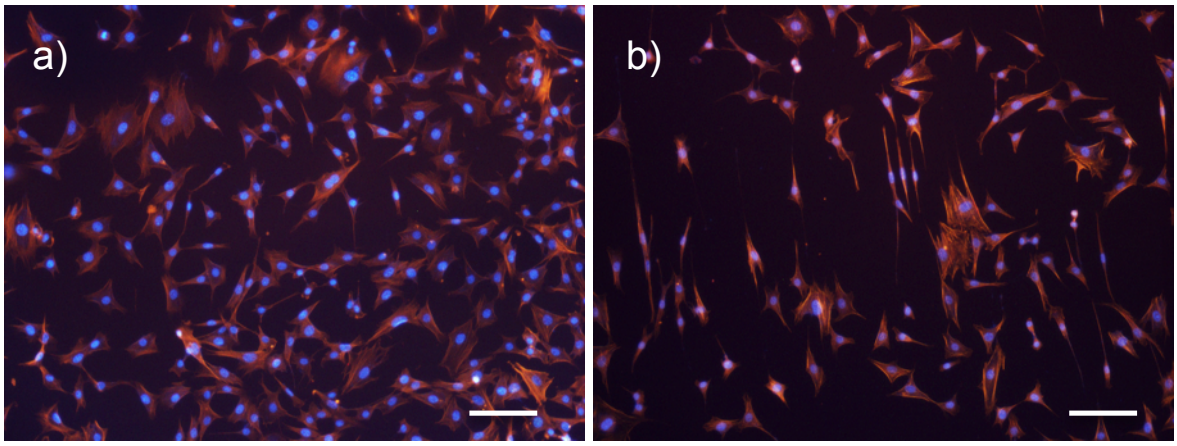

*Figure **6.2**: (a) Control sample, NIH-3T3 on bare Au surface. (b) Fibroblasts NIH-3T3 on patterned Au: we can observe many cells aligned along the stripes direction.*

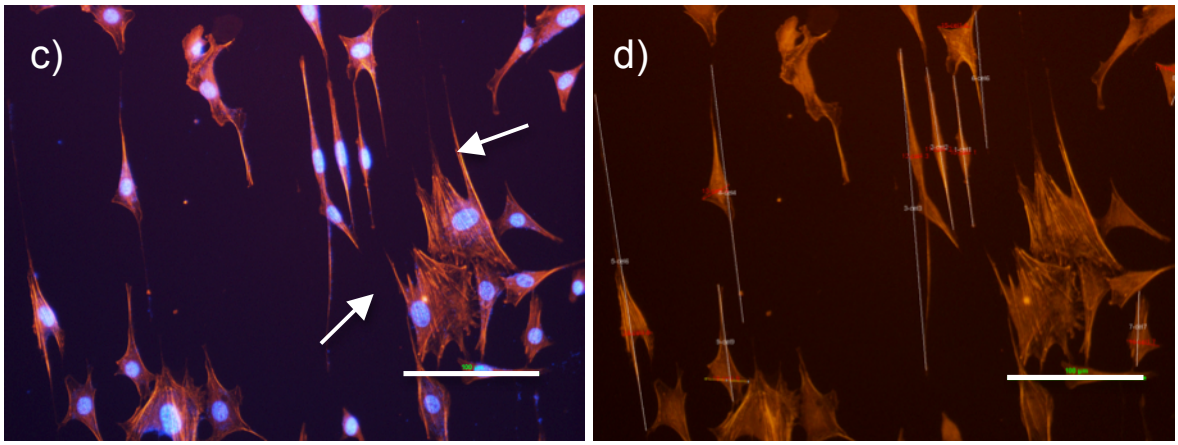

*Figure **6.2**: In a higher magnification (c) we observe how 'giant' cells (indicated by white arrows) stress the big soma sloping stripes length. Scale bar is 100 µm.*

We can clearly observe from the images that, while on control samples fibroblasts are randomly distributed, the presence of fibroblasts aligned along stripes direction prevails in the patterned samples.
Cells that adhered on *fouling* stripes stretched their cytoplasm and nucleus for better sticking on the substrate (Figure 6.2).
Following the observation of these samples with fluorescence microscopy, we performed quantitative analysis to correlate the length of the cytoplasm's and nuclei axes of aligned cells compared to those not aligned. The aim of this evaluation is to link nucleus deformation with cytoplasm alignment due to the anisotropic adhesion. We have used the ratio between difference and sum of major and minor axis of nucleus and cytoplasm as a parameter to describe the cell anisotropy as reported in the graph in Figure 6.3c-6.3g.

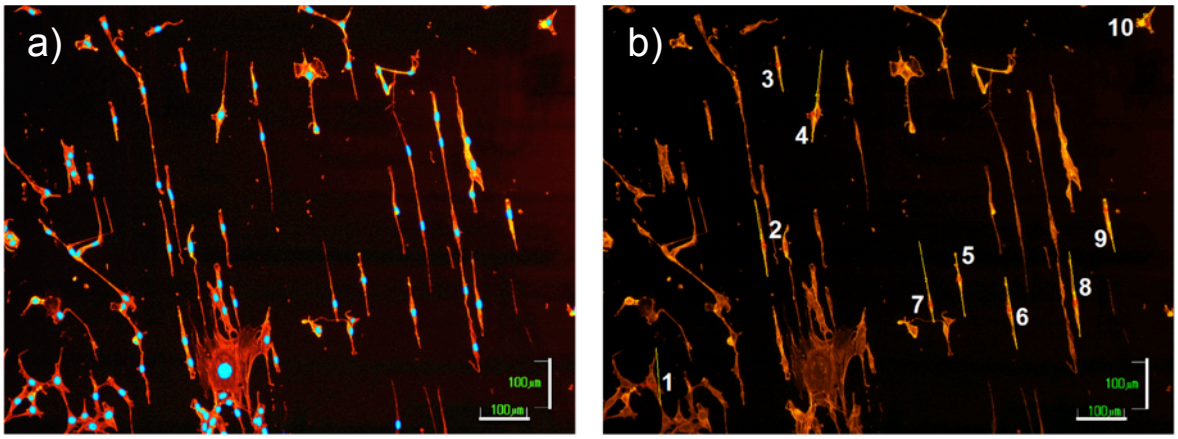

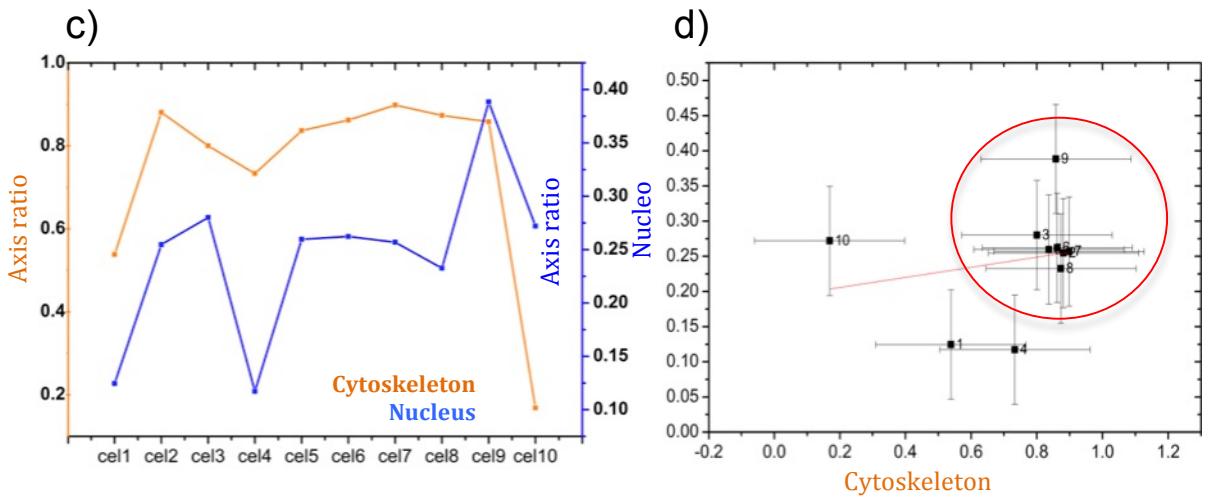

*Figure **6.3**: Analysis of major and minor axis of cytoplasm (orange) and nuclei (blue) of ten cells. Scale bar in the fluorescence images overhead is 100 µm.*
In c) is reported the ratio between difference and sum of major and minor axis of the nuclei (blue line) and cytoskeleton (orange line): the correlation between cytoplasm and nuclei elongating is noticeable if we look at the curve trend. In d) the interpolation of the data shown in c) is reported: we can notice how aligned cells are located on the same graph area (red circle).

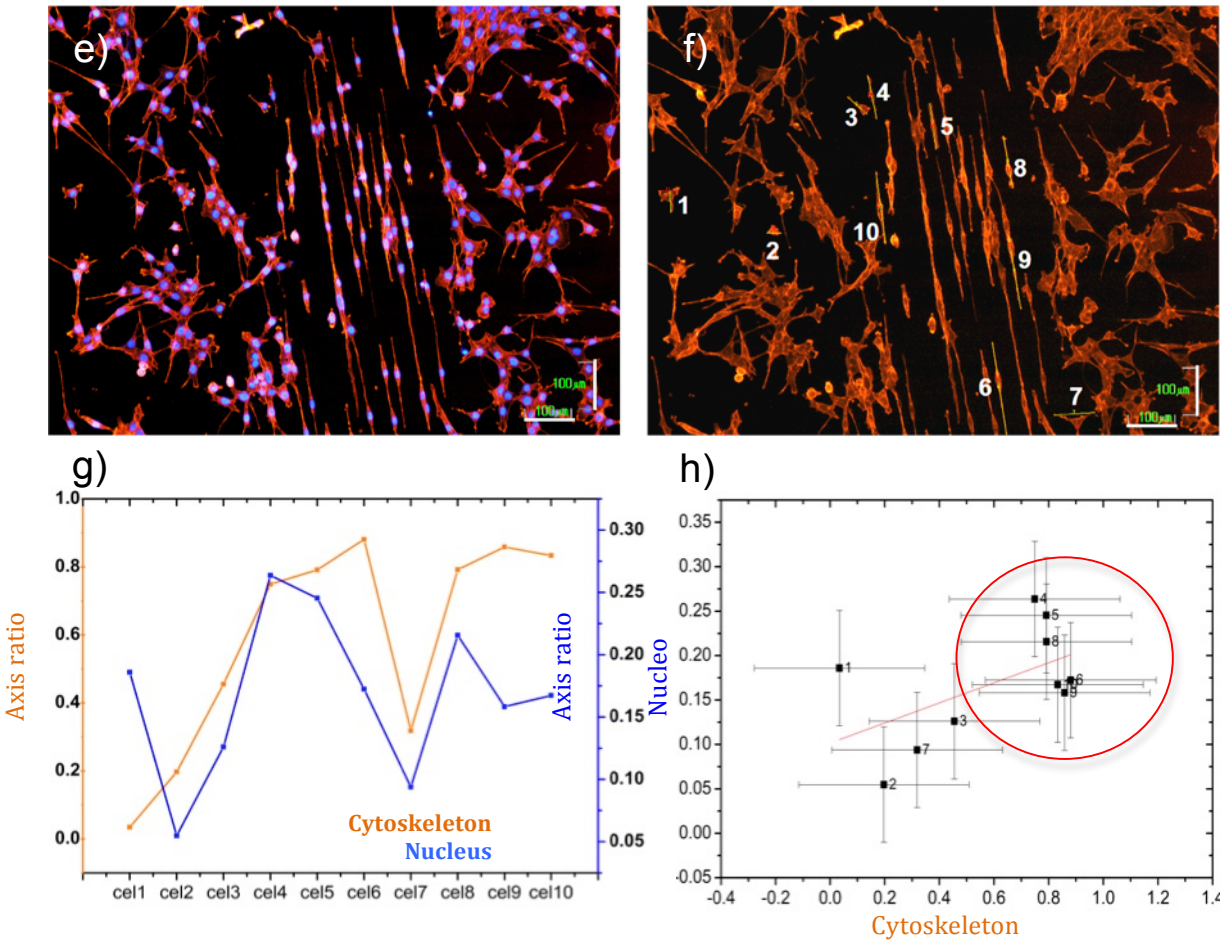

*Figure **6.3**bis: The same analysis of Fig. 6.3, but in another sample region, is here reported.*

The correlation between nucleus and cytoplasm stretching is remarkable. In the graph on the right (Fig. 6.3d, 6.3h) the correlation ratio between the 10 trials cells is even more evident: on the x we have the axial ratio of the cytoskeleton, on the y we have the same parameter for the nucleus. Doing the data interpolation from the graphs on the left, we notice that aligned cells are located on the same graph region in respect to the interpolation straight line. This observation means that for strong cytoskeleton stretching, a nucleus deformation is associated, due to the cytoplasm filaments stress.

6.3 Chemical gradient of TOEG6 on gold

Unlike the previous experiment, where cell adhesion was subjected to a discrete parameter, namely *anti-fouling* TOEG6 stripes against *fouling* gold stripes, in the forthcoming experiments cell adhesion was tuned by continuously varying surface properties. Using cyclic voltammetry (see Chapter 2), the TOEG6 SAM has been gradually desorbed from the gold layer, to obtain a chemical surface gradient running from an *anti-fouling* (complete TOEG6 SAM) to a *fouling* region (fully desorbed SAM) [5]. NIH-3T3 fibroblasts have been seeded on the TOEG6 gradients on gold evaporated both on glass and on SiO_2; a detailed protocol description is given at the end of the chapter. In Figure 6.4 a collage of serial images taken for DAPI (blue) and GFP (green) fluorescence is reported. From left to right the surface becomes gradually more suitable for cell adhesion, because on the left TOEG6 SAM is less desorbed compared to the area on the right, where the desorption of the thiol is almost fully achieved.

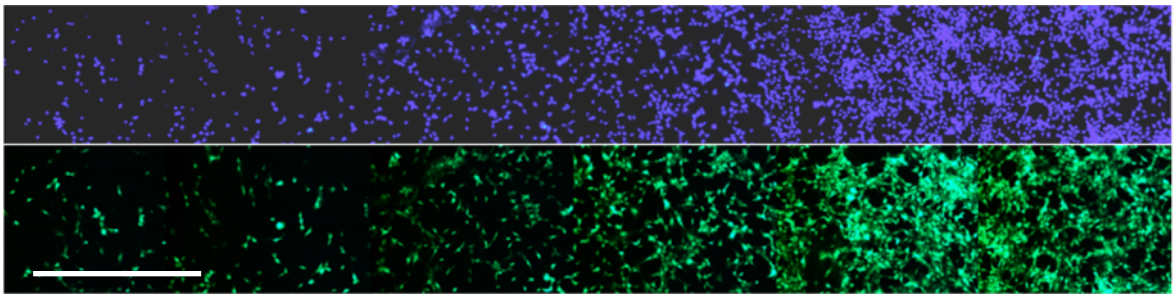

*Figure **6.4**: Collage of sequential images (7 progressive snapshots of 15 total) of NIH-3T3 cells along TOEG6 gradient, in DAPI (above) and GFP view (below). Scale bar is 1000 μm.*

The quantitative analysis involved two different procedures: in the first one, we just counted cells nuclei number (on DAPI images); in the second one we estimated the percentage of area occupied by cells soma in each image, the coverage (on GFP images). As shown in Figure 6.5, the behavior of the curves is the same for the nuclei amount (6.5a, 6.5b) and for the surface coverage (6.5c, 6.5d): cell distribution gradually rises from left to right. Cell density increases following the TOEG6 desorption grade, with few

fluctuation due to sporadic gold surface imperfections that affect SAM stability (see Figure 6.5c).

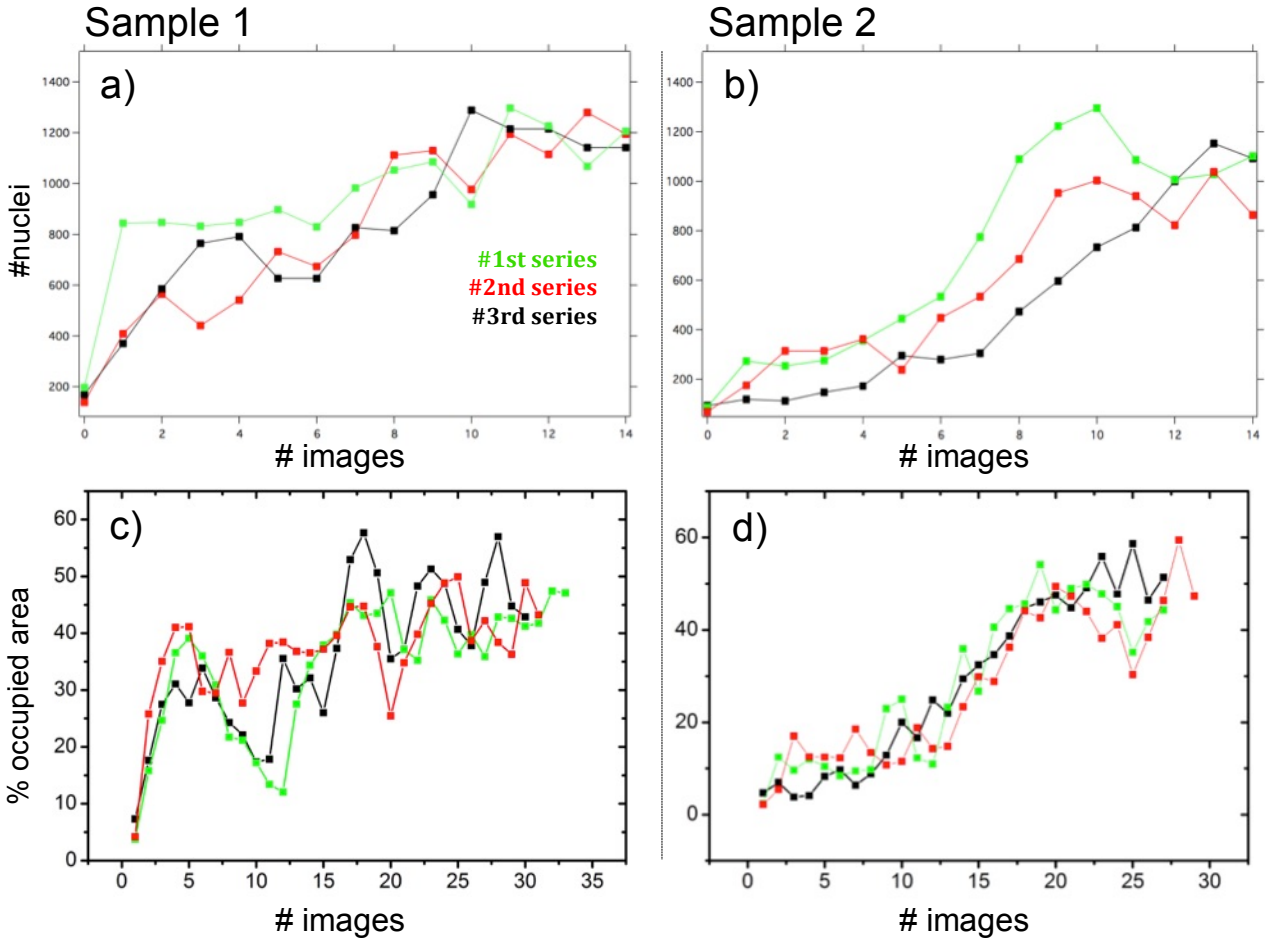

*Figure **6.5**: Quantitative analysis on cell distribution on TOEG6 gradient (two distinct samples (a-c) and (b-d) are reported). The fouling capacity grows from left to right. (a)(b) Cell nuclei counting performed on the DAPI images (14 of ≈30 total along the gradient) (curves green, red and black) along three regions parallel to each other and parallel to the gradient. (c)(d) Beneath the analysis on GFP images is reported. The % of area occupied by cells soma has been calculated for each image along the series. The trends of the curves are in good agreement.*

For this experiment, the Power Spectrum Density Function (PSDF) analysis has also been calculated, with the aim of finding some typical features.
We performed PSDF on DAPI images, which referred to the green (#1st series) and the black (#3rd series) curves of the sample 2, shown in Figure 6.5b-d: we found two characteristic lengths.
PSD is the norm square of the Fourier transform of the image. From it the characteristic lengths of the image (ξ = correlation length) can be extracted and then quantitatively correlated with the morphological details present in the different images and samples. The analysis of the PSD is a robust method that provides a quantitative measure of the

spatial distribution of cells. It is also a versatile method because it can be applied to images obtained by any microscopy techniques, such as scanning electron microscopy, fluorescence microscopy or atomic force microscopy.

The analysis of the PSD allows exploring a wide range of frequencies between ν_{MIN} = (1/L) where L is the size of the image and ν_{MAX} = (N/2L) where N is the number of pixels of the image. In order to carry out a consistent PSD based analysis it is important to capture images of the same size and resolution to always have the same information in terms of frequencies displayed by the PSD plots.

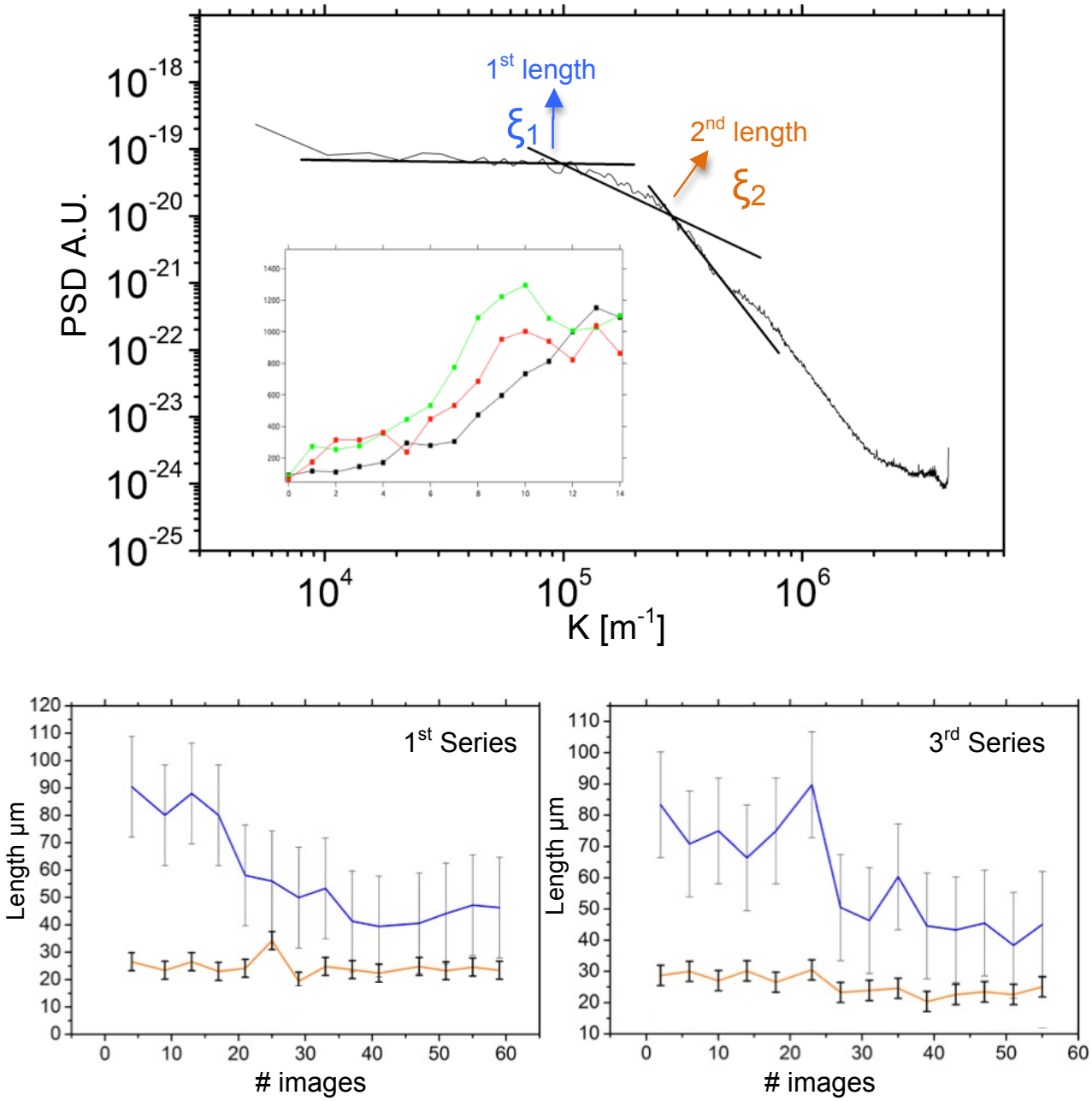

*Figure **6.6**: (a) Power spectral density vs wave vector **k** of two images series (1st and 3rd series in the small pic below) showed two characteristic lengths. In b) and c) graphs the development of the features along the gradient for each series is reported.*

The PSDF plot has been performed on all the DAPI images of fibroblast along the TOEG6 gradient. The one in Figure 6.6a is an example in which two characteristic lengths (ξ_1 and ξ_2) has been manually extracted from the curve. A change of slope in the curve, in fact, matches with a typical feature that can be calculated by using this equation:

$$\xi = 2\pi/k$$

where k is the spatial frequency [m^{-1}] on the x axis.
In Figure 6.6b and 6.6c are displayed the progressions of the wholly average values for ξ_1 and ξ_2, with the corresponding error (standard deviation), estimated for all the DAPI images PSDF. The blue curve denotes a feature (ξ_1) that progressively decreases lengthways the gradient, definitely corresponding to the spacing between the nuclei. This result contributes to strengthen the power of the TOEG6 gradient in directing cell adhesion along the functionalized surface. Finally, the pink curve (ξ_2), constant at the value of 15 μm, is the measure of the nuclei width.

6.4 Discussions and conclusions

The activity presented in this chapter has been dealing with the ability to tune the adhesion of cells onto different surfaces. Two parallel strategies have been followed, both involving the functionalization of gold surfaces by mean of alkylthiol: the first one, based on a soft lithography approach, has produced sharp changes in the adhesion propensity of the surface and thus a strong alignment and deformation of the cell shape; the second one, based on the electrochemical desorption, has allowed the fabrication of smooth gradients of antifouling molecules able to control the local density and migration of the cells.
In the first strategy Microcontact Printing, a broadly diffuse technique for its ease of execution and cheapness, has been employed. We exploited *μCP* of *antifouling* thiol TOEG6 on gold with the aim of driving cell stretching along the stripes pattern: analyzing aligned cells some quantitative evaluations have been done.
Our hypothesis was funded on understanding if there was a correlation between nuclear and cytoplasmic alignment, a clear signal of nuclear deformation played by actin filaments. Quantitative analysis performed in this chapter revealed this kind of correlation. The study of the nuclei morphology from the fluorescence images is very simple and can be easily automatized; once characterized nucleus-cytoplasm correlation, it will be possible to merely measure the nuclear axes to detect stretching events taking place in the cytoskeleton.
Axes analysis has been performed manually, choosing among various cells. In the future it will be desirable to develop software to automatize and speed up the procedure.

The fabrication of chemical gradients is widely cited in literature [6], [7] and the application of these kind of surfaces represents a new frontier in the field of cell adhesion study. Creating a smart surface using a gradient offers new possibilities to control cell adhesion and migration from an *antifouling* to a *fouling* area. The two different modes of quantitative analysis show the same result: a gradient is actually existing and it goes from low to higher cell density, both expressed by DAPI count (single cells counting) or by occupied area percentage (via GFP images examination). PSDF analysis corroborates these observations.

Material and Methods

Microcontact Printing of TOEG6

TOEG6 (Top oligo (ethylene-glycol), HS-$(CH_2)_{11}$-OEG_6-OH) was purchase from Prochimia, Poland. A polydimethylsiloxane (PDMS) mold was obtained by replica molding of a master with designed topographical features (microchannels). A solution of TOEG6 300µM in Ethanol (Fluka 02860) was prepared and 20µl were placed onto the patterned side of the PDMS replica; using a pipette tip the solution is spread onto the whole mold surface, then the wet face is placed onto a filter paper without exert any pressure and finally the superfluous solution is gently dried using N_2 flow.
The printing is made placing the stamp for 20'' on the surface with a slightly compression. It is possible to recycle the stamp two times before wetting again.
TOEG6 pattern is incubated over-night at 4°C.

Gradient fabrication via cyclic electro voltammetry

Glass or SiO_2 slides covered with gold (rectangular shape 1cmx3cm) are dipped over-night at 4°C in a solution of TOEG6 300µM in Ethanol to allow the SAM formation. Electrochemical desorption is performed using a 3 electrodes chamber (previously described in chapter 2), in which the working electrode (WE) is the gold slide, that is bathed in the electrolyte solution (KOH 0,5M). The reference electrode (RE) is Ag/AgCl, the counter electrode (CE) is made of platinum. Using a motor-powered machine (Figure MM.1), the slide is gradually removed from the solution, with constant and controlled speed.

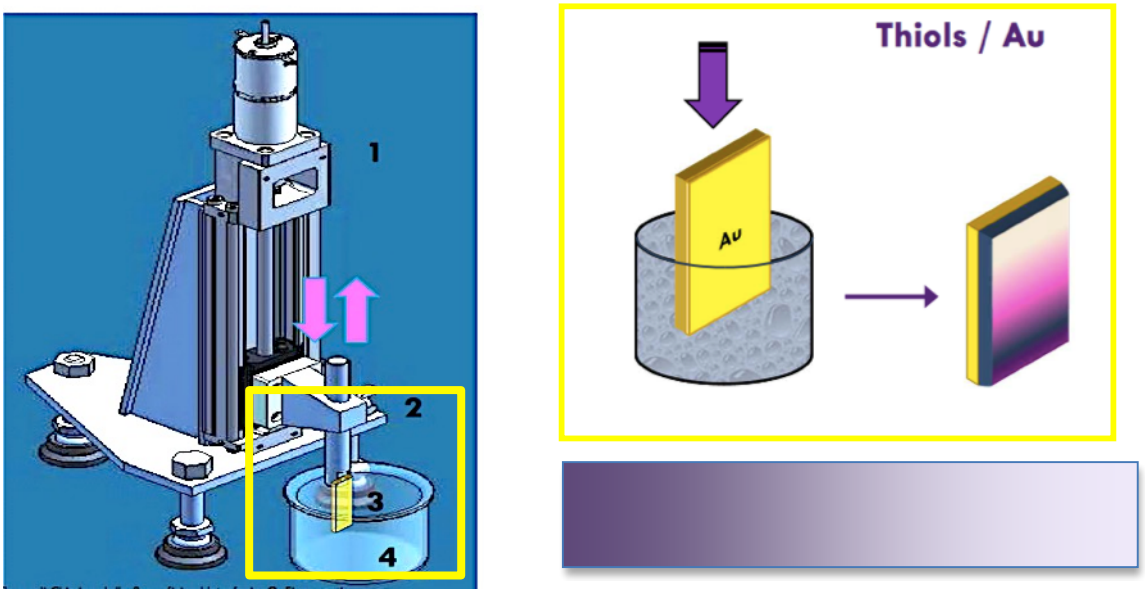

*Figure **MM.1**: Motorized machine for the continuing slide removal. **1**- Motor. **2**- Motorized guide. **3**- Slide to desorb (WE). **4**- Electrolytic KOH solution.*

The motorized machine has been designed and fabricated by Dott. Mauro Murgia (ISMN-CNR, Bologna).

The applied potential for desorbing is tested before the gradient creation and it fluctuates from -0,9 to -1,1V. When the slide is completely arisen, the surface that we get has an higher density of TOEG6 in the upper part, the one that has been less desorbed (white in the picture on the right), while the lower part, lately extracted from the solution and for this reason more desorbed, has minor density of TOEG6 (dark purple).

Data analysis on Microcontact Printing

*We used ImageJ software for analyzing the results on cell alignment by means of Microcontact Printing. We took both DAPI and Phalloidin images (correspondingly blue and red), six for each filter, then we picked 10 cells for each picture, well distinguishable and well-defined (both aligned and not). We measured minor (**a**) and mayor axis (**A**) for all cells, collecting them in tables.*
The measurement tables can been analyzed with Origin software for doing the calculation of the ratio between difference and sum of the two axis:

$$\frac{A-a}{A+a}$$

For obtaining the graph in Figure 6.3c and 6.3g we have to put on X the column that contains cells (SAMPLE column), on Y1 and Y2 the two columns that contain the axis ratio for nucleus and cytoplasm.
For obtaining the interpolation graph, on X we have to put the cytoplasm axis ratio and in Y the nuclei axis ratio and the software can calculate the interpolation automatically.

Bibliography

[1] S. V. Graeter, J. Huang, N. Perschmann, M. López-García, H. Kessler, J. Ding, and J. P. Spatz, "Mimicking cellular environments by nanostructured soft interfaces," *Nano Lett.*, vol. 7, no. 5, pp. 1413–1418, 2007.

[2] E. Bystrenova, M. Jelitai, I. Tonazzini, A. N. Lazar, M. Huth, P. Stoliar, C. Dionigi, M. G. Cacace, N. Nickel, E. Madarasz, and F. Biscarini, "Neural networks grown on organic semiconductors," *Adv. Funct. Mater.*, vol. 18, no. 12, pp. 1751–1756, 2008.

[3] J. E. Dumont, S. Dremier, I. Pirson, and C. Maenhaut, "Cross signaling, cell specificity, and physiology," *Am. J. Physiol. - Cell Physiol.*, vol. 283, no. 1, pp. C2–C8, 2002.

[4] A. Cossaro, R. Mazzarello, R. Rousseau, L. Casalis, A. Verdini, A. Kohlmeyer, L. Floreano, S. Scandolo, A. Morgante, M. L. Klein, and G. Scoles, "X-ray diffraction and computation yield the structure of alkanethiols on gold(111)," *Science (80-.).*, vol. 321, pp. 943–946, 2008.

[5] G. Fioravanti, F. Lugli, D. Gentili, V. Mucciante, F. Leonardi, L. Pasquali, A. Liscio, M. Murgia, F. Zerbetto, and M. Cavallini, "Electrochemical fabrication of surface chemical gradients in thiol self-assembled monolayers with tailored work-functions," *Langmuir*, vol. 30, no. 39, pp. 11591–11598, 2014.

[6] X. Han, L. Wang, and X. Wang, "Fabrication of Chemical Gradient Using Space Limited Plasma Oxidation and its Application for Droplet Motion," *Adv. Funct. Mater.*, vol. 22, no. 21, pp. 4533–4538, Nov. 2012.

[7] S. M. Morgenthaler, S. Lee, N. D. Spencer, E. T. H. Zurich, and C.- Zu, "Submicrometer Structure of Surface-Chemical Gradients Prepared by a Two-Step Immersion Method," no. 12, pp. 9797–9802, 2006.

Chapter 7 – Biodegradable and Biocompatible polymers for regenerative medicine applications

In this chapter a general review on biodegradable/biocompatible polymers used for regenerative medicine (mainly spinal cord injury (SCI) repairing) will be provided. In particular, we will describe two of these materials: PLGA (already seen in the previous chapters) and PHB poly(3-hydroxybutyrate), that have been used for this application.

7.1 Introduction

Biomaterial is a term used to categorize such materials and devices that directly "interact" with human tissues and organs [1].
The interaction can be both structural and functional and occurs through their surfaces. For this reason, it is extremely important to characterize biomaterial surface properties in order to achieve a good integration with the host tissue (making the material *biocompatible*) [2]. Basically, the scaffold should be porous, because the pore structure is necessary to allow cells infiltration into the scaffold, supply O_2 and nutrients and washout cellular wastes. Once tissue regeneration is naturally arisen, cells start to produce naturally their ECM: the scaffold is therefore a temporary platform of cell activities and a persistent retention of this foreign object sometimes can cause physical interference against the natural regeneration project. Successful tissue regeneration needs to control the timing of scaffold deterioration trying to make the chosen material as closer as possible to be 100% *biodegradable*.
At the beginning of the iOne project, a deep bibliographic research was performed with the aim of having a large vision on the world of biodegradable/biocompatible polymers. Weighting some functional and practical advantages, we finally decided to choose two different polymers: PHB poly(3-hydroxybutyrate) and PLGA poly(lactic-co-glycolic acid). In this chapter we will describe fabrication, characterization and uses of PHB, whereas, concerning PLGA, we will just talk about one application in the construction of microfluidic devices (a deeper portrayal of PLGA has been given in Chapter 3).

7.2 PHB (poly(3-hydroxybutyrate))

Polyhydroxyalkanoates (PHAs) are bacterial polymers, made as naturally occurring storage polyesters by a wide range of microorganisms usually under unbalanced growth

conditions [3]. Biotechnological processes under controlled conditions can also produce PHAs. Mechanical properties of PHAs make them suitable alternatives for petrochemically produced bulk plastics (polyethylene, polypropylene etc.), but, in contrast to these plastics, PHA are completely degradable to carbon dioxide and water through natural microbiological mineralization. Poly-3-hydroxybutirate (PHB) and its copolymers with 3-hydroxyvalerate (3HV), poly(3-hydroxybutyrate-co-3-hydroxyvalerate) (PHBV), are the best known representatives of PHA family. These polyesters have attracted widespread attention, as environmentally friendly polymers, which can be used in a wide range of agricultural, industrial, and, moreover, medical applications.

In the last decades, potential applications of bacterial PHB and related PHAs as biodegradable and biocompatible materials in medicine have attracted a wide attention. A challenging combination of biomedical and biodegradable properties of PHB is a perspective tool in designing novel medical devices and tissue engineering. Over the past years, PHAs, particularly PHB, have been used to develop devices including sutures, repair devices, repair patches, slings, cardiovascular patches, orthopedic pins, adhesion barriers, stents, guided tissue repair/regeneration devices, articular cartilage repair devices, nerve guides, tendon repair devices, bone marrow scaffolds, and wound dressings [4]. Moreover, the capability of PHB for encapsulation and controlled release of different drugs allows applying PHB for development of therapeutic systems of sustained drug delivery.

PHB films were fabricated through the dissolution of PHB powder in Chloroform at 60°C: the dissolution does not occur at room temperature (a detailed description is given in Materials and Methods at the end of the chapter).

We used solution casting for the fabrication of PHB film. At first, PHB solution was poured onto a glass Petri dish (6 cm of diameter).

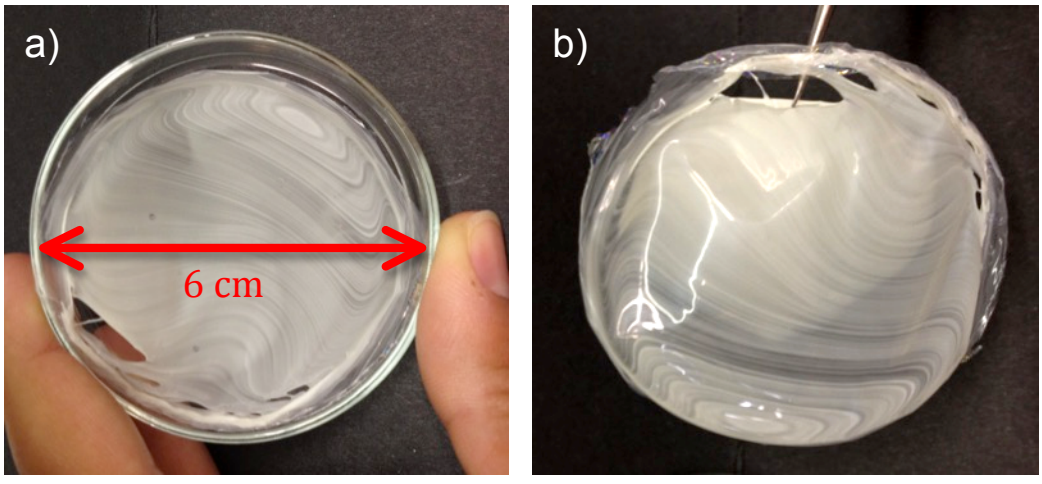

*Figure **7.1**: PHB film made in Petri dish. The film side in a) is the one that has been in contact with air under the chemical hood, while the side in b) has been in touch with Petri glass surface.*

In Figure 7.1 we can see how the PHB film after the total evaporation of $CHCl_3$ that occurs under chemical hood. The film is white and not transparent, except in few tiny areas. It is easy to peel off and to handle; it is also very easy to cut, like cutting a sheet of paper. As we can see, the two faces of PHB look macroscopically different: the face in 7.1a is more 'matt' compared to the face in 7.1b that looks almost glossy. The microscopic characterization confirmed this observation (see Figure 7.2).

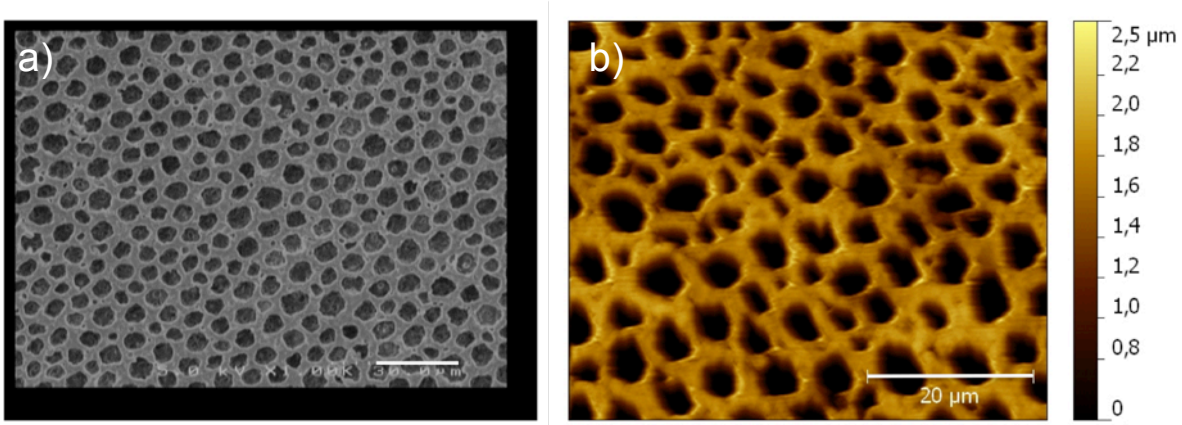

*Figure **7.2**: PHB film "air face" characterized by SEM a) and AFM b). Scale bar is 20 µm.*

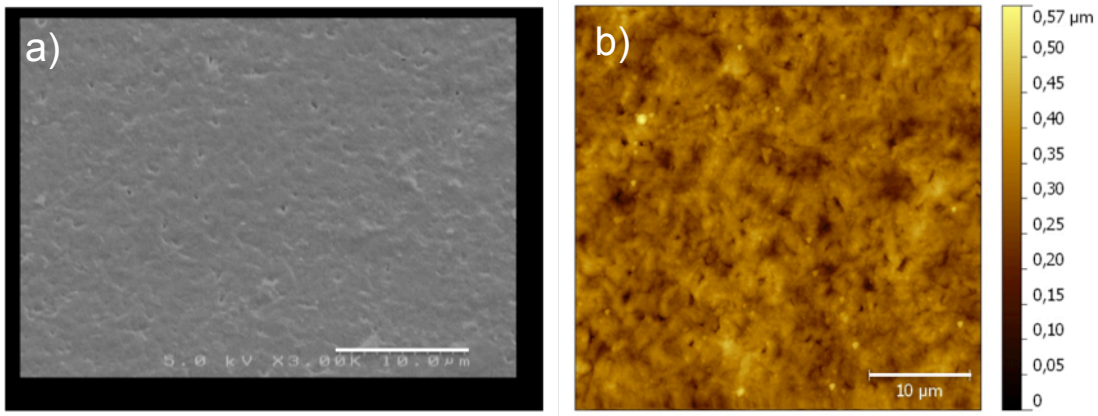

*Figure **7.3**: PHB film "glass face" characterized by SEM a) and AFM b). Scale bar is 10 µm.*

In Figure 7.2 the 'air face' of PHB film shows a spongy structure, with pores 6-7 µm of average diameter. The average roughness of the surface, calculated by AFM images, is 443 nm. The 'glass face' in the pictures below (Figure 7.3) is absolutely different: the ordered and regular spongy surface is lost, except for some pores, the roughness is also different and its value is 45,7 nm. This difference from one to the other side is probably due to the evaporation of $CHCl_3$ from the polymer mixture that occurs through the area exposed to air in a very short time (because of the high volatile nature of the solvent).
Using an optical profilometer (*Sensofar*, Schaefer Technologie GmbH, Germany) we measured the thickness of the film in three chosen positions as shown in Figure 7.4.

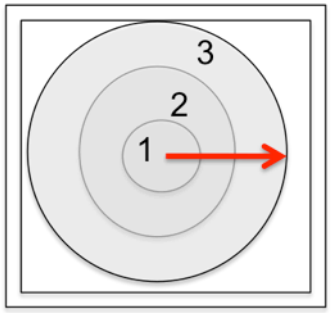

1st area	2nd area	3rd area
50 ± 4,2 µm	75 ± 5,8 µm	115 ± 7,7 µm

*Figure **7.4**: Representation of PHB film made in Petri dish and the three selected positions in which we made the profilometer measuring. In the table on the right the mean values and the errors are reported for each position.*

The thickness increases from the central area to the edge of the film from 50 to 115 µm, possibly because of the inhomogeneous flatness of the Petri dish and of the not-controlled evaporation of $CHCl_3$ without monitoring surrounding humidity.
With the aim of enhancing and improving the homogeneousness of PHB film, both in the surface features and in the average thickness, we decided to employ the same strategy (solution casting) in a confinement regime, by using a silicol pool (1cmx1cm) the same in which we fabricated PLGA film as described in Material and Method section in Chapter 3. For better adjusting also $CHCl_3$ evaporation, after poured, samples were placed in oven at 37°C with controlled humidity (as done for PLGA films).
In Figure 7.5 the complete macro and microscopic characterization of a PHB film made in confinement pools is reported.

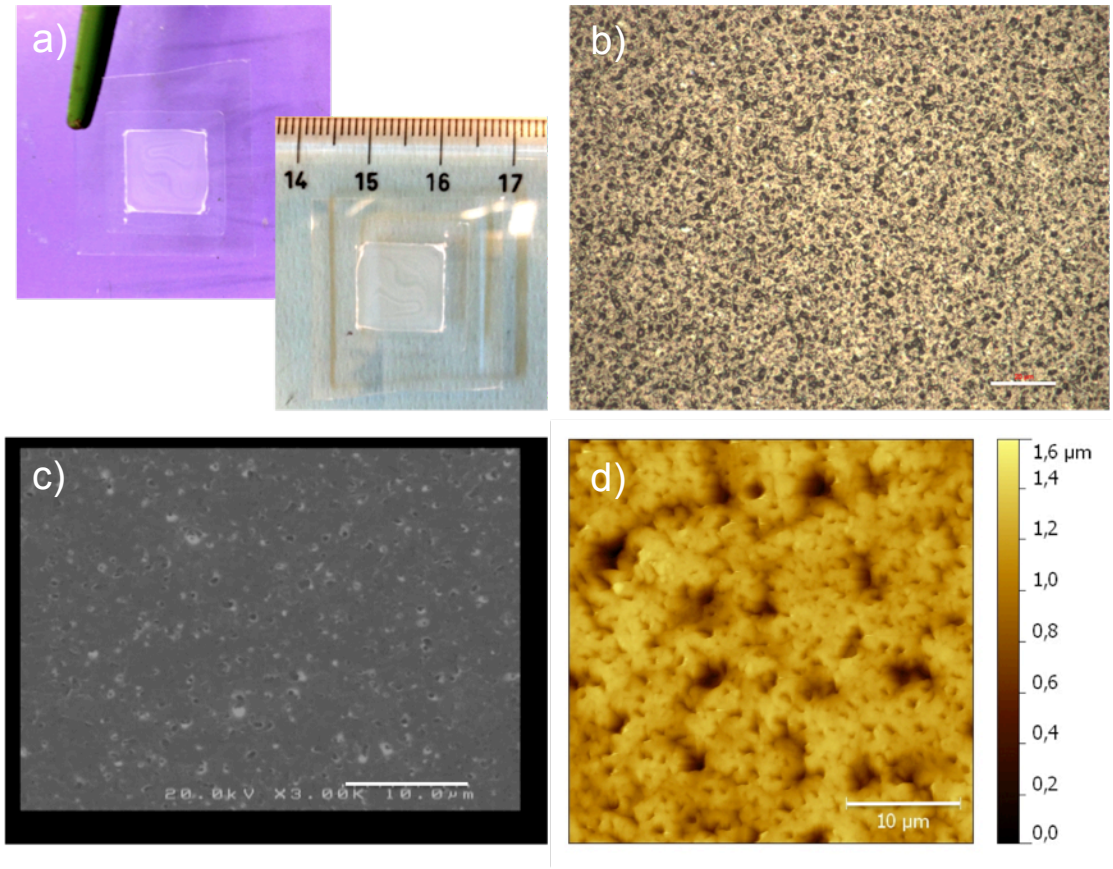

*Figure **7.5**: a) 1cmx1cm PHB film poured onto cleaned glass in silicon confinement pool. b) Optic, c) SEM and d) AFM characterization images. Scale bar is 20 µm in b) and 10 µm in c) and d).*

As we can see, the appearance in color and transparency of these PHB films made in silicon pool is quite similar to the one made in the Petri dish. The spongy structure is found again, but it is not regular as the one observed in Figure 7.2; here pores are randomly distributed and smaller. Roughness is 173 nm and thickness has been measured by optical profilometer (see table in Figure 7.6) in the three neighboring positions. The achieved results are much more uniform compared to those shown in Figure 7.4.

1st area	2nd area	3rd area
6,2 ± 0,7 µm	6,5 ± 0,7 µm	7,5 ± 1,1 µm

*Figure **7.6**: Optical profilometer height values for the 1st position (central area), the 2nd (midway) and 3rd (edge) of the PHB film.*

Static contact angle of PHB films has been measured with water: the mean Θ value for both types of film is 76,5° ± 0,4°.

7.3 NPC and NE4C cells on PHB films

To assess PHB biocompatibility, we performed cell culture on the fabricated polymer films. In Materials and Methods, at the end of this Chapter, all the specifics about cell seeding are described. Two different cell types were tested: our NE4C stem cell line (see Chapter 3) and NPC neural stem cells, a primary cell line obtained from mice by the group of Professor Stefano Pluchino (Cambridge University, UK) [5].
The experiment was 24h and 48h for NE4C and 2, 4 and 6 days for NPC with the aim of evaluating cell adhesion and proliferation.
In Figure 7.7 SEM images of NE4C cultures are displayed. Cells adhere well on PHB both after 24h (7.7a-b) and 48h (7.7c-d) and begin to produce extracellular matrix, as visible in the enlarged pictures in 7.7b an 7.7d. The proliferation from the initial seeded cell number has not been quantitatively valued, but the two images in 7.7a and 7.7c give a qualitative idea on the increasing amount of cells just observing the cellular coverage on the film surface.

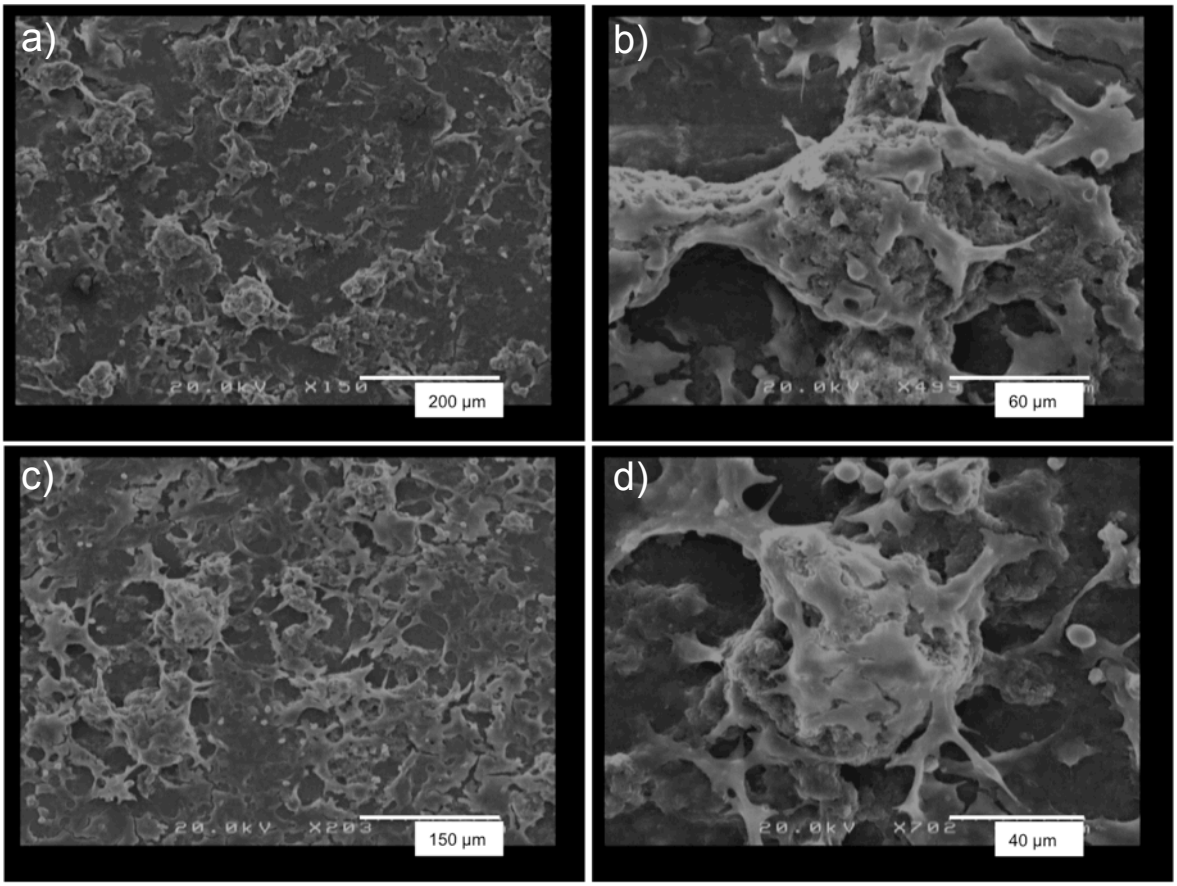

*Figure **7.7**: NE4C culture on PHB film after 24h (a) b)) and 48h (c) and d)).*

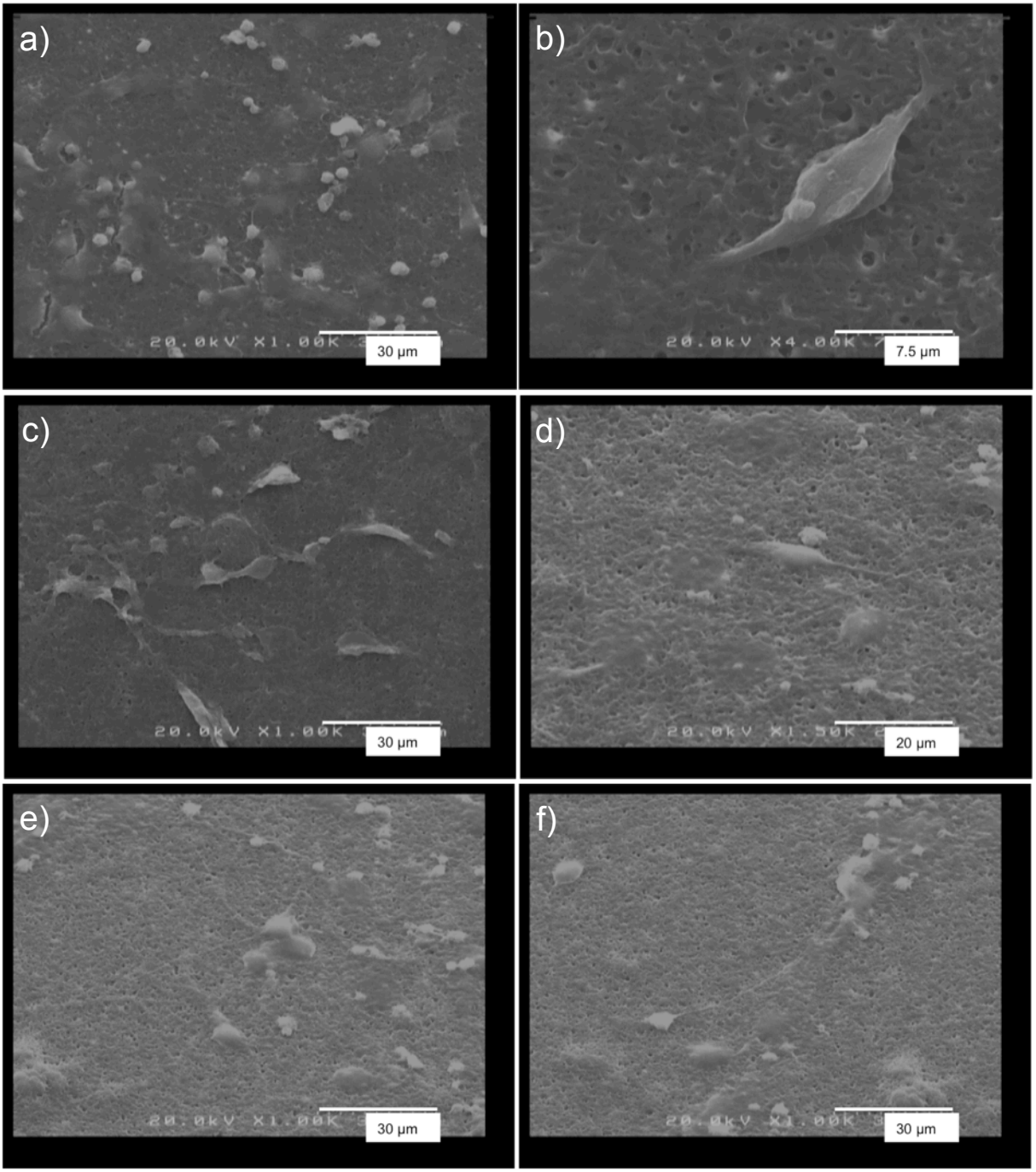

*Figure **7.8**: NPC culture on PHB film after 2days (a) (b), 4 days (c) (d) and 6 days (e) (f).*

NPC adhesion onto PHB films is relatively worst than NE4C adhesion: in fact, if we look at cell shape in SEM images (Figure 7.8), we can see that some cells are spherical and don't exhibit the typical morphology of a cell in a very healthy condition. Cell proliferation has not been quantitatively assessed, but the observable coverage in 7.8a-b (2days), 7.8c-d (4days) and 7.8e-f (6days) is quite similar.

7.4 Microfluidics systems made of PLGA

As briefly described at the end of Chapter 1, the ultimate iOne device layout has to integrate both electronic and microfluidic (μ-fluidic) components. In other terms, the organic transistors must provide an electrical stimulation, once coupled to a biological means (such as tissue, cells etc.); on the other side, microfluidic system guarantees the delivery of anti-inflammatory drugs. In this way, the final object has two functionalities: (i) an electrical stimulator able to induce biological activity in the spinal cord injury and (ii) an inflammatory controller because it can release anti-inflammatory drugs in the wound zone.

In this paragraph an overview about the manufacture of microfluidics devices made of biodegradable materials, as PLGA film (see Chapter 3 for details about polymer fabrication), is given. Since the final implant is based on PLGA substrate, the same material will compose even the μ-fluidic system. This enables an easy integration. Flexibility, easy-fabrication and mechanical robustness are the stringent requirements to be fulfilled for the future implant. PLGA film fabrication has been already abundantly described in Chapter 3. Two different types of μ-fluidic systems have been fabricated in order to satisfy the stringent requirements of device platform. For sake of clarity, the two μ-fluidic systems will be termed "ver.1" (see Fig7.9a. and Fig7.9b.) and "ver.2" (see Fig7.9c and Fig7.9d). The fabrication protocol of ver.2 involves the same replica molding procedure adopted for ver.1 starting from a different layout, while the main difference between the two versions lies in the lacking of the metallic needle that connects silicone tube and inlet. The fabrication protocols of the ver.1 and ver2 are described in Materials and Methods section.

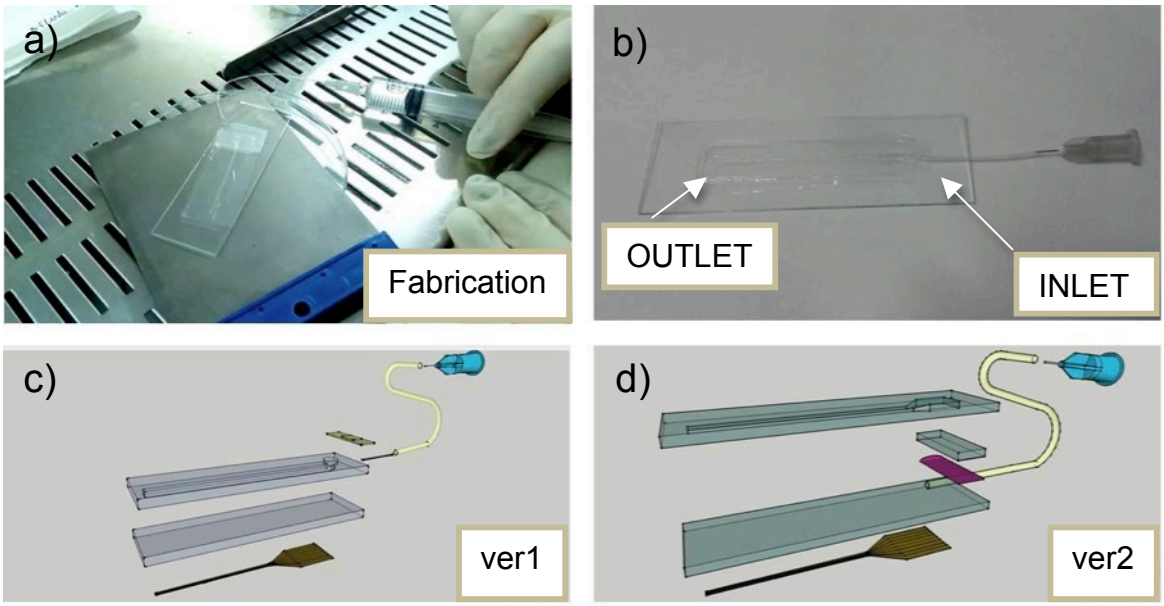

*Figure **7.9**: Pictures of μ-fluidic systems: Ver.1 (a) and Ver.2 (b). Cartoons of the single components of ver.1 (c) and ver.2 (d).*

Although the effective functionality of ver.1 has been validated, some technical drawbacks have been identified. In particular the junction between needle and inlet is the weakest point of the whole system. This is likely due to different reasons: i) unfavorable match between surface tension of PLGA (hydrophobic) and metal needle (hydrophilic), ii) excessive liquid counter pressure due to the narrow section of μ-channel (see Fig.2a and Fig.2c) and iii) possible presence of PLGA cracks because of needle insertion. In ver.2, the inlet junction is completely hydrophobic, because the silicone tube is directly fixed to the PLGA μ-fluidic system (see Fig.2b and Fig.2d). This confers higher flexibility and stability, which is crucial aiming at an implant subjected to movements coming from the animal alive.

7.5 NE4C cell adhesion gradient on PLGA microfluidics

Two type of validation have been carried out: a cell adhesion test through the formation of laminin gradient and the delivery of minocycline (an experiment performed by the group of Prof. Stefano Pluchino from University of Cambridge and not shown in this thesis). Laminin improves cell adhesion [6] whereas minocycline is a powerful anti-inflammatory agent [7]. Both experiments require a pool mounted around the outlet for the cell seeding and growth. This allows us, after the injection in the channel of a small volume (50μl) of laminin solution, to create a gradient of laminin that goes circularly from the outlet up to the peripheral zones of the pool (see Fig.7.10). Fluorescent assays show dense crowding of cells around the outlet with respect to peripheral areas. The histograms quantify this qualitative proof arisen from the optical images (Fig.7.10a and Fig.7.10b). Furthermore, it has been verified how a homogeneous spread of laminin does not induce any local cell crowding: in Fig. 7.10d the cell-crowding index for positive and negative control samples is shown.
A “positive sample” is a μ-fluidic in which laminin hasn’t been injected in the pool area through the channel, but a 300μl volume of protein solution has been homogenously poured with a pipette in the silicon pool area. A “negative sample”, on the opposite way, doesn’t have any laminin coating.

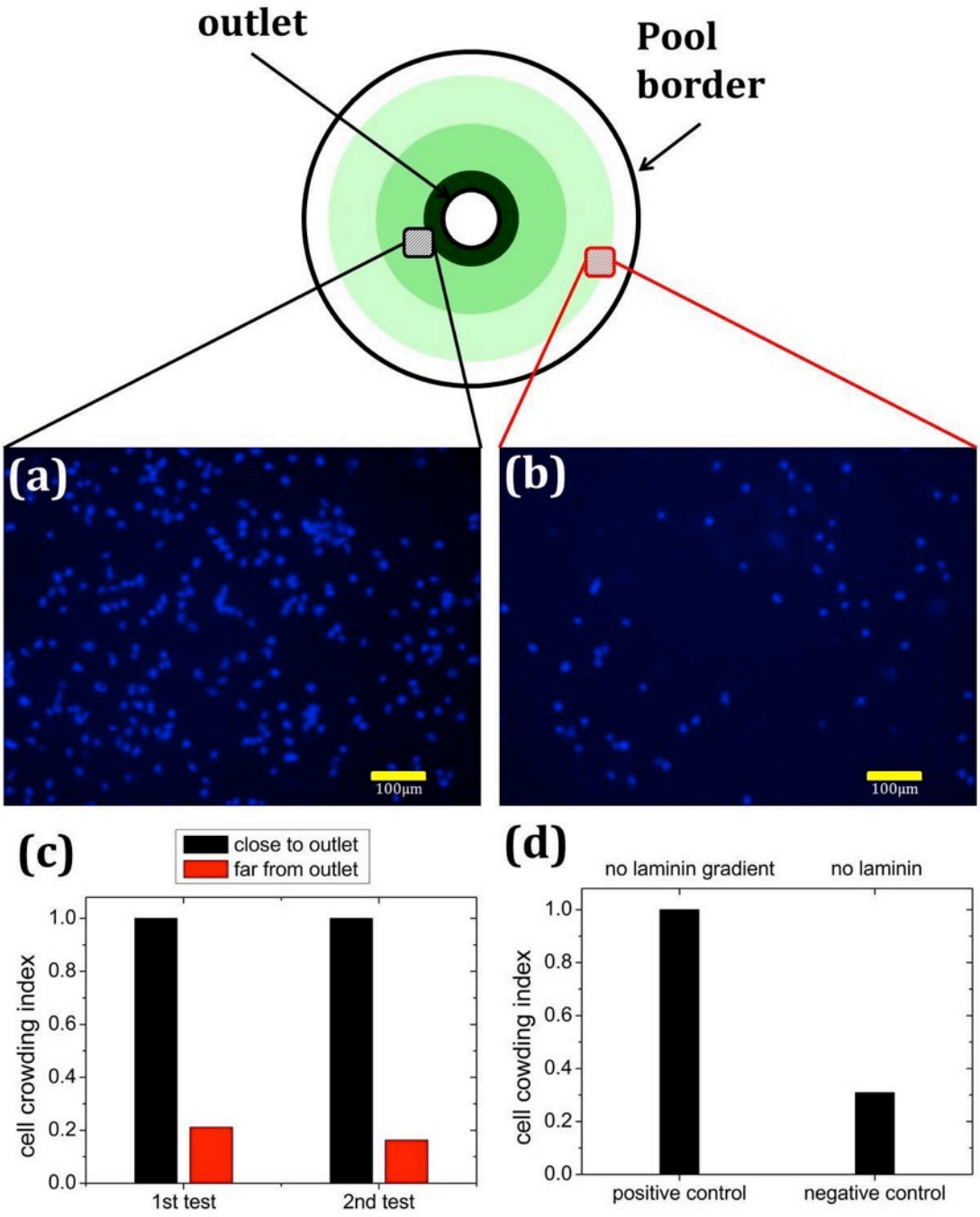

*Figure **7.10**: In the upper part, a 2D sketch of the pool area. The green circular shadows stand for the laminin gradient due to the incubation protocol. Fluorescence images of cell crowding close (a) and far (b) from the outlet are shown. Cell crowding index has been calculated for 2 runs of samples (c) as the normalized value of the nuclei totality; positive (laminin coating) and negative (no laminin functionalization) controls have also been checked (d).*

7.6 Discussion and conclusions

In this Chapter a synopsis on biodegradable/biocompatible polymers used for regenerative medicine (SCI repairing, in our case) has been presented. In particular, we described two of these biomaterials: PHB and PLGA.
PHB film has been fabricated both in Petri dish and in confinement regime in a silicon pool: the complete characterization has been assessed by contact angle, optical microscopy, AFM and SEM. The film made by the solution casting of PHB in $CHCl_3$ is a mat film, easy to cut, completely water insoluble and resistant to hydrolytic degradation, for at least 2 weeks. Cell viability has been demonstrated using two different cell lines: NE4C and NPC (University of Cambridge).
For what concerns PLGA characterization and cell viability, it has been widely discussed in Chapter 3. However, in this Chapter, an additional use of PLGA film is portrayed: it has been developed an effective and robust μ-fluidic system capable to delivery homogenously drugs, such as minocycline. Furthermore, it has been demonstrated that it is also possible to create surface gradient on PLGA substrate (by means of laminin) inducing local cell crowding. This μ-fluidic system is completely based on PLGA; therefore its future integration with the electronic transducer for the complete achievement of iOne project goals will be straightforward.

Materials and Methods

Substrate preparation

PHB was purchased from Sigma Aldrich (363502 Poly[(R)-3-hydroxybutyric acid], mol wt 150 KDa, 99,9% purity). PHB films (thickness= 5,5 ± 1,5 μm) were prepared by solution casting using 2%wt PHB chloroform solution at 70°C, with mechanical agitation in a reflux controlled system. PHB films have been fabricated onto cleaned glass substrates in a confining elastomeric frame (1,2cm x 1,2cm) or into cleaned glass Petri dishes (∅ 6cm). The glass slides, the Petri dishes and the elastomeric confining frames were cleaned with 15' sonication in Ethanol 99,9% and allowed to dry under chemical hood. Then the frames, when used, were mounted on the glass surfaces taking care to make them adhering to each other. Once the PHB was completely dissolved in chloroform, the liquid solution was poured onto the glass slides and the Petri glass surfaces (respectively 100 μl and 10 ml). After the complete evaporation of chloroform (6-8h in oven 37°C), the silicon frame was removed from the slides. The resulting film was then sterilized before use.

Substrate characterization

PHB films were characterized by different microscopy techniques like optical microscopy (Olympus BX51, software Infinity), atomic force microscopy (AFM), this last has been used to achieve a high resolution surface characterization of the film surface. AFM images were acquired with a Smena microscope (NT-MDT, Moskow, Russia) operated in semicontact mode under ambient conditions. The cantilevers employed were NSG01 (NT-MDT, Moscow, Russia) with a nominal tip radius of curvature of 10 nm and a resonance frequency of between 87 and 230 kHz. Images were analyzed using the opensource software Gwyddion ; the size and the height of the surface features were measured by the section analysis tool. SEM analyses were performed using a SEM-FEG Hitachi S4000 (Vext = 20 keV; i = mA) (Hitachi, Tokyo, Japan).

PLGA Microfluidic devices fabrication

As previously said, two versions of the μ-fluidic device has been fabricated (ver1 and ver2 showed in Figure 7.9). For both types, the μ-fluidic master is produced by the "replica molding" technique (see Chapter 2), although ver2 starts from a different layout.
Replica molding technique consists of three steps:
1. A photolithographic mask has been produced bearing the layout of the μ- fluidic system by laser-assisted ablation using ScribaR Laser Mark.
2. The μ-fluidic master is embossed on a polypropylene substrate by pressing (~160 psi) at 90°C for 3-4 minutes.
3. This master is then covered by PLGA solution, yielding a final thickness <100μm.

At this point, the PLGA replica is placed on another PLGA substrate (5.5cm x 1.5cm) and the two layers are sealed by heating (T>60°C) for 1min by means of hot plate. The liquid injection is guaranteed by using a silicone tube featuring an internal diameter of 300µm. In the first version of the µ-fluidic device, at both ending sides of this tube two metallic needles are fixed. As explained, ver.1 has some disadvantages in terms of easy manufacturing, handling etc. Ver.2 has a simplified µ-channel and it does not need a metallic needle as connection between silicone tube and the inlet. To achieve this new layout, the silicone tube has to be directly placed on a substrate PLGA (5cm x 1.5cm), and it is firmly fixed by means of a double layer of PDMS and PLGA. The µ-fluidic replica is now casted on the PLGA substrate and aligned to the fixed tube (internal diameter 300µm). Sealing is accomplished with a heating press dedicated for this technical purpose.

Cell culture and characterization

Maintenance of stem cell line NE4C on PHB films was carried out according to the published protocol. The stem cells were seeded at 73000 cells per cm² in a final volume of 400 µL of the complete medium (CM) (MEM containing 10% FBS, 4 mM glutamine, 40 mg/ml, 1 gentamicin and 2.5 mg/ml, 1 amphotericin) in sterilized silicon pool (∅ 1,6cm) and incubated under the standard cell culture conditions (37°C, 5% CO2 and 95% relative humidity).

Spinal cord Neural Stem/Progenitor Cells (NPC) derivation and maintenance

Three different lines of neural progenitor cells (NPCs) have been derived from the spinal cord of C57BL/6 mice. Adult C57BL/6 mice (n=15, 5 mice for each preparation) were culled by cervical dislocation and the spinal cords collected and kept in ice cold sterile phosphate buffered saline (PBS 1X). After carefully removing the meninges, whole spinal cords were dissected with a blade and dissociated in digestion medium [EBSS 1X, 200 mg/L Cysteine, 200mg/L EDTA (Sigma), 2 U/ml Papain) for 45 min at 37°C. Cells were centrifuged at 600 rpm for 10 minutes, the supernatant was removed and the pellet was mechanically dissociated and washed in PBS 1X. Cells were centrifuged at 600rpm for 10 minutes and resuspended in 0.9 M sucrose in EBSS. After centrifuging 10 minutes at 750 g, the pellet was resuspended in 200 µl of Complete Growth Medium (CGM, mouse NeuroCult basal medium, Stem Cell Technologies Catalog #05700 plus mouse NeuroCult proliferation supplements, Stem Cell Technologies Catalog #05701) in the presence of heparin 0.002% (Sigma #H3393), basic fibroblast growth factor (bFGF) [10 ng/ml] (Peprotech #100-18B-1000), epidermal growth factor (EGF) [20 ng/ml] (Peprotech #AF-100-15- 1000) and antibiotics (Penycillin/Streptomycin, Invitrogen #1514012). The cell suspension was slowly added on top of 4% bovine serum albumin (BSA) in EBSS, and centrifuged 7 minutes at 200g. The myelin-free pellet was then resuspended in CGM, plated in a 25 cm2 tissue culture flask and incubated at 37°C in an atmosphere of 5% CO2. After 7-10 days, a small percentage of the isolated cells began to form neurospheres.

For NE4C cell adhesion tests on PLGA µ-fluidic devices, a sterilized pool (∅ 1,6cm) has been sealed close to the outlet of the µ-fluidic. A laminin solution has been prepared with a final

concentration of 5µg/ml in physiological buffer. 2 µ-fluidic systems (ver.1) have been used confining a droplet of laminin just around the outlet. Another µ-fluidic system has been homogeneously wetted by laminin solution (termed "false positive"). Further 2 µ-fluidic systems were used only with physiological buffer (namely "without laminin"). The standard incubation protocol for laminin was applied. The stem cells were seeded at 25000 cells per cm^2 in a final volume of 500 µL of the complete medium (CM) and incubated under the standard cell culture conditions (37°C, 5% CO2 and 95% relative humidity). The seeding and adhesion steps lasted 5h, afterwards the cells were stained using DAPI to evaluate the adhered cells.

Cell crowding index has been calculated through the cell nuclei count using ImageJ software.

Bibliography

[1] V. K. Vendra, L. Wu, and S. Krishnan, *Polymer Thin Films for Biomedical Applications*, vol. 5. 2010.

[2] P. Vadgama, "2 Surface biocompatibility," *Annu. Reports Sect. "C" (Physical Chem.*, vol. 101, p. 14, 2005.

[3] A. P. Bonartsev, V. L. Myshkina, D. A. Nikolaeva, E. K. Furina, and T. A. Makhina, "Biosynthesis , biodegradation , and application of poly (3- hydroxybutyrate) and its copolymers - natural polyesters produced by diazotrophic bacteria," pp. 295–307, 2007.

[4] X.-Y. Xu, X.-T. Li, S.-W. Peng, J.-F. Xiao, C. Liu, G. Fang, K. C. Chen, and G.-Q. Chen, "The behaviour of neural stem cells on polyhydroxyalkanoate nanofiber scaffolds.," *Biomaterials*, vol. 31, no. 14, pp. 3967–75, May 2010.

[5] S. Pluchino, L. Zanotti, B. Rossi, E. Brambilla, L. Ottoboni, and G. Salani, "Neurosphere-derived multipotent precursors promote neuroprotection by an immunomodulatory mechanism," *Nature*, vol. 436, pp. 266–271, 2005.

[6] S. Dertinger, X. Jiang, Z. Li, V. Murthy, and G. M. Whitesides, "Gradients of substrate-bound laminin orient axonal specification neurons," *Proc. Natl. Acad. Sci. U. S. A.*, vol. 99, no. 20, pp. 12542–12547, 2002.

[7] J. E. A. Wells, R. J. Hurlbert, M. G. Fehlings, and V. W. Yong, "Neuroprotection by minocycline facilitates significant recovery from spinal cord injury in mice," *Brain*, vol. 126, pp. 1628–1637, 2003.

CONCLUSIONS

In this thesis the use of different approaches for the fabrication of smart surfaces have been explored, with the aim of providing precise control of cell behavior, adhesion, proliferation and differentiation, through chemically and spatially designed surfaces.
In particular, the research activity has been focused on the adhesion and proliferation of three cell lines (NE4C stem cells, a neurons-astrocytes lineage, human SH-SY5Y neuroblastoma and murine NIH-3T3 fibroblasts) with respect to chemical and topographical stimuli. This is important for understanding the process of cell adhesion, positioning and migration, targeted at cell and tissue regeneration that is a key issue for central nervous system diseases and spinal chord injuries.

To investigate cell response to chemical signals, patterns of a cell adhesive molecule such as laminin on biodegradable/biocompatible PLGA films have been fabricated, by means of Laser Assisted Bioprinting, obtaining neural stem cells adhesion upon laminin pattern, also when PLGA had no topographic guidance. Differentiation, however, occurred only in presence of hydrated PLGA scaffolds; moreover, the presence of laminin spots induced anisotropic orientation of the neurite processes from large cellular clusters. Probability of NE4C adhesion on gradually spaced droplets of laminin has been evaluated too, both by mathematic simulation model and experimentally. LAB technique has been successfully employed for the functionalization of microcantilevers with single laminin droplets, noticing how the position of the drop lengthways the beam was critical for changing the resonance frequency response: a promising way for ultrasensitive and specific recognition of biological targets.
Microfabrication obtained by LAB allows tailoring morphological and chemical cues for adhesion and differentiation, represents a valuable tool in engineering devices for studying the recruiting and differentiation of autologous stem cells.

In order to assess SHSY5Y cells behavior with respect to chemical cues, the use of Litographically Controlled Wetting for patterning β-cyclodextrins ACyD on a glass support with modified hydrophobicity rate has been described.
With the same purpose of controlling cellular adhesion, we employed Microcontact Printing of antifouling molecule TOEG6 and NIH-3T3 cells alignment along the fouling-antifouling stripes has been demonstrated.
In parallel to this 'discrete mode' of surface functionalization, using the electrochemical desorption of self-assembly monolayers of TOEG6, has been possible to fabricate also a continuous chemical gradient to affect cell adhesion and growth.

Finally the last chapter discussed a very recent study about the fabrication of biodegradable-biocompatible microfluidics made of PLGA for the delivery of small volumes of active molecules, preceded by a brief paragraph on the use of Polyhydroxybutyrate (PHB), a biodegradable polymer, for cell adhesion and growth.

List of Acronyms

3HV 3hydroxyvalerate
ACYD Amphiphilic cyclodextrin
AMID Active Multifunctional implantable device
AFM Atomic Force Microscopy
AU Arbitrary Unit

BDNF Brain Derived Neurotrophic Factor
BFGF Basic Fibroblast Growth Factor
BioLP Biological Laser Printer
BOE Buffered Oxide Etch
BSA Bovine Serum Albumin
BSE Back Scattered Electrons

CD Cyclodextrin
CE Counter Electrode
CL Cathodoluminescence
CM Complete Medium
CNS Central Nervous System
CPD Critical Point Drying
CV Cyclic Voltammetry

DAPI 4'-6'-diamidino-2-phenylindole
DM Differentiation Medium
DMEM Dulbecco's Modified Eagle's Medium
DPD Dissipative Particle Dynamics
DPL Dip Pen Lithography

EBSD Electron Back Scattered Diffraction
EBSS Earle's Balanced Salt Solution
ECD Electrochemical Desorption
ECM Extracellular Matrix
EDS Energy Dispersive Xray Spectrometry
EDTA Ethylenediaminetetraacetic acid
EGF Epidermal Growth Factor

FDA Food and Drug Administration
FEG Field Emission Gun
FET Field Effect Transistor
FITC Fluorescein Isothiocyanate
FT Fourier Transform

GFP Green Fluorescent Protein

ICS Intelligent Cell Surface
IF Immunofluorescence
IONE Implantable Organic Nano Electronics

LAB Laser Assisted Bioprinting
LCW Lithographically Controlled Wetting
LIFT Laser Induced Forward Transfer
LON Local Oxidation Nanolithography

MAPLE Matrix Assisted Pulsed Laser Evaporation
MC Microcantilever
MCF Mark Connection Function
MD Molecular Dynamics
MEM Modified Eagle's Medium
MEMS Micro Electro Mechanical System
MIMIC Micro Molding in Capillaries
MM Molecular Mechanics

NIL Nano Imprinting Lithography
NPC Neural Progenitor Cells
NPs Nano Particles

PA Probability of Adhesion
PBS Phosphate Buffered Saline
PDMS Polydimethylsiloxane
PEG Polyethylene Glycol
PF Paraformaldehyde
PHA Polyhydroxyalkanoate
PHB Polyhydroxybutyrate

PHBV PHB-co 3 hydroxyvalerate
PID Proportional Integral Derivative
PLGA Poly(lactic-co-glycolic acid)
PPD Pulsed Plasma Deposition
PSD Position Sensitive Detector
PSD/PSDF Power Spectrum Density/Function
PVD Physical Vapor Deposition
PZT Piezo Zirconium Titane

RE Reference Electrode
REM Replica Molding
RIE Reactive Ion Etching
RMS Root Mean Square
RSA Random Sequential Adsorption
RT Room Temperature

SAM Self Assembly Monolayers
SAMIM Solvent Assisted Micro Molding
SCI Spinal Cord Injury
SEM Scanning Electron Microscopy
SOI Silicon On Insulator
SPR Surface Plasmon Resonance
STM Scanning Tunneling Microscopy

TEM Transmission Electron Microscopy
TOEG6 Top Oligo Ethylene Glycol
TRITC Tetramethylrhodamine

WE Working Electrode

μCP Micro Contact Printing
μTM Micro Transfer Molding

List of Publications

1. F. Valle, M. Bianchi, S. Tortorella, G. Pierini, F. Biscarini, M. D'Elia "Nanotechnology for forensic sciences: analysis of PDMS replica of the case head of spent cartridges by optical microscopy, SEM and AFM for the ballistic identification of individual characteristic features of firearms" *Forensic Sci. Int.* vol. 222(1-3), pp. 288-97, Oct. 2012.

2. A.C. Dumitru, F.M. Espinosa, R. Garcia, G. Foschi, S. Tortorella, F. Valle, M. Dallavalle, F. Zerbetto, F. Biscarini "*In situ* nanomechanical characterization of the early stages of swelling and degradation of a biodegradable polymer" *Nanoscale*, vol. 7, pp. 5403-5410, 2015.

3. S. Tortorella, P. Greco, F. Valle, M. Barbalinardo, G. Foschi, F. Biscarini, "Laser Assisted Bioprinting of laminin on biodegradable PLGA substrates for neural stem cell adhesion and differentiation" *submitted to Nanomedicine: Nanotechnology, Biology, and Medicine on Jan. 2015.*

4. S. Tortorella, F. Valle, F. Leonardi, M. Barbalinardo, M. Checchi and M. Cavallini, "Surface chemical gradients in thiol self-assembled monolayers fabrication for controlling and guiding cell adhesion" *in preparation.*

5. M.Dallavalle, F. Lugli, S. Tortorella, P. Greco, F. Valle, S. Rapino, F. Biscarini and F. Zerbetto, "Mathematic coarse-grained model for studying NE4C cells behavior on surfaces patterned by Laser Assisted Bioprinting" *in preparation.*

6. A. Mazzaglia, F. Valle, S. Tortorella et al. "Amphiphilic β-Cyclodextrins ($SC16NH_2$) patterning on substrates with different surface tension effects cell positioning" *in preparation.*

Acknowledgements

Desidero ringraziare tutte le persone che hanno reso possibile il mio lavoro negli ultimi tre anni, traducendolo nella ricca serie di esperimenti descritta in questa tesi di Dottorato.
In primis, voglio ringraziare il mio *supervisor*, il Prof. Fabio Biscarini, il quale scommise su di me nel lontano 2011, quando ero ancora una giovane studentessa, e che, come con tutti i suoi collaboratori, mi ha formato per affrontare il mondo della ricerca da vincente.

Ufficialmente Grazie al Prof. Francesco Zerbetto, relatore della mia tesi di Dottorato, nonché prezioso collaboratore in alcuni dei progetti di ricerca cui ho preso parte.
Ringrazio i miei *tutors* Pierpaolo Greco e Francesco Valle per tutto il sostegno che mi hanno accordato, sia dal punto di vista tecnico, che umano.
Un ringraziamento doveroso è destinato a tutti i ricercatori e i loro rispettivi gruppi con cui ho avuto la fortuna di collaborare: le Dott.sse Francesca Lugli e Stefania Rapino (Dip. Chimica G. Ciamician, Università degli Studi di Bologna), il Dott. Carlo Ricciardi (Politecnico di Torino), il Dott. Antonino Mazzaglia (CNR-ISMN U.O.S., Palermo), il Dott. Pietro Parisse (Elettra Sincrotrone, Trieste), il Prof. Stefano Pluchino e i suoi collaboratori, il Dott. Matteo Donegà e la Dott.ssa Elena Giusto (University of Cambridge), il Prof. Ricardo García (CSIC, Madrid).

Tutte le persone che lavorano al CNR meritano un ringraziamento, ma elencarli singolarmente sarebbe prolisso e rischierei di dimenticare qualcuno. Ognuno, chi più e chi meno, è stato per me necessario e insostituibile.
Pochi possono affermare di avere degli 'ottimi colleghi'; io, e lo dico con grande orgoglio, ho avuto la fortuna di trovare dei veri amici, splendide persone, dalla grande sensibilità ed empatia.

Infine, ringrazio chi nella mia vita è sempre presente:
questo lavoro, come pure tutto ciò che amo e creo, è dedicato a loro.

Silvia